EXPERIMENTAL INVESTIGATION AND THEORETICAL MODELING OF PIEZOELECTRIC ACTUATORS USED IN FUEL INJECTORS

by

Mohamed Salah Senousy Youssef

B.Sc., Cairo University, Egypt, 2002
M.Sc., Cairo University, Egypt, 2005

A THESIS SUBMITTED IN PARTIAL FULFILMENT OF

THE REQUIREMENTS FOR THE DEGREE OF

DOCTOR OF PHILOSOPHY

in

THE FACULTY OF GRADUATE STUDIES

(Mechanical Engineering)

THE UNIVERSITY OF BRITISH COLUMBIA

(Vancouver)

November 2009

Abstract

Piezoelectric stack actuators are increasingly used in micropositioning applications due to their precision and responsiveness. Advanced automotive fuel injectors have recently been developed that utilize multilayer piezoelectric actuators. Since these injectors must operate under high dynamical excitations at high temperatures, understanding their thermo-electro-mechanical performance under such operating conditions is crucial to their proper design.

In this thesis, the effect on soft Lead Zirconate Titanate (PZT) piezoelectric actuators of different controlling parameters relevant to fuel injection is studied experimentally. These parameters include electric-field magnitude and frequency, driving-field rise time, DC offset, duty-cycle percentage, and ambient temperature. Soft PZT actuators generate a significant amount of heat when driven under high electric-field magnitudes and/or high frequency, both of which occur in fuel injectors. They also exhibit hysteretic nonlinear behavior when driven under high electric-field magnitudes. Self-heating and hysteretic nonlinearity are interconnected, and both are undesirable in applications that require precise positioning, such as fuel injection. Self-heating in PZT stacks is considered to be caused by ferroelectric hysteretic nonlinearity, originating from domain-switching. Theoretical studies of self-heating and domain-switching in PZT materials are developed in this thesis.

An analytical self-heating model based on the first law of thermodynamics is presented that accounts for different parameters such as geometry, magnitude and frequency of applied electric field, duty-cycle percentage, and surrounding properties. It also directly relates self-heating in PZT actuators to displacement-electric field loss (displacement hysteresis), which is found to increase linearly with increased temperature. The model shows reasonable agreement with experimental results at low and high electric-field magnitudes.

A novel domain-switching model for PZT materials is developed. The model is based on changes in potential energy, and accounts for the temperature effect on domain switching. It also accounts for full thermo-electro-mechanical coupling. Additionally, different energy levels are assumed for different domain-switching types. It is assumed that 180^o switching is a two-step process caused by two 90^o switching events. A finite element implementation of a thermo-piezoelectric continuum, based on the proposed switching model, is presented. The model shows good agreement with experimental results at different temperatures and loading conditions.

Table of Contents

List of Tables

List of Figures

List of Symbols

α	Thermal strain coefficients
A	Area
a_1, a_2	Fitting parameters
c	Heat capacity
C	Capacitance
c, a, a_0	Lattice constants
C_p	|Specific heat
D	Electric field displacement vector
d, e	Piezoelectric constants
D_f	Hysteresis
d_t	Duty cycle
E	Electric field vector
ε, ε^r,ε^0	Strain tensors
E_c	Coercive electric field
E_{ch}	Electric charge
f, f_r, ω	Frequency
F, Π, ψ	Energy
G^c	Energy-barrier level
h	Thickness, convective heat coefficient
I	Entropy
φ	Potential
κ	Dielectric Constant
κ_0	Free space permittivity (8.85×10^{-12} F/m)
k, K	Thermal conductivity
L	Length
λ, β, τ, X_1	Constants
m	Mass
n	Number of layers, outward normal vector
P, P^r, P^s	Polarization vectors
p	Pyroelectric constants
Q	Heat source
ρ	Density
R, r	Radius
σ	Stress tensor
s	Surface
s, c	Elastic constants
σ_c	Coercive mechanical stress
T	Temperature

t	Time, thickness
t_h	Thickness, holding time
T_p, T_f	Period
t_r	Rise time
u	Displacement
V, V_{pp}, V_{dc}	Voltage
$\overline{h}$	Convection heat coefficient

Acknowledgments

First and foremost, I would like to acknowledge my thesis supervisors, Professor Nimal Rajapakse and Professor Mohamed Gadala, for their invaluable guidance and support. I am also thankful to Professor Rajapakse for providing financial support from the NSERC research grant.

My respectful gratitude goes to my supervisory committee members: Professors Clarence de Silva and John Madden. I am also grateful to David Mumford, Damien Clapa, Charlie Loo, and Peter Costca of Westport Power Inc. for providing assistance during testing.

The University of British Columbia Graduate Fellowship and Dr. David W. Strangway Fellowship are gratefully acknowledged.

My PhD experience was made more enjoyable by my friends and colleagues. I would like to thank all of them for their friendship, help with research problems, and our fun discussions.

Last but not least, I would like to thank my parents and my wife for their unconditional love, encouragement, and support.

M. Senousy

Dedication

To my lovely wife

Howaida

and our little princesses

Yomna

Boushra

Statement of Co-Authorship

Mohamed Salah Senousy Youssef is the primary author of the papers presented in this work. For all these papers, Mr. Senousy identified and proposed the research topic, performed the literature survey and research, analyzed the data, performed the simulations and prepared the manuscripts under the supervision and direction of Professor Nimal Rajapakse and Professor Mohamed Gadala. Mr. Senousy was assisted in running the experiments by Dr. Faxin Li and Mr. David Mumford.

All this work has been done completely during Mr. Senousy's Ph.D. program. None of the papers presented in this work have received credit or presented in any other thesis work.

M. Senousy

Chapter 1

1. Introduction and Literature Review

1.1. Piezoelectric Materials

1.1.1. Piezoelectricity

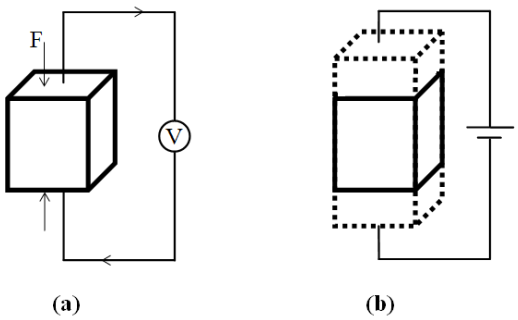

Figure 1.1. An illustration of (a) direct, and (b) converse piezoelectricity.

Piezoelectricity is the ability of certain crystalline materials to generate an electric charge proportional to a mechanical strain. This phenomenon is called *direct piezoelectricity* [Figure 1.1(a)]. *Direct piezoelectricity* was discovered by Pierre and Jacques Curie in 1880 when they were studying the effect of pressure on natural single-crystal structures such as tourmaline, quartz, topaz, and Rochelle salt [1]. Piezoelectricity was later reported for polycrystalline ceramics [2]. In 1881, Lippmann mathematically deduced the converse piezoelectric effect from the fundamental thermodynamic principles. *Converse piezoelectricity* is the ability to generate mechanical strain in response to an applied electric charge [Figure 1.1(b)].

In the presence of a temperature field within a piezoelectric continuum, interaction between the mechanical, electrical, and thermal fields occurs. *Piezoelectricity* is the interaction between mechanical and electrical fields; *pyroelectricity* is the interaction between thermal and electrical fields; and *thermoelasticity* is the interaction between thermal and mechanical fields. The linear constitutive relations for piezothermoelastic materials were derived based on the first and the second laws of thermodynamics (see Ikeda [3] for a detailed derivation). They can be expressed in different ways, depending on the choice of independent variables. For example, if the mechanical stress, electric field, and temperature are chosen as the independent variables, the linear constitutive relations can be expressed as follows:

$$\varepsilon = s\sigma + dE + \alpha T \tag{1.1a}$$

$$D = d\sigma + \kappa E + pT \tag{1.1b}$$

$$I = \alpha\sigma + pE + \alpha_v T \tag{1.1c}$$

where σ and ε are the stress and strain vectors, respectively; I and T are entropy and temperature, respectively; D and E are the electric-displacement and electric-field vectors, respectively; s, d, and κ are the elastic compliance constants, the piezoelectric-strain constants, and the dielectric coefficients, respectively; α and p are the thermal-strain coefficients and pyroelectric constants, respectively; and α_v is a material constant.

It can be seen in Equation (1.1) that the equations for linear elasticity, dielectrics, and entropy are coupled by means of the piezoelectric constants d, the thermoelastic constants α, and the pyroelectric constants p. If these constants are set to zero, the

coupled linear piezothermoelastic constitutive relations are reduced to three uncoupled constitutive equations.

Piezoelectricity requires a particular crystal structure, such that only crystal structures with no center of symmetry can exhibit piezoelectricity. A piezoelectric unit cell is then said to be *noncentrosymmetric*. There exist *32* crystal point groups, of which *21* are *noncentrosymmetric,* with *20* of these possessing piezoelectric properties [4]. Due to the crystal symmetry in piezoelectric crystals, the number of nonzero independent material constants in the *d* matrix is reduced. Uchino [4] described the symmetries in the piezoelectric matrix *d* for all crystal point groups, and showed the position of nonzero independent constants. *d* is zero for a *centrosymmetric* ceramic. For a tetragonal ferroelectric ceramic such as the widely used *Lead Zirconate Titanate (PZT)* ceramics, the number of independent piezoelectric material constants is 3, and *d* is expressed as

$$\begin{bmatrix} 0 & 0 & 0 & 0 & d_{15} & 0 \\ 0 & 0 & 0 & d_{15} & 0 & 0 \\ d_{13} & d_{13} & d_{33} & 0 & 0 & 0 \end{bmatrix} \tag{1.2}$$

1.1.2. Ferroelectricity

Ferroelectric materials are a subcategory of piezoelectric materials. *Ferroelectricity* was first discovered in single crystal structures, such as Rochelle salt. It was later discovered in polycrystalline ceramics such as *Lead Zirconate Titanate (PZT)*, *Lanthanum Lead Zirconate Titanate (PLZT)*, *and Barium Titanate ($BaTiO_3$)* [5]. Ferroelectric materials are also classified as a subcategory of dielectric materials. In dielectric materials, the constituent atoms are either positively or negatively charged.

Due to electrostatic interactions, an applied electric field forces the positively charged atoms (*cations*) to move towards the cathode, whereas the negatively charged atoms (*anions*) move towards the anode [6]. Consequently, an electric dipole moment is developed. On the other hand, if the center of the positively charged atoms coincides with the center of the negatively charged atoms, the electric dipole moment is zero. This phenomenon is called *electric polarization*. The polarization P is expressed as the sum of electric dipole moments per unit volume (C/m^2), and it is related to the external electric field E by the following expression:

$$D = \kappa_0 E + P = \kappa\kappa_0 E \tag{1.3}$$

where D is the electric-field displacement vector (C/m); κ_0 is the free space permittivity (8.85×10^{-12} F/m); and κ is the relative dielectric constant.

In some crystal structures, the centers of the positive and negative atoms do not coincide, even without the application of an external electric field. These crystals are said to possess a *spontaneous polarization* P^s. If P^s can be altered by the application of an electric field opposite to its direction, these crystal structures are called *ferroelectrics*. Note that not all dielectric materials are ferroelectrics.

Ferroelectric materials undergo phase transformation at a transition temperature known as the *Curie temperature* T_c. They undergo a ferroelectric to paraelectric phase transformation above the Curie temperature, and lose their spontaneous polarization and ferroelectric properties. This phase transformation results in the center of the positively charged atoms and the center of the negatively charged atoms coinciding. The material is then said to be *paraelectric*.

1.1.3. PZT Ceramics

Lead Zirconate Titanate (PZT) ceramics are ferroelectric ceramics. They were discovered in 1954, and since then have replaced other ferroelectric ceramics and become the dominant piezoelectric ceramics in applications [7]. PZT ceramics are widely used in actuator applications that require fast, reliable and precise performance [8-10]. They are superior to other ferroelectric ceramics because they have higher electromechanical coupling; higher Curie temperature values, which permit a higher temperature range of operation; and a wider range of dielectric constants. They are also easier to be poled by applying an external electric field [5].

PZT ceramics are binary solid solutions of Lead Zirconate ($PbZrO_3$) and Lead Titanate ($PbTiO_3$). They have an ABO_3 perovskite-type crystal structure, depicted in Figure 1.2. PZT-ABO_3 perovskite structures are cubic at elevated temperatures ($> T_c$), whereas they exhibit either tetragonal or rhombohedral structures at room temperature, depending on their composition. Tetragonal PZT structures are the focus of this study. In an ABO_3 unit cell, there is an A^{2+} ion at each corner (Pb^{2+} in the case of PZT), a B^{4+} ion at the centroid (Zr^{4+}/Ti^{4+} in the case of PZT), and an O^{2-} ion at the center of each face of the unit cell. In the tetragonal phase, the central ion Zr^{4+}/Ti^{4+} moves relative to the side ions O^{2-}, resulting in a spontaneous polarization P^s. Consequently, the unit cell expands in the direction of the spontaneous polarization (*poling axis*) and contracts in the other two directions, and a spontaneous strain ε^s is developed. The spontaneous strain in the poling axis is $\frac{c-a_0}{a_0}$, whereas it is $\frac{a-a_0}{a_0}$ in the other two axes (a_0 is the lattice parameter in the cubic state; c and a are the new lattice parameters in the tetragonal state, as shown in Figure 1.2).

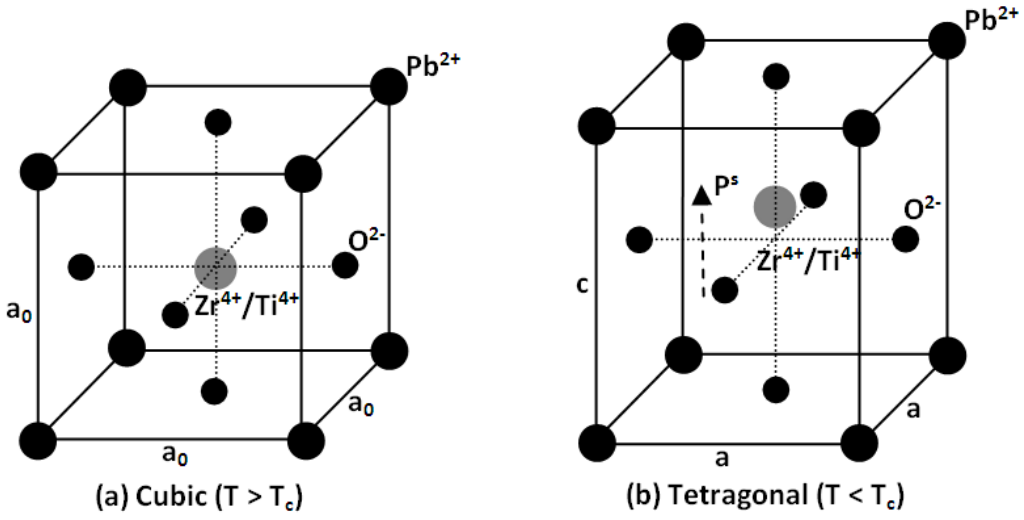

Figure 1.2. Perovskite structure of PZT at (a) $T > T_c$, and (b) $T < T_c$.

The piezoelectric properties of PZT ceramics are controlled by doping the crystals with impurities [11]. PZT ceramics can be broadly classified into two categories: (1) soft PZT ceramics; and (2) hard PZT ceramics. Soft PZTs are obtained by doping PZT crystals with donor elements such as Nb^{5+} or La^{3+}, replacing Zr^{4+} or Pb^{2+}, respectively. Hard PZTs are obtained by doping PZT ceramics with acceptors such as FE^{3+}, replacing Zr^{4+} or Ti^{4+}. Soft PZT ceramics have higher piezoelectric coefficients, coupling factors, and mechanical compliance than hard PZT ceramics.

1.2. Nonlinear Constitutive Behavior of PZT Ceramics

At low electric-field magnitudes, PZT materials show linear response and exhibit no complicated behavior. At high electric-field magnitudes, nonlinear behavior is observed. If the mechanical stress, electric field, and temperature are chosen as independent variables, the constitutive relations accounting for remnant polarization and strain can be written as

$$\varepsilon = s\sigma + dE + \alpha T + \varepsilon^r \tag{1.4a}$$

$$D = d\sigma + \kappa E + pT + P^r \tag{1.4b}$$

$$I = \alpha\sigma + pE + \alpha_v T \tag{1.4c}$$

where ε^r and P^r are the remnant strain and remnant polarization vectors, respectively. ε^r and P^r are defined as the macroscopic strain and macroscopic polarization, respectively, at zero electric field. They are calculated by averaging the spontaneous strain ε^s and the spontaneous polarization P^s, respectively, over all domains.

It is well accepted that nonlinearities in PZT ceramics are mainly due to a phenomenon called *domain switching*, otherwise known as *domain-wall motion* [12]. Domains are regions with the same spontaneous polarization direction. They tend to be formed to minimize free energy when piezoelectric ceramics undergo paraelectric to ferroelectric phase transformation at the Curie temperature [2]. Domain switching is the ability to rotate the spontaneous polarization direction of a domain by either 180^o or non-180^o in response to an applied electric field (*ferroelectric switching*) or mechanical stress (*ferroelastic switching*) higher than the critical values, known as the coercive electric

field and the coercive stress, respectively. Figure 1.3(a) and Figure 1.3(b) show the nonlinear macroscopic polarization–electric field hysteresis loop and the nonlinear macroscopic strain–electric field hysteresis loop (*butterfly loop*), respectively. The coercive electric field E_c can be defined, according to Figure 1.3, as the electric field at which the macroscopic-remnant polarization reduces to zero.

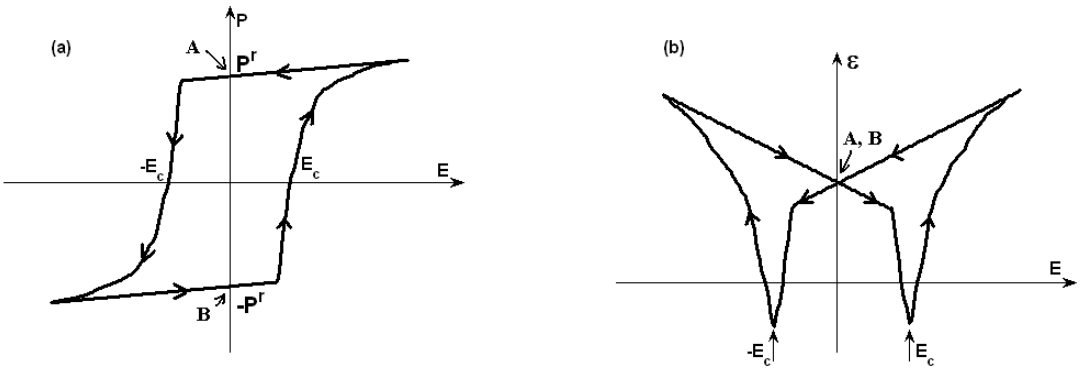

Figure 1.3. Hysteresis nonlinearity demonstrated in (a) polarization—electric field hysteresis loop, and (b) strain—electric field (butterfly) hysteresis loop.

In tetragonal ferroelectric ceramics such as PZT ceramics, domains can switch by either 180^o or 90^o. If an electric field is applied in the same direction of the poling axis of a PZT unit cell, the unit cell elongates along this axis, whereas it contracts when an electric field is applied opposite to the polarization direction. If this latter electric field is sufficiently large (i.e., larger than the coercive electric field E_c), the central positive ion, Zr^{4+}/Ti^{4+}, can move towards one of five possible off-center sites; one possible 180^o switching direction; and four possible 90^o switching directions. Consequently, the polarization direction is reoriented. This type of switching is called *ferroelectric domain switching*, otherwise known as *electric field-driven switching*. Figure 1.4(a) shows a PZT

unit cell poled along its c-axis, so that its polarization vector is given by [*0 0 -P*^{s}]. Figure 1.4(b) shows the switched unit cell when a positive electric field is applied along the c-axis; the unit cell switches by 180^o and the new polarization vector is given by [*0 0 P*^{s}]. 180^o domain switching does not cause any change in spontaneous strain. However, 90^o domain switching increases strain by $\frac{c-a}{a_0}$ in the new polarization direction, and reduces strain by the same amount in the preceding polarization direction.

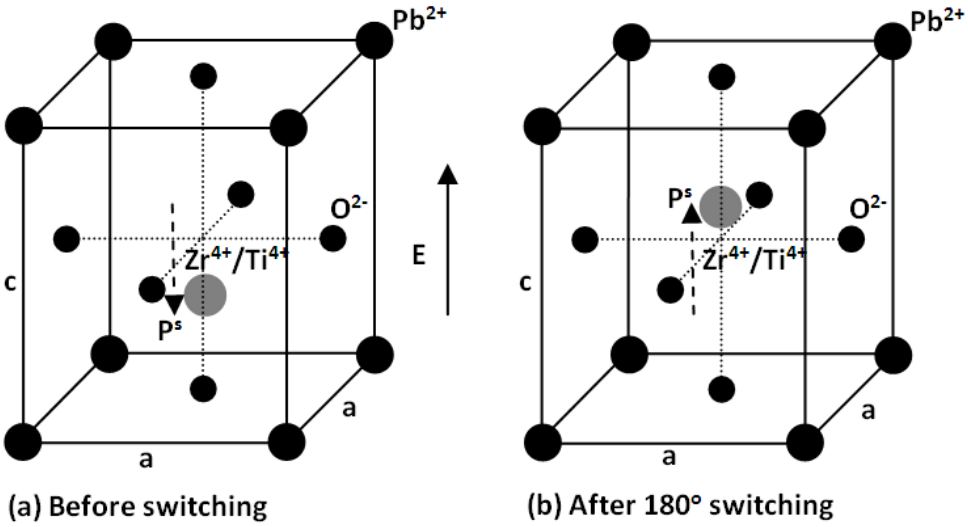

Figure 1.4. Ferroelectric switching in PZT ceramics.

Ferroelastic domain switching, otherwise known as *stress-driven switching*, is caused by the application of a sufficiently large stress in a direction parallel to the polarization direction, as shown in Figure 1.5. Mechanical stress can only cause the central positive ion to move towards one of the four side sites, causing 90^o domain switching; 180^o domain switching cannot be triggered by a mechanical stress.

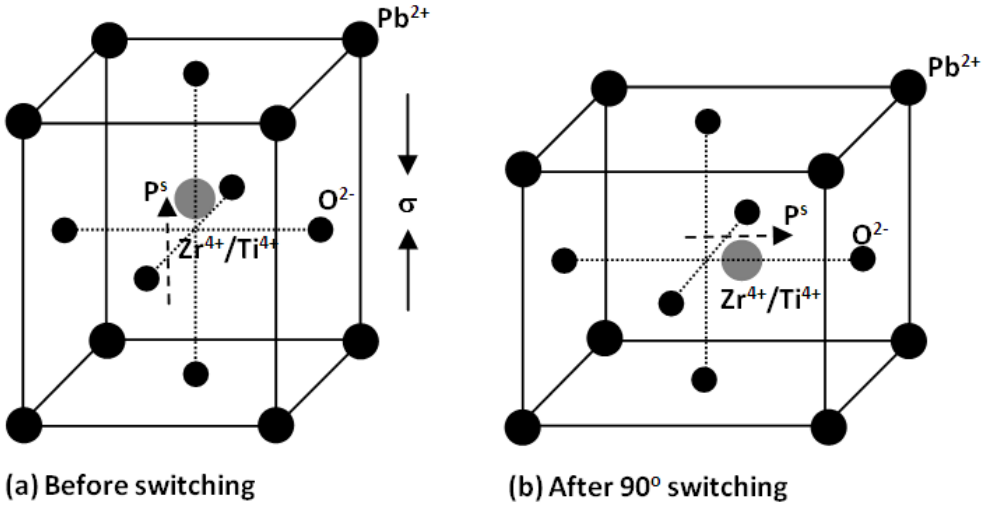

Figure 1.5. Ferroelastic switching in PZT ceramics.

1.3. Modeling of Domain Switching

The development of domain switching models for piezoelectric materials remains a challenging task because of the evolving microstructure and polycrystalline nature of these materials. Hwang et al. [12] developed the first domain-switching criterion, based on a reduction in potential energy. They assumed that the spontaneous polarization direction of a domain switches when the reduction in potential energy exceeds a certain value, known as the "*switching-energy barrier*". According to [12], the reduction in potential energy for a single domain is related to the change in spontaneous polarization ΔP^s and spontaneous strain $\Delta \varepsilon^s$, as follows:

$$E\Delta P^s + \sigma \Delta \varepsilon^s \geq G^c \tag{1.5}$$

where the left-hand side represents the reduction in potential energy, and G^c is the critical switching-energy barrier.

Hwang et al. [12] focused their study on Lead Lanthanum Zirconate Titanate (PLZT) ceramics, which exhibit tetragonal perovskite crystal structures at room temperature. PLZT ceramics can, therefore, switch by either 90^o or 180^o under a sufficiently large electric field and/or mechanical stress. Hwang et al. [12] assumed that both 180^o and 90^o domain switching occurs at the same energy level. The critical energy barriers G^c for both switching types were expressed as

$$G^c = G^c_{180^o} = G^c_{90^o} = 2E_c P^s \tag{1.6}$$

Based on the concepts of Hwang et al. [12], a domain-switching criterion that considered the fracture and fatigue behavior of tetragonal PZT ceramics was developed by Jiang [13]. Although Jiang [13] also assumed that the energy required to cause 180^o or 90^o switching is identical, and used Equation (1.6) to represent the critical energy barriers, he extended the above model to also include the dependence of potential energy reduction on variations in the produced strain. Moreover, he assumed that the coercive electric field E_c is dependent on the applied compressive stress σ, and that the coercive mechanical stress σ_c is dependent on the applied electric field E, such that

$$E_c^{'} = \frac{E_c}{1-\lambda\sigma}, \text{ and } \sigma_c^{'} = \sigma_c - \beta E \tag{1.7}$$

where λ and β are material constants.

Lu et al. [14] developed a domain-switching model based on the Gibbs free energy. They stated that a domain with a higher Gibbs free energy tends to change to another state with a lower Gibbs free energy. The difference in the Gibbs free energy between the

two states was considered as the domain-switching driving force. Lu et al. [14] considered this driving force to be dependent only on the change in spontaneous strain and spontaneous polarization. However, they assumed different energy dissipation levels associated with 180° and 90° domain switching. The energy barrier for 180° domain switching $G^{c}_{180^o}$ was found to be equal to Equation (1.6), whereas the energy barrier for 90° domain switching $G^{c}_{90^o}$ was expressed as follows:

$$G^{c}_{90^o} = \left(\frac{c-a}{a_0}\right)\sigma_c + \frac{1}{2}(S_{11} - S_{33})\sigma_c^2 \tag{1.8}$$

where c, a, and a_0 are lattice parameters; S_{11} and S_{33} are components of the elastic compliance in the x_1 and x_3 directions, respectively; and σ_c is the coercive mechanical stress.

The above model was later modified by Li et al. [15] to account for the interactions among the switched domains and their neighbors. They calculated the domain-switching driving force based on the change in Gibbs free energy for both switched domains and their neighbors. They also used different energy barriers for 180° and 90° domain switching. This criterion was further modified by Li et al. [16] to account for incomplete domain switching.

Huber et al. [17] also proposed a different form of the energy required to activate 90° domain switching such that

$$G^{c}_{90^o} = \sqrt{2}E_c P^s \tag{1.9}$$

Zeng and Rajapakse [18] developed another domain-switching criterion based on potential energy. This criterion did not differentiate between the energy levels required to activate 90^o and 180^o domain switching. Instead, both energy barriers were considered equal to Equation (1.6). However, the change in potential energy accounted for the change in material properties in addition to switching strains and switching polarization. Zeng and Rajapakse [18] applied their developed criterion to simulate the evolution of 180° and 90° domain nuclei in ferroelectric ceramics.

Although theoretical formulations of domain switching in ferroelectric ceramics were introduced in the early 1990s, experimental studies on this phenomenon have received attention since the mid-1960s. Krueger [19] studied the effect of compressive stress parallel to the poling axis on domain switching of PZT ceramics. He compared the response of both hard and soft PZT ceramics. PZT-4 and PZT-8 were used as hard ceramics, and PZT-5A and PZT-5H as soft ceramics. Krueger [20] studied the effect of compressive stress perpendicular to the poling axis on domain switching of the same ceramics. He reported that compressive stresses parallel to the poling axis caused domain switching, and that depolarization of the material occurred; *depolarizatio*n is the phenomenon of remnant strain and remnant polarization reduction with increased compressive stress. On the other hand, compressive stresses perpendicular to the poling axis stabilize domain switching, and have a negligible effect on the hysteresis behavior on the PZT material.

Lynch [21] studied the electromechanical response of PLZT 8/65/35 under a constant compressive preload and a cyclic electric field parallel to the poling axis. He observed that both remnant strain and remnant polarization decreased with increased compressive

stress. The nonlinear electromechanical behavior of soft PZT-51 under combined electromechanical loading was experimentally studied by Fang and Li [22]. The effect of parallel and perpendicular compressive stresses on the nonlinear behavior of soft PZT-51 was also investigated by Li et al. [23]. Similar studies were conducted by Yimnirun et al. [24, 25] who reported that polarization—electric field hysteresis decreases with increased compressive loading. Shindo et al. [26, 27] experimentally and numerically studied the effect of applied voltage on the electro-elastic field concentrations ahead of electrodes in multilayer soft PZT actuators.

1.4. Multilayer PZT Stack Actuators

Piezoelectric materials have been widely used as distributed sensors and actuators in diverse engineering applications due to their direct and converse piezoelectric effects [28]. Because of their light weight, piezoelectric sensors and actuators are used in smart structures vibration suppression [29], shape control, and on-line fault detection [30]. Piezoelectric sensors are not subjected to large loading and their mechanical or dielectric strength is not an issue. However, since piezoactuators can be subjected to large mechanical and electric cyclic loads, strength, durability, and other factors must be considered.

Piezoactuators have advantages over conventional actuators because of their compact design, high speed, and easily controllable stroke. They have also been proven to withstand harsh environmental conditions. Piezoelectric actuators can be classified into two categories: (1) flexural actuators, such as unimorph and bimorph actuators; and (2) extensional actuators, such as multilayer stack actuators. Flexural piezoelectric actuators

typically generate low forces, but produce large displacement. Multilayer stack actuators normally generate larger forces, but small displacements [31].

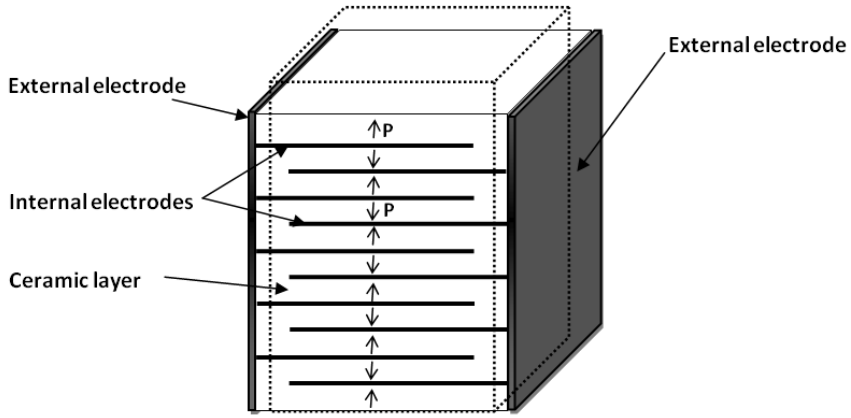

Figure 1.6. Multilayer PZT stack actuator.

A multilayer piezoelectric stack actuator consists of thin piezoelectric discs with adjacent discs having opposite poling directions bonded together and sandwiched between electrodes, as shown in Figure 1.6. Discs are mechanically connected in series and electrically connected in parallel. The thickness of each disc is as small as 100 μm, and the thickness of the electrode is in the order of 10 μm [32]. The axial length of a typical multilayer piezoelectric stack actuator can change by up to 0.12% by applying an electric field across the layers; the resultant actuator stroke can be calculated by multiplying the total number of layers by the net displacement of a single layer. The applied electric field across a multilayer actuator is obtained by dividing the applied voltage by the thickness of one disc ($E = V/t_h$); the electric field increases with decreasing disc thickness. Therefore, having several hundreds of thin layers stacked with alternating electrodes allows reducing the applied voltage to as low as 100-200 Volts.

Multilayer PZT stack actuators are manufactured using one of two techniques: (1) cut-and-bond (stacking); or (2) tape casting (co-firing) [33]. The stacking process is simpler, but it is time-consuming. It involves firing; polishing; electroding; and adhesive bonding of electrodes and ceramic layers into a stack. The tape-casting method requires extensive production facilities and more complicated techniques, but is widely preferred for fabricating multilayer piezoelectric stack actuators. A significant advantage of the tape-casting method is that it allows producing thinner layers with several hundred layers in a single stack; this in turns allows using lower applied voltage. Additionally, the tape-casting method is suitable for mass-production because it is a cost-effective production method.

The tape-casting method starts with a green, unfired, organic binder-bound tape of piezoelectric ceramic composition with printed patterns of electrode paste; this green composition is then laminated using temperature and pressure. The external electrodes are, thereafter, printed. Subsequently, the organic binder is burned out and the composite of the ceramic materials and electrodes are sintered at high temperature (as high as 1200 ^{o}C). When the ceramic cools to room temperature, it is said to be unpoled, with its domains polarized in different directions. Domains in the unpoled state are randomly polarized with relative spontaneous polarization orientations of either 180^{o} or 90^{o} between each two neighbors. An unpoled ceramic has a zero remnant polarization with no piezoelectric properties. The ceramic is then subjected to a strong DC electric field to reorient the domains as closely as possible to the electric-field direction; this process is called *poling*. After poling the ceramic, remnant polarization is no longer zero; the ceramic is said to be poled, and it possesses piezoelectric properties.

1.5. Multilayer PZT Stack Actuators in Fuel Injector Applications

High-pressure direct injection (HPDI) is a breakthrough technology that is pioneered and developed in Canada by Vancouver based Westport Innovations Inc. It would significantly reduce emissions produced by diesel engines used in transportation. A key element of HPDI technology is the fuel injector. Advanced fuel injectors that utilize multilayer PZT actuators for injector needle opening have been introduced as an innovative replacement of the conventional solenoid technology.

Multilayer PZT stack actuators were first investigated for use in fuel injection systems in the early 1990s [34]. In the late 1990s, fuel injection systems based on piezoelectric injectors that achieved better fuel metering than conventional actuators were reported in many patents, for example [35, 36]. Recently, DENSO Corporation and Toyota Motor Corporation have introduced the world's first 1,800 bar diesel common rail injection system [37], is based on piezoelectric injectors. They claim to have achieved the world's highest fuel injection pressure with the shortest injection interval.

In a fuel injector, PZT stack actuators control the injection process via an applied electric field; the stroke of the actuator is used to activate a valve needle, allowing the pressurized fuel to be injected, as shown in Figure 1.7. The response time of the needle nozzle is typically less than 0.1 msec. The short response time reduces the fuel delivery rate and the energy required from the high-pressure fuel pump [38]. Also, since the valve is actuated more quickly, very precise injection intervals are possible between pre- and main injections, which significantly reduces emissions, and reduces fuel consumption by up to 15 percent [39]. Furthermore, piezoelectric actuator-based injectors allow an

increase in the injection pressure, up to 250 MPa; the higher the pressure and the more accurate the dosing and timing of the injection, the more efficient (and therefore less polluting) the combustion event becomes. It should be noted that whereas the valve-needle stroke is fixed in electromagnetic injection systems, in injectors where the piezoelectric actuator acts directly on the needle, the needle stroke can be varied by changing the magnitude of the applied voltage, enabling better control over the valve opening. Overall, the advantages of piezoelectric injectors over conventional solenoid technology are that they provide an optimized injection system (i.e., quieter, more economical, more powerful, reduced emissions [40]).

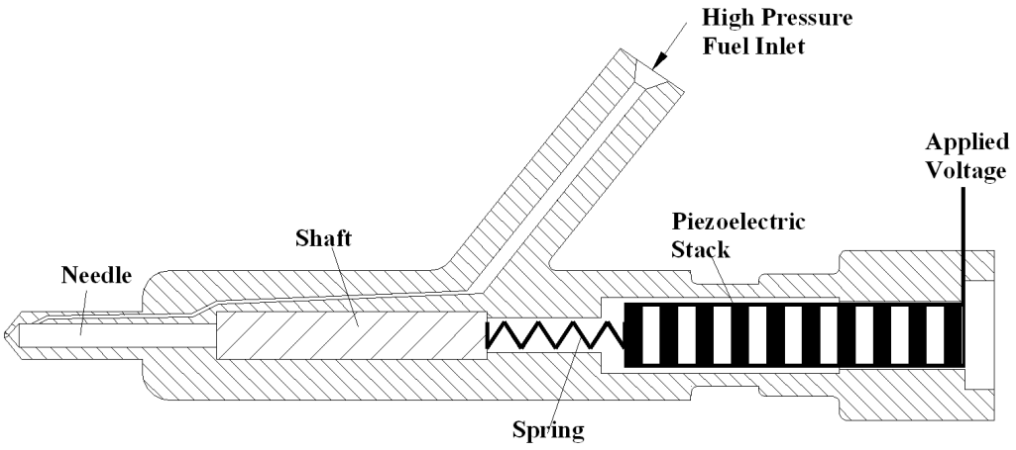

Figure 1.7. A schematic of a piezoelectric-based fuel injector.

The overall response of the injector needle, which is in direct contact with the actuators, is governed by different controlling parameters. These parameters include the applied voltage, frequency, driving-field rise time, biased DC offset voltage, duty cycle, and ambient temperature. Because of the operational requirements in fuel injection, stack actuators are subjected to relatively high electric-field magnitudes (> 1.5 kV/mm), high frequencies (> 100 Hz), and elevated temperatures (up to 120 ^{o}C). Operating at high

electric-field magnitudes close to or larger than the coercive electric field E_c, may result in a nonlinear response of the actuators, which is not desirable in applications that require precise positioning, such as fuel injection. In addition to the elevated operating temperature, PZT stacks typically generate heat when driven under high electric-field magnitudes and/or high frequency. This generated heat may accelerate material aging, and may also produce thermal stresses. The resulting thermal stresses could, in turn, lead to structural failure by debonding the interface between the ceramic and the electrodes [41].

1.6. Self-Heat Generation in PZT Stacks

Self heating in PZT actuators is a serious issue when precise accuracy is required, which is the case in fuel injection systems. Self heating is observed under dynamic loading, even in the linear range of operation. It can substantially affect the overall performance and durability of PZT actuators, and may limit their use. It can also affect the electro-mechanical coupling coefficients, resonance frequencies, and oscillation amplitudes of piezoelectric elements [42]. For example, in high power applications, the resonance frequencies; mode shapes; and oscillation amplitudes of the piezoelectric actuators are not stable until the steady-state temperature is reached. Self heating also has a direct effect on current consumption and total displacement of an actuator; Rokanen et al. [43] reported that a temperature rise of 1.0 ^{o}C caused a change in current consumption by almost 0.5 %.

Self heating is considered to be caused by losses, such as mechanical damping and dielectric loss, with the major contribution from dielectric loss caused by ferroelectric

hysteresis loss [44-46], which is believed to be caused by domain switching. Zheng et al. [47] proposed a theoretical model to explain the mechanism of heating in piezoelectric materials. Their model was based on the law of energy conservation and the assumption that the rate of heat generation was directly proportional to the frequency and hysteresis loss per driving cycle per unit volume. However, the dependence of hysteresis on temperature was not considered in their model. The model was expressed in an exponential form written as

$$T = T_0 + \Delta T_\infty \left(1 - e^{-t/\tau}\right) \tag{1.10}$$

where T, T_0, and ΔT_∞ are the actuator temperature, initial temperature, and steady-state temperature, respectively. τ is a time constant which was found to be material and geometry dependent.

Zheng et al. [47] also experimentally studied the effect of geometry of PZT stacks on self heating under different operating conditions at room temperature. They studied 5 different actuator sizes, with a layer thickness of 20 and 40 μm. They reported that the steady-state temperature rise ΔT_∞ of an actuator linearly increased with the ratio v_e/A (v_e and A are the total active volume and the surface area, respectively). The steady-state temperature rise ΔT_∞ was also found to increase with increased electric field and frequency. As an example, a 7×7×2 mm^3 actuator, under an applied electric field of 2.5 kV/mm and a frequency of 300 Hz, ΔT_∞ was around 70 ^oC. Similar results were experimentally verified by other researchers [43, 48].

Another mathematical model that explains self-heating phenomenon in piezoelectric materials was proposed by Lesieutre et al. [49]. The main difference was the inclusion of heat dissipation from the actuator by convection and radiation [47] or by only convection [49]. Lesieutre et al. [49] studied the thermal response of PZT actuators under two different conditions: (1) stand-alone actuators; and (2) actuators embedded in a composite. For the latter case, it was reported that the actuator-composite interface had the highest temperature increase.

Lu and Hanagud [50] developed an irreversible thermodynamics model to predict self-heating in PZT stacks. Their model considered different loss mechanics and expressed the cyclic increase in temperature as

$$\Delta T = \frac{\pi \omega d_{33} \mathrm{X}^2}{\rho c_v \left(\mathrm{Y}^2 + \omega^2 \mathrm{Z}^2 \right)} E_0^2 \tag{1.11}$$

where ω is the excitation frequency; E_0 is the amplitude of the applied electric field; and all other constants are material-related constants.

According to Equation (1.11), if ω is small, ΔT linearly increases with increased frequency reaching a peak value ΔT_{max}. On the other hand, if ω is large, ΔT decreases with increased frequency and reaches zero when $\omega \to \infty$. This, however, contradicts with their experimental findings, where they showed that ΔT exponentially increased with increased frequency, until it reached a steady state.

1.7. Scope of the Present Work

Based on the above literature review, several research issues related to the use of multilayer PZT actuators in fuel injector applications remain uncertain and need further investigation. Current understanding of the thermo-electro-mechanical performance of these actuators under dynamic driving conditions relevant to fuel injection is limited. Therefore, this thesis has two main objectives:

1. To experimentally study the response of multilayer PZT actuators under operating conditions relevant to the development of advanced fuel injectors. Data related to temperature and strain distribution, stroke-load relationship, loading frequency and rise time, and duty cycle effects are obtained and analyzed.
2. To theoretically model temperature-dependent domain switching, nonlinear constitutive behavior, and self heating in PZT actuators under cyclic-electric loading.

A comparison between the experimental results from the first objective and the obtained results from the second objective is presented.

The organization of this thesis is as follows: in Chapter 2, the thermo-electro-mechanical performance of custom made soft PZT stack actuators manufactured by *Kinetic Ceramics Inc.* is experimentally investigated. The actuators are examined over a temperature range of -30 ^{o}C to 80 ^{o}C, under driving electric fields of up to 2.0 kV/mm, different frequencies, and a constant preload of about 5 MPa. The effect of using different excitation wave forms, which corresponds to different rise times, on the actuation performance of the stacks is also studied. Additionally, self heating in the

actuators under different electric-field magnitudes, frequencies, and duty cycles is investigated.

In Chapter 3, a simplified analytical self-heating model is presented. The model directly relates self heating in multilayer piezoelectric stack actuators to displacement-electric field loss (displacement hysteresis). The model is based on the first law of thermodynamics, and accounts for different parameters such as geometry, magnitude and frequency of applied electric field, duty cycle percentage, and surrounding properties. The findings from the proposed model are compared with experimental results.

In Chapter 4, a new domain-switching model for PZT piezoelectric materials is presented. The model is based on the reduction in potential energy caused by the contributions from changes in spontaneous strain and spontaneous polarization, as well as the interaction of electro-mechanical fields with switching strains and switching polarization. The model accounts for the substantial influence of full thermo-electro-mechanical coupling. The effect of change in material properties before and after switching is also included. Therefore, the proposed model is valid for general anisotropic piezothermoelastic materials. It is assumed that 180^o switching is a result of two 90^o switching events. The proposed model is then implemented in a finite element scheme based on the weighted-residual principle. Isoparametric finite elements are used. Selected Numerical results for D_3-E_3 and S_3-E_3 hysteresis loops are compared with the experimental results for soft PZT ceramics. The conclusions of the present study and the recommendations for future work are presented in Chapter 5.

1.8. Bibliography

[1] Cady WG. Piezoelectricity. *McGraw-Hill*. New York, USA 1946.

[2] Jaffe B, Cook WR, Jaffe H. Piezoelectric Ceramic. *Academic Press Inc.* London 1971.

[3] Ikeda T. Fundamentals of Piezoelectricity. *Oxford University Press Inc.* New York, USA 1996.

[4] Uchino K. Piezoelectric Actuators and Ultrasonic Motors. *Kluwer Academic Publishers*. Norwell, Massachusetts, USA 1997.

[5] Haertling GH. Ferroelectric Ceramics: History and Technology. *Journal of the American Ceramic Society* 1999;82:797.

[6] Buchanan RC. Ceramic materials for electronics: processing, properties, and applications. *Marcel Dekker Inc.* New York 1991.

[7] Fujishima S. The history of ceramic filters. *IEEE Transactions on Ultrasonics, Ferroelectrics and Frequency Control* 2000;47:1.

[8] Jäker P. Electro-Mechanical Characterization of High-Performance Piezoactuators. *Proceedings of SPIE* 1997;3039:670.

[9] Ardelean EV, Cole DG, Clark RL. High performance "V-stack" piezoelectric actuator. *Journal of Intelligent Material Systems and Structures* 2004;15:879.

[10] Chen Q, Yao DJ, Kim CJ, Carman GP. Frequency response of an inchworm motor fabricated with micromachined interlocking surface mesoscale actuator device (MAD). *Proceedings of SPIE* 1998;3329:768.

[11] Uchino K. Ferroelectric Devices. *Marcel Dekker Inc.* New York, USA 2000.

[12] Hwang SC, Lynch CS, McMeeking RM. Ferroelectric/ferroelastic interactions and a polarization switching model. *Acta Materialia* 1995;43:2073.

[13] Jiang L. Fracture and fatigue behaviour of piezoelectric materials. Ph.D Thesis, *Purdue University*, West Lafayette, IN, USA 1998.

[14] Lu W, Fang DN, Li CQ, Hwang KC. Nonlinear electric–mechanical behavior and micromechanics modeling of ferroelectric domain evolution. *Acta Materialia* 1999;47:2913.

[15] Li F, Fang D. Simulations of domain switching in ferroelectrics by a three-dimensional finite element model. *Mechanics of Materials* 2004;36:959.

[16] Li FX, Rajapakse RKND. Nonlinear finite element modeling of polycrystalline ferroelectrics based on constrained domain switching. *Computational Materials Science* 2008;44:322.

[17] Huber J, Fleck N, Landis CM, McMeeking RM. A constitutive model for ferroelectric polycrystals. *Journal of the Mechanics and Physics of Solids* 1999;47:1663.

[18] Zeng X, Rajapakse RKND. Eshelby tensor for piezoelectric inclusion and application to modeling of domain switching and evolution. *Acta Materialia* 2003;51:4121.

[19] Krueger HHA. Stress Sensitivity of Piezoelectric Ceramics: Part 1. Sensitivity to Compressive Stress Parallel to the Polar Axis. *Journal of the Acoustical Society of America* 1967;42:636.

[20] Krueger HHA. Stress Sensitivity of Piezoelectric Ceramics: Part 3. Sensitivity to Compressive Stress Perpendicular to the Polar Axis. *Journal of the Acoustical Society of America* 1968;43:583.

[21] Lynch CS. Electro-mechanical coupling in 8/65/35 PLZT. *9th IEEE International Symposium* 1994:357.

[22] Fang D, Li C. Nonlinear electric-mechanical behavior of a soft PZT-51 ferroelectric ceramic. *Journal of Materials Science* 1999;34:4001.

[23] Li F, Fang D, Lee J-J, Kim HC. Effects of compressive stress on the nonlinear electromechanical behavior of ferroelectric ceramics. *Science in China, Series E: Technological Sciences* 2006;49:29.

[24] Yimnirun R, Laosiritaworn Y, Wongsaenmai S. Effect of uniaxial compressive pre-stress on ferroelectric properties of soft PZT ceramics. *Journal of Physics D: Applied Physics* 2006;39:759.

[25] Yimnirun R, Triamnak N, Unruan M, Ngamjarurojana A, Laosiritaworn Y, Ananta S. Ferroelectric properties of Pb(Zr1/2Ti1/2)O3-Pb(Zn1/3 Nb2/3)O3 ceramics under compressive stress. *Current Applied Physics* 2009;9:249.

[26] Shindo Y, Yoshida M, Narita F, Horiguchi K. Electroelastic field concentrations ahead of electrodes in multilayer piezoelectric actuators: experiment and finite element simulation. *Journal of the Mechanics and Physics of Solids* 2004;52:1109.

[27] Shindo Y, Narita F, Hirama M. Electromechanical field concentrations near the electrode tip in partially poled multilayer piezo-film actuators. *Smart Materials and Structures* 2009;18:085020.

[28] Uchino K. Piezoelectric actuators: Expansion from IT/robotics to ecological/energy applications. *Journal of Electroceramics* 2008;20:301.

[29] Qiu J, Tani J. Vibration control of a cylindrical shell using distributed piezoelectric sensors and actuators. *Journal of Intelligent Material Systems and Structures* 1995;6:474.

[30] Akella P, Chen X, Cheng W, Hughes D, Wen JT. Modeling and control of smart structures with bonded piezoelectric sensors and actuators. *Journal of Smart Materials and Structures* 1994;3:344.

[31] Nuffer J, Bein T. Application of piezoelectric materials in transportation industry. Global Symposium on Innovative Solutions for the Advancement of the Transport Industry. San Sebastian, Spain, 2006.

[32] Zeng X. Theoretical modeling of small-scale domain switching and fracture of ferroelectric ceramics. Ph.D thesis*, The University of British Columbia*, Vancouver, BC, Canada 2002.

[33] Uchino K. Materials issues in design and performance of piezoelectric actuators: an overview. *Acta Materialia* 1998;46:3745.

[34] Wolff A, Cramer D, Hellebrand H, Probst I, Lubitz K. Optical two channel elongation measurement of PZT piezoelectric multilayer stack actuators. *IEEE International Symposium on Applications of Ferroelectrics* 1994:755.

[35] Gromek B, Shen JJ. Multiple stack piezoelectric actuator for a fuel injector. *United States Patent, Patent Number 6,345,771*, 2000.

[36] Takase S. Piezoelectric actuator and fuel-injection apparatus using the actuator. *United States Patent, Patent Number 6-155-500*, 1999.

[37] Fujii A, Toyao T. Piezoelectric actuators with high reliability for diesel injection valve. *10th International Conference on New Actuators,* 2006:177.

[38] Randall CA, Kelnberger A, Yang GY, Eitel RE, Shrout TR. High strain piezoelectric multilayer actuators: A material science and engineering challenge. *Journal of Electroceramics* 2005;14:177.

[39] Scharf A. Prize-Winning Piezo. *Piezo-actuators in fuel injection systems, EPCOS technical articles*, 2006.

[40] Boecking F, Sugg B. Piezo Actuators: A technology prevails with injection valves for combustion engines. *10th International Conference on New Actuators,* 2006:171.

[41] Aburatani H, Harada S, Uchino K, Furuta A, Fuda Y. Destruction mechanisms in ceramic multilayer actuators. *Japanese Journal of Applied Physics* 1994;33:3091.

[42] Keoschkerjan R, Harutyunyan M, Wurmus H. Analysis of self-heating phenomenon of piezoelectric microcomponents actuated harmonically. *Microsystem Technologies* 2002;9:75.

[43] Ronkanen P, Kallio P, Vilkko M, Koivo HN. Self heating of piezoelectric actuators: Measurement and compensation. *Int. Symp. on Micro-NanoMechatronics and Human Sci.,* 2004:313.

[44] Uchino K, Hirose S. Loss mechanisms in piezoelectrics: How to measure different losses separately. *IEEE Transactions on Ultrasonics, Ferroelectrics, and Frequency Control* 2001;48:307.

[45] Ochi A, Takahashi S, Tagami S. Temperature Characteristics for Multilayer Piezoelectric Ceramic Actuator. *Japanese Journal of Applied Physics* 1985;24:209.

[46] Yao K, Uchino K, Xu Y, Dong S, Lim LC. Compact piezoelectric stacked actuators for high power applications. *IEEE Transactions on Ultrasonics, Ferroelectrics, and Frequency Control* 2000;47:819.

[47] Zheng J, Takahashi S, Yoshikawa S, Uchino K, de Vries JWC. Heat generation in multilayer piezoelectric actuators. *Journal of the American Ceramic Society* 1996;79:3193.

[48] Pritchard J, Ramesh R, Bowen CR. Time-temperature profiles of multi-layer actuators. *Sensors and Actuators, A: Physical* 2004;115:140.

[49] Lesieutre GA, Fang L, Koopmann GH, Pai SP, Yoshikawa S. Heat generation of a piezoceramic induced-strain actuator embedded in a glass/epoxy composite panel. *Smart Structures and Materials* 1996;2717:267.

[50] Lu X, Hanagud SV. Extended irreversible thermodynamics modeling for self-heating and dissipation in piezoelectric ceramics. *IEEE Transactions on Ultrasonics, Ferroelectrics, and Frequency Control* 2004;51:1582.

Chapter 2

2. Experimental Investigation*

2.1. Introduction

Piezoelectric ceramic elements are used as distributed sensors and actuators in many engineering applications because of their direct and converse piezoelectric effects. Industrial piezoelectric devices are subject to high temperatures, thus must be designed to withstand thermal effects. These devices are also widely used in dynamically loaded systems that require fast, reliable and precise actuation performance. Modern internal combustion engines are a cutting-edge example of such dynamic systems, where fuel injectors based on piezoelectric actuators are used to open and close fuel injection valves. A critical component of this new generation of fuel injectors is the multilayer piezoelectric stack actuator, which controls the injection process via an applied electric field.

A multilayer piezoelectric actuator consists of piezoelectric thin discs with adjacent discs having opposite poling directions bonded together and sandwiched between electrodes. The axial length of a typical actuator used in fuel injectors can change by up

* "A version of this chapter has been published. **Senousy, M. S.,** Li, F.X., Mumford, D., Gadala, M.S., and Rajapakse, R.K.N.D. (2009) Thermo-electro-mechanical Performance of Piezoelectric Stack Actuators for Fuel Injector Applications, *Journal of Intelligent Material Systems and Structures*, Vol. 20, No. 4, pp. 387-399."

to 0.12% by applying an electric field across the layer elements; the resultant actuator stroke can be calculated by multiplying the total number of layers by the net displacement of a single layer. This stroke is used to activate a valve needle that allows the fuel to be injected and controlled. Since the valve is actuated more quickly with piezoelectric actuators than by conventional solenoids, very precise injection intervals are possible between pre- and main injection, which significantly reduce emissions. Overall, piezoelectric actuators represent a promising improvement in direct fuel injection technology, with its precise positioning and rapid response time compared with conventional solenoid technology [1].

Fuel metering in the combustion chamber is important for reducing the level of emissions generated during the combustion process, while minimizing fuel consumption. Therefore, many proposals have been made to provide fuel metering control for fuel injector systems, including systems that employ piezoelectric fuel injectors [2, 3]. Boecking and Sugg [4] proposed an optimal piezoelectric injection actuator for combustion engines that overcomes the drawbacks of solenoid valves, with a design that accounts for heat dissipation in the actuator. Fujii and Toyao [5] presented a piezoelectric actuator used in Toyota diesel engines with an injection interval as low as 0.1 msec.

It is yet clear that fuel injector technology utilizing piezoelectric actuators holds much promise. The static and dynamic performance of stacked piezoelectric actuators has received some attention in the past [6-11]. However, studies addressing the performance of these actuators under conditions that are directly applicable to fuel injection do not appear in the literature. It is therefore important to examine the performance and reliability of piezoelectric actuators under conditions that simulate the actual operating

conditions of a fuel injector (high electric-field levels, > *1.5* kV/mm, high frequencies, > 100 Hz, and elevated operating temperature, up to 120 ^{o}C).

The quasi-static thermo-electro-mechanical performance of cylindrical PZT actuators manufactured by Kinetic Ceramics Inc. was investigated in our lab by Li et al. [10] over a temperature range of -30 ^{o}C to 125 ^{o}C, under driving-electric fields varying from 0.3 to 1.8 kV/mm. Ardelean et al. [8] also experimentally investigated the quasi-static and dynamic behavior of piezoelectric actuators manufactured by Noliac. Co-fired piezoelectric actuators manufactured by Piceramic were experimentally studied by Heinzmann et al. [9]. They studied the actuators' behavior over an ambient temperature range of -40 ^{o}C to 150 ^{o}C.

In this chapter, we conduct a comprehensive investigation of the dynamic thermo-electro-mechanical response of a typical set of multilayer piezoelectric stack actuators under different ambient temperatures, electric-field magnitudes, duty cycles, frequencies, and rise times. The temperature increase due to heat generation, under continuous AC driving fields (100% duty cycle), and its effect on the response of the actuators are also studied for different frequencies and electric-field magnitudes.

2.2. Experimental Procedure

Custom-made PZT multi-layer stack actuators manufactured by Kinetic Ceramics Inc. *(www.kineticceramics.com)* were used in this study. The actuators are made from soft PZT ceramics with a coercive field E_c of 1.08 kV/mm, and have a Curie temperature above 360 ^{o}C (*Kinetic Ceramics Inc.*). Although soft PZT ceramics have a higher dielectric loss factor $tan\delta$ than hard PZT ceramics, which promotes higher heat generation under large electric-field magnitude and/or frequency, they have a higher piezoelectric coefficient d, which makes them advantageous for actuator applications because they produce a greater strain than harder materials in response to an applied electric field [12-14]. However, soft PZT ceramics are characterized by highly mobile domain-walls, whereas hard PZT ceramics restrain the domain-wall response so that higher electric-field magnitudes are required for the same effect to be observed. Table 2.1 shows the geometry and properties of the actuators used in this study.

The actuators used in the study conducted by Li et al. [10] could not be used for dynamic testing in this study as they are incompatible with the current driver; their high capacitance reduces the applied voltage at the actuator to about one-third of the commanded voltage. This difference in voltage is caused primarily by the reactive impedance of the piezoelectric actuators, which places some special requirements on the amplifier. In other words, the amplifier has to handle significantly higher voltages and circulating currents than are suggested by the real electrical/mechanical power requirements of the actuator. Additionally, Linder et al. [15] showed that the electrical power at the actuator terminals has a negative real component, indicating that the

actuator feeds electrical power back to the source. Since the current actuators are smaller and have lower capacitance than those used by Li et al. [10], there is almost no difference between the two voltages.

Table 2.1. PZT stack actuator characteristics.

Property	***Value***
Actuator diameter (mm)	5
Actuator length (mm)	30
Layer thickness (mm)	0.5
Number of layers (stacks)	54
Capacitance (nF)	69
Maximum operating voltage (Volts)	1000
Maximum operating electric field (kV/mm)	2.0
Longitudinal piezoelectric coefficient d_{33} (pC/N)	370
Young's Modulus Y_{33} (GPa)	48

The test stand (shown in Figure 2.1) was placed inside a thermal chamber (*TestEquity Model 1007C*) with a temperature range of -73 ^{o}C to 175 ^{o}C and a temperature feedback control of 0.1 ^{o}C. The temperature of the actuator was measured through a Resistance Temperature Detector (*RTD*) attached to the surface of the actuator.

In injector applications, the piezo actuators are subjected to a compressive preload for alignment and other design requirements. Li et al. [10] found that a preload of -40 MPa has a negligible effect on the static response of an actuator. The actuators were therefore subjected to a constant compressive preload of 5 MPa (100 Newton) throughout the testing; the preload was applied using a soft spring (30 N/mm) fixed by a screw nut and

measured using a force sensor placed between a shaft and a moving loading head, which was in direct contact with the actuators. The other end of the actuator was placed on a fixed plate, allowing the displacement to be measured using a Linear Variable Displacement Transducer (*LVDT*), with a resolution of 0.1 μm. The measured displacement, temperature, and force signals were input into a National Instrument data acquisition system and monitored by a computer.

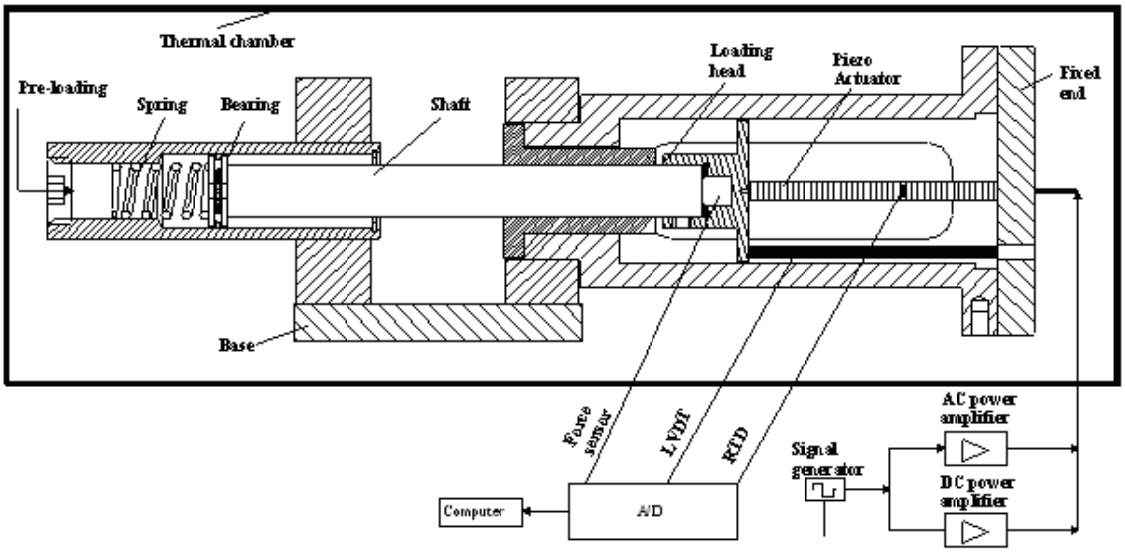

Figure 2.1. Test setup.

Four different wave forms - sine wave and trapezoidal waves *A*, *B*, and *C* (Figure 2.2) - were applied using the Agilent signal generator with variable wave frequencies. The chosen wave forms were based on the potential design requirements of fuel injectors.

A TREK piezo driver/power amplifier model *PZD700*, with an adjustable gain of up to 300 V/V, was used. Since the maximum allowed negative voltage applied to the stacks was -200 Volts (-20% of allowable full operating voltage), a DC bias voltage had to be applied to ensure that the negative voltage peak did not exceed -200 Volts (-0.4 kV/mm).

The actuator was operated at full vendor-specified voltage with a bias field of +300 Volts, and an AC field of +500/-500 Volts. Although the DC offset was kept at -20 % of the applied voltage, its effect on dynamic stroke was also examined.

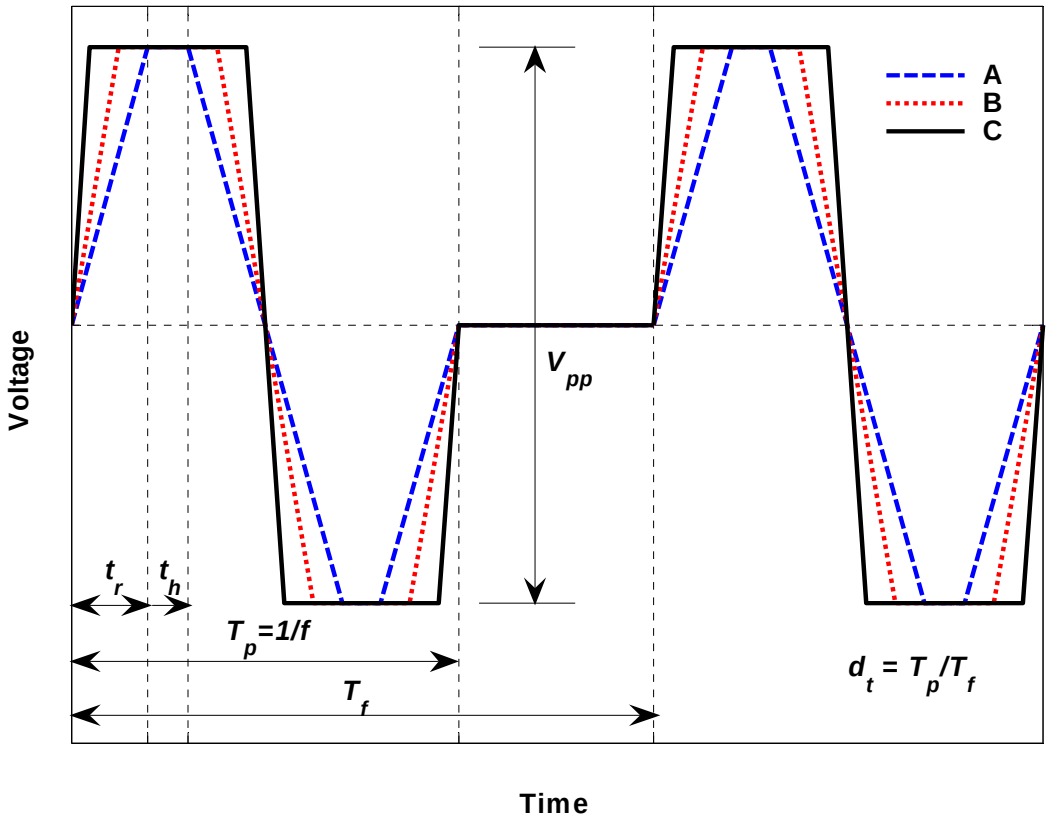

Figure 2.2. Illustration of the three different driving-field trapezoidal waves (A, B, and C).

The test procedure consisted of the following steps:

(1) aligning the piezoelectric actuator with the centre of the shaft and the loading head;

(2) preloading the actuator using a screw nut through a spring;

(3) choosing the desired wave form, electric-field magnitude, and frequency using the signal generator;

(4) switching the power amplifier on and adjusting the DC offset;

(5) firing the actuator; and

(6) recording data.

In the current study, different controlling parameters were employed to obtain a better understanding of the dynamic behavior of the stacks. These parameters include the electric-field magnitude E ($E=V_{pp}/h$, where V_{pp} is the applied peak-to-peak voltage and h is the thickness of a single layer), frequency f, driving-field rise time t_r, biased DC offset voltage V_{dc}, duty cycle d_t, and ambient temperature. In addition, a sinusoidal wave form and three different trapezoidal waves A, B, and C with different rise times were used. Wave A had the longest rise time, $t_r = 0.2\ T_p$, where T_p is the driving-field period, and C had the shortest rise time, $t_r = 0.05\ T_p$ (Figure 2.2). Holding time t_h is defined as the period over which a signal is kept constant at a peak value, $T_p=4t_r+2t_h$. Duty cycle is defined as the ratio between the driving-field period and the period of a complete voltage cycle, T_f (i.e., $d_t = T_p/T_f$). A duty cycle of *100%* means a continuous wave, whereas a 0 % duty cycle implies no signal, or a DC signal.

2.3. Experimental Results

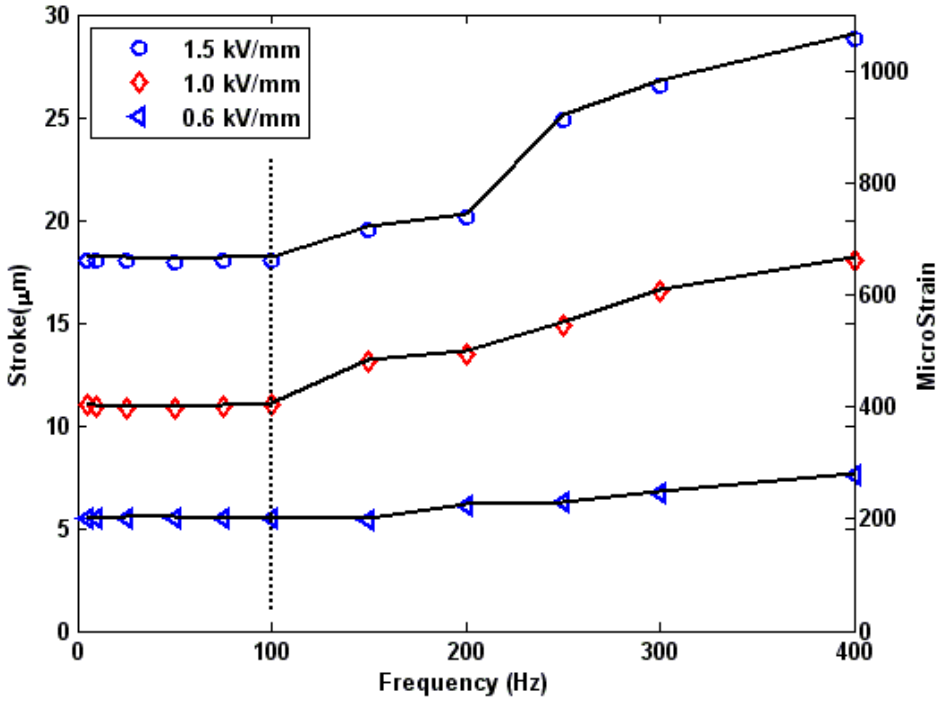

Figure 2.3. Variation of the dynamic stroke of piezoelectric stack actuators with driving frequency (sine wave and 10% duty cycle).

Figure 2.3 shows the frequency dependence of the dynamic stroke under sinusoidal electric driving fields of 0.6, 1.0, and 1.5 kV/mm and a duty cycle of 10 %. It can be seen from Figure 2.3 that below a frequency of 100 Hz, the dynamic stroke was almost constant. However, for frequencies higher than 100 Hz, the dynamic stroke increased almost linearly with the driving-field frequency. It can also be seen that the rate of change of the stroke increased with increasing electric-field magnitude as a result of the increased activities of non-180^{o} domain walls at high electric-field magnitudes (i.e., ≥ coercive electric field). Moreover, the temperature rise of the tested actuator increased with increased frequency, as it will be shown in Section 2.4. As a result, an additional

extrinsic part was introduced to account for the temperature-driven activities of non-180° domain walls. The resonance frequency, f_r, of the testing system (including the actuator, loading shaft, spring for pre-loading, etc.) was found to be about 500 Hz. This estimate is based on an actuator axial stiffness of 31 N/μm, a mass of 5 gm, and a moving-parts mass of 3 Kg. Thus, as expected, when the driving-field frequency approached f_r, the dynamic stroke and system oscillations rapidly increased with frequency, as shown in Figure 2.4.

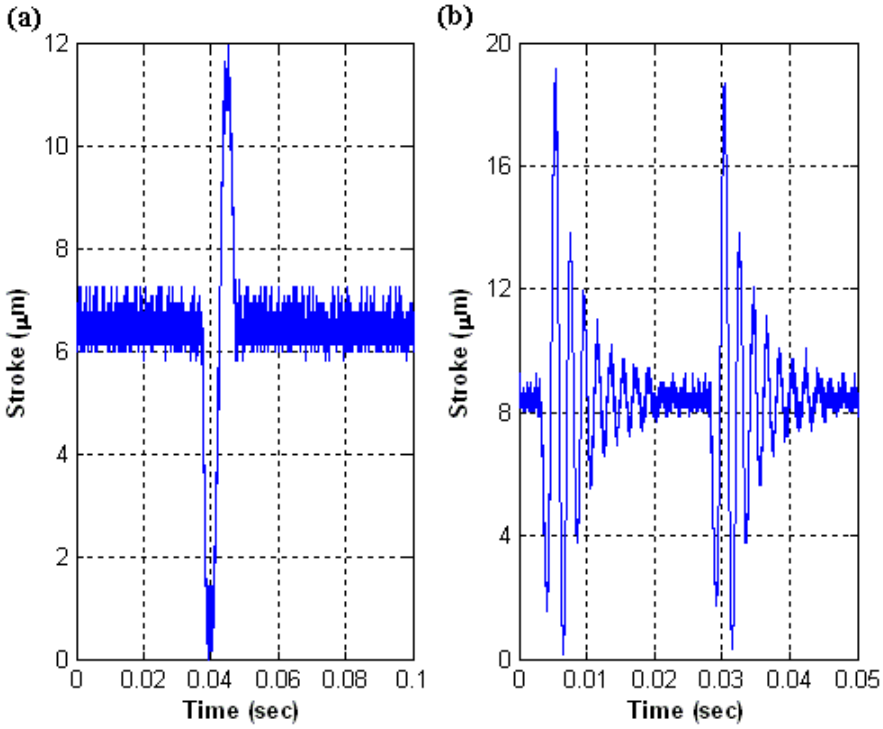

Figure 2.4. Dynamic stroke under (a) 100 Hz and (b) 400 Hz sinusoidal wave forms (E = 1.0 kV/mm and 10 % duty cycle).

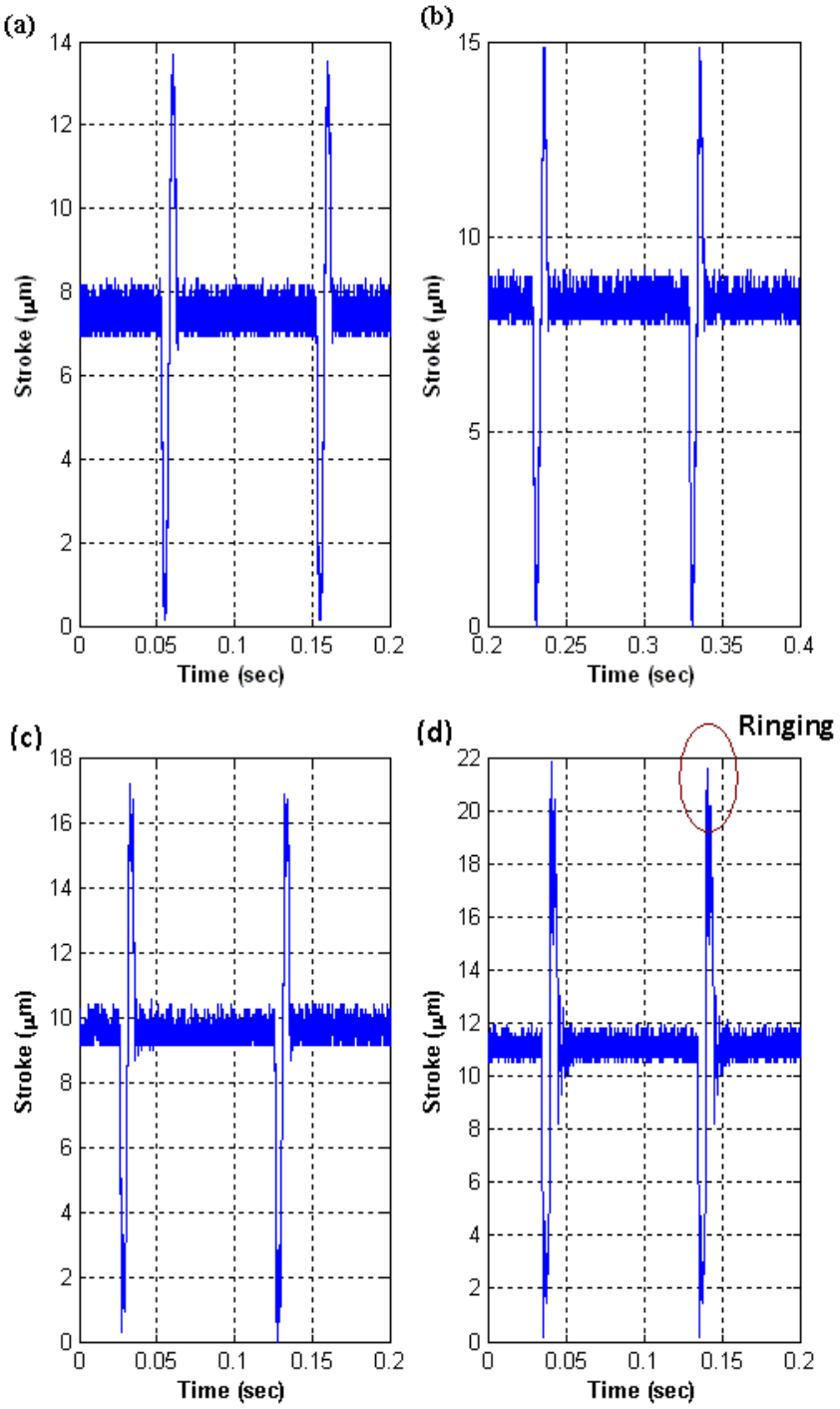

Figure 2.5 Dynamic stroke under (a) sine wave, (b) trapezoidal wave A, (c) trapezoidal wave B, and (d) trapezoidal wave C (E = 1.0 kV/mm, f = 100 Hz and 10 % duty cycle).

Figure 2.5 shows the dynamic stroke for the four waveforms at a frequency of 100*Hz*, a driving-field magnitude of 1.0 *kV/mm*, and a 10% duty cycle. For all the driving waveforms considered, the dynamic stroke showed a highest ringing level at the trapezoidal wave C, which had the shortest rise time [Figure 2.5(d)]. The decrease in rise time is believed to increase the effect of the sub-harmonics of the driving field, which may explain the increase in dynamic stroke ringing with decreased rise time.

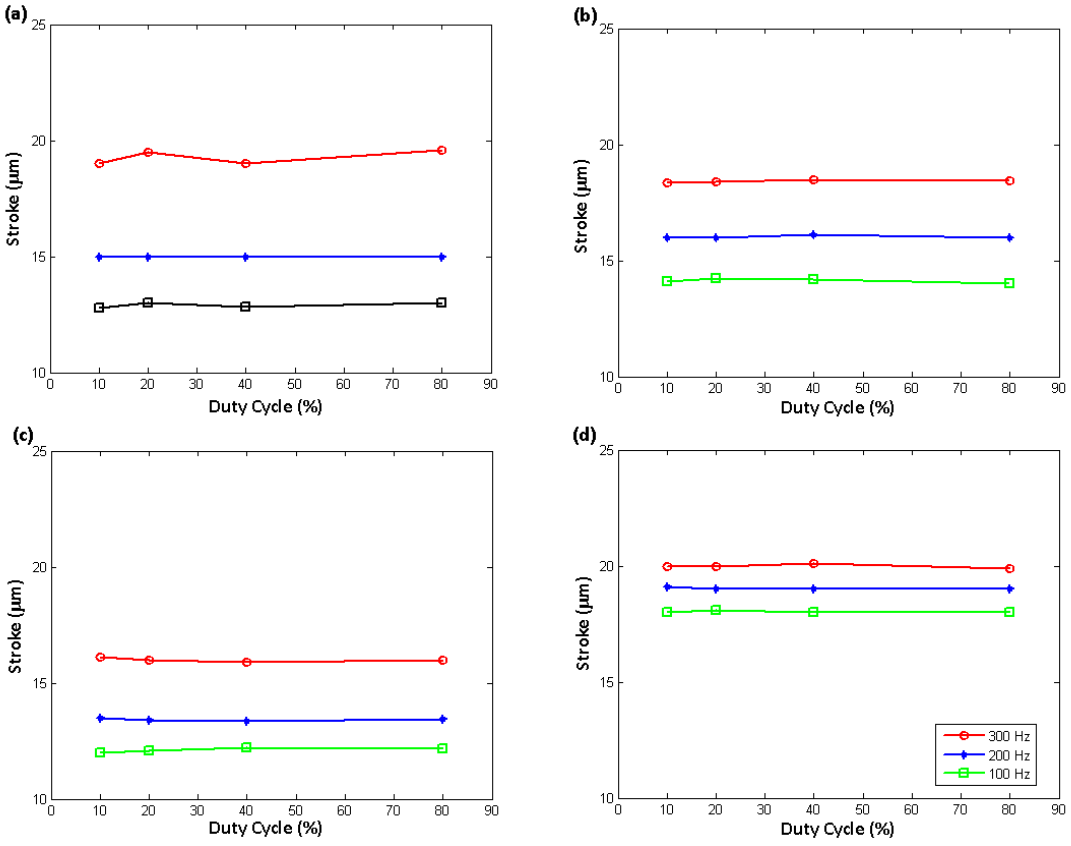

Figure 2.6. Effect of duty cycle on stroke for four different wave forms at E = 1.0 kV/mm: (a) sine wave, (b) trapezoidal A, (c) trapezoidal B, and (d) trapezoidal C.

Figure 2.6 shows the effect of duty cycle on dynamic stroke for the four different waveforms at E = 1.0 kV/mm and for different frequencies up to 300 Hz. It can be seen from the figure that the duty cycle had almost no effect on dynamic stroke for both sinusoidal and trapezoidal loading. Although duty cycle did not affect dynamic stroke, it strongly affected the temperature increase of the PZT actuators being considered in this study, except at low frequencies and electric-field magnitudes. The duty cycle was therefore fixed at 10% in all remaining dynamic testing, except for the self-heat generation tests presented in Section 2.4, where duty cycles up to 100 % were investigated. Figure 2.6 also shows that the dynamic strokes corresponding to the three trapezoidal waves were larger than those corresponding to the sinusoidal wave. Furthermore, under trapezoidal loading, the shortest rise time yielded the largest stroke.

In Figure 2.7, dynamic stroke is plotted against rise time for different trapezoidal driving-field magnitudes, with duty cycle constant at 10%. Dynamic stroke was found to increase with decreased driving-field rise time. The rise-time dependence may be explained by the time dependence of the extrinsic response of PZT. Sherritt et al. [16] reported that non-180^{o} domain switching is time dependent and needs a finite time to occur, and that only domain wall motions that have sufficient time to occur contribute to the piezoelectric response. This result suggests that as rise time decreased in the current study (*i.e., holding time increased*), more domain walls may have had enough time to realign causing a larger actuator stroke. The increasing effect of the sub-harmonics of the driving field may also explain the increase in stroke with decreased rise time. System inertia is also expected to have contributed to this response. In the practical case of a piezoelectric actuator in a fuel injector, the mass of the moving parts is much less than in

the test stand. Therefore, the rise-time effect may differ in practices, but it will still show the decaying trend depicted in Figure 2.7.

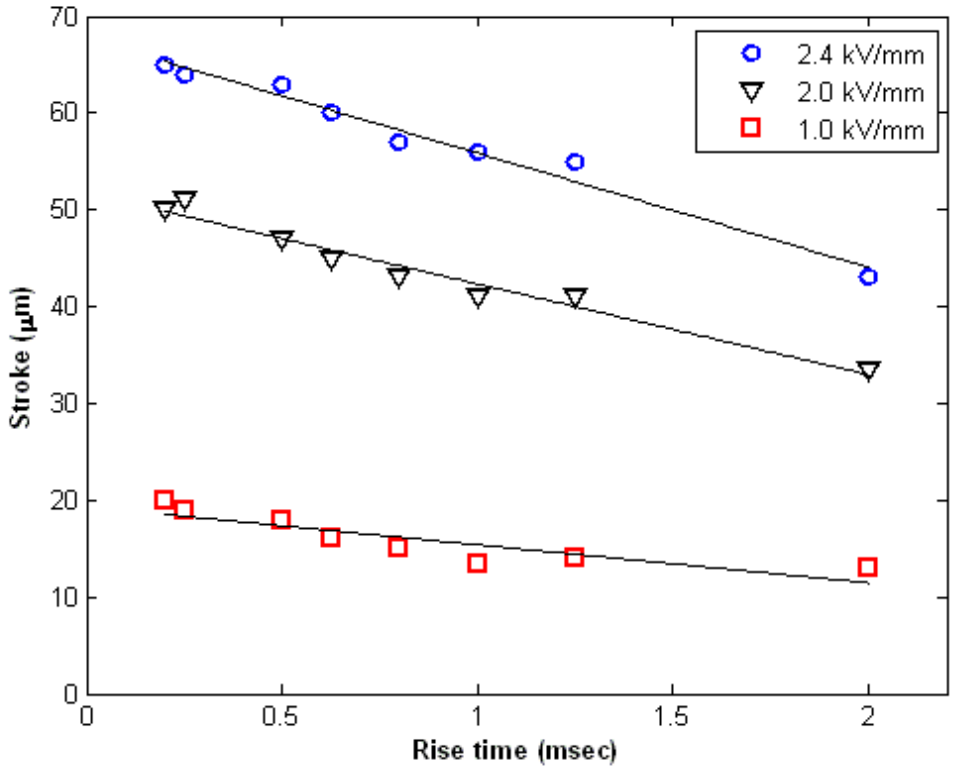

Figure 2.7. Effect of rise time on dynamic stroke for different trapezoidal driving-field magnitudes at 10 % duty cycle.

Figure 2.8 shows the dependence of dynamic stroke on ambient temperature under a sinusoidal electric driving field with magnitude ranging from 0.6 to 2.0 kV/mm, a frequency of 100 Hz, and a duty cycle of 10 %. It can be seen that dynamic stroke increased steadily with ambient temperature under the range of driving field magnitudes considered. However, at driving fields of 1.0 kV/mm and above, a nonlinear transition zone occurred between 40 ^{o}C and 55 ^{o}C, leading to an almost bilinear stroke-temperature curve. As discussed by Strukov et al. [17], if domain wall density is in equilibrium state,

new domain walls are not generated immediately after heating. Instead, a certain degree of heating is required for domain wall density to change noticeably and reach another equilibrium state. Accordingly, the nonlinear transition zone observed in Figure 2.8 may be explained by the extrinsic contribution from increased domain wall density and non-180^{o} domain switching-induced strain. The general trend of the dynamic stroke results shown in Figure 2.8 is similar to that found in static-stroke tests [10], where a nonlinear transition zone was observed between 25 ^{o}C and 60 ^{o}C.

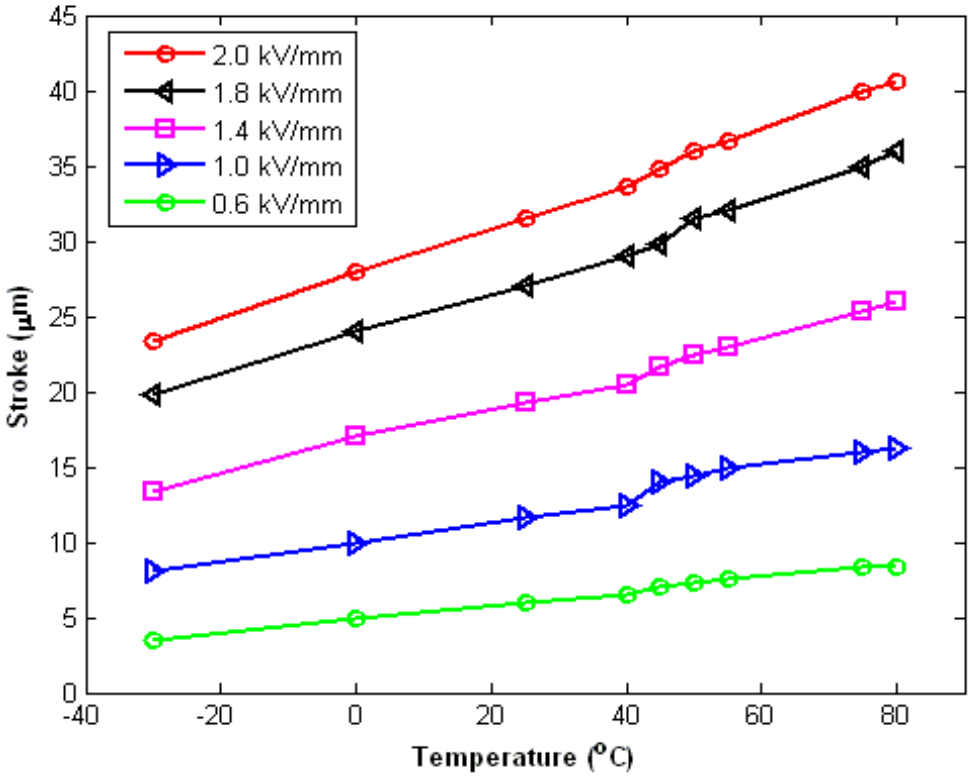

Figure 2.8. Variation of dynamic stroke with ambient temperature under different sinusoidal driving field magnitudes (100 Hz and 10 % duty cycle).

To reveal the relationship between driving-field magnitude and dynamic stroke over the desired ambient temperature range (-30 ^{o}C to 80 ^{o}C), Figure 2.8 is re-plotted in Figure 2.9. As expected, dynamic stroke increased with driving-field magnitude, such that the stroke-electric field curves can be approximated by a bilinear curve connecting two points with a slope modulation point at 0.6 kV/mm, and the slopes of the curves increase with ambient temperature. Li et al. [10] found that in the static case, the static strain at the maximum driving-field magnitude (1.8 kV/mm) was about 1.7 times the product of the electric field and the piezoelectric constant, d_{33}, measured at a low driving field. For the actuators used in this study, the dynamic strain at maximum driving–field magnitude (2.0 kV/mm) was almost 1.6 times the product of the electric field and the piezoelectric constant, d_{33}, measured at a low driving-field magnitude, which indicates that under higher driving-field magnitudes, non-180^{o} domain switching-induced strain may contribute to the piezoelectric response.

Assuming that the thermal-expansion coefficient α does not change with electric-field magnitude, the longitudinal piezoelectric constant d_{33} at different temperatures can be calculated by dividing the induced longitudinal strain, indirectly measured using the *LVDT*, by the applied electric field. d_{33} was calculated over a temperature range of -30 ^{o}C to 80 ^{o}C and electric-field magnitudes of up to 2.8 kV/mm using the measured stroke. As expected, the longitudinal piezoelectric constant showed a nonlinear dependence on electric-field magnitude under different temperatures, as depicted in Figure 2.10, which is in good agreement with the results obtained at room temperature by Masys et al.[18].

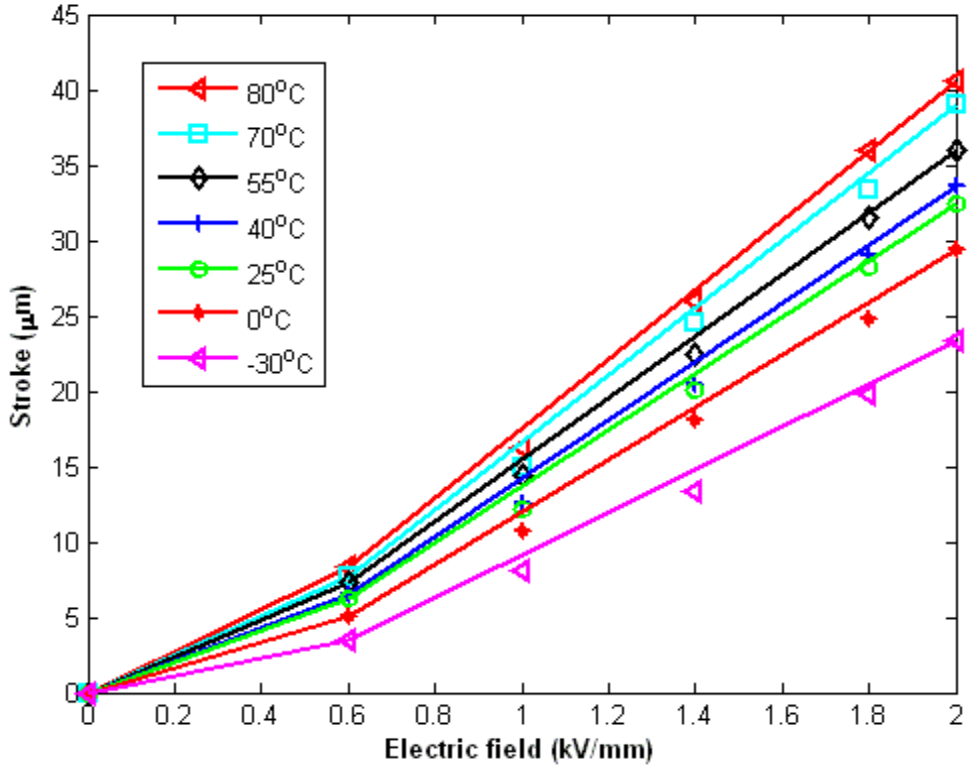

Figure 2.9. Variation of dynamic stroke with driving-field magnitudes over an ambient temperature range of -30 °C to 80 °C (sinusoidal wave at 100 Hz and 10 % duty cycle).

For low electric-field magnitudes (≤ 0.6 kV/mm), the material behavior was approximately linear and d_{33} was almost constant (Figure 2.10, region I). When the applied electric field increased, d_{33} increased nonlinearly with E (Figure 2.10, region II). Figure 2.10 also shows that d_{33} increased with ambient temperature. The computed d_{33} of the stack actuator at room temperature and low-driving fields was about 350 x 10^{-12} C/N, which is close to the vendor-specified data of 370x10^{-12} C/N. At room temperature and an electric-field magnitude of 2.0 kV/mm, d_{33} reached a value of ≈540x10^{-12} C/N (≈ 55 %

increase from the value at low driving field). In the temperature range -30 ^{o}C to 80 ^{o}C at low electric-field magnitudes, d_{33} increased by 125 %.

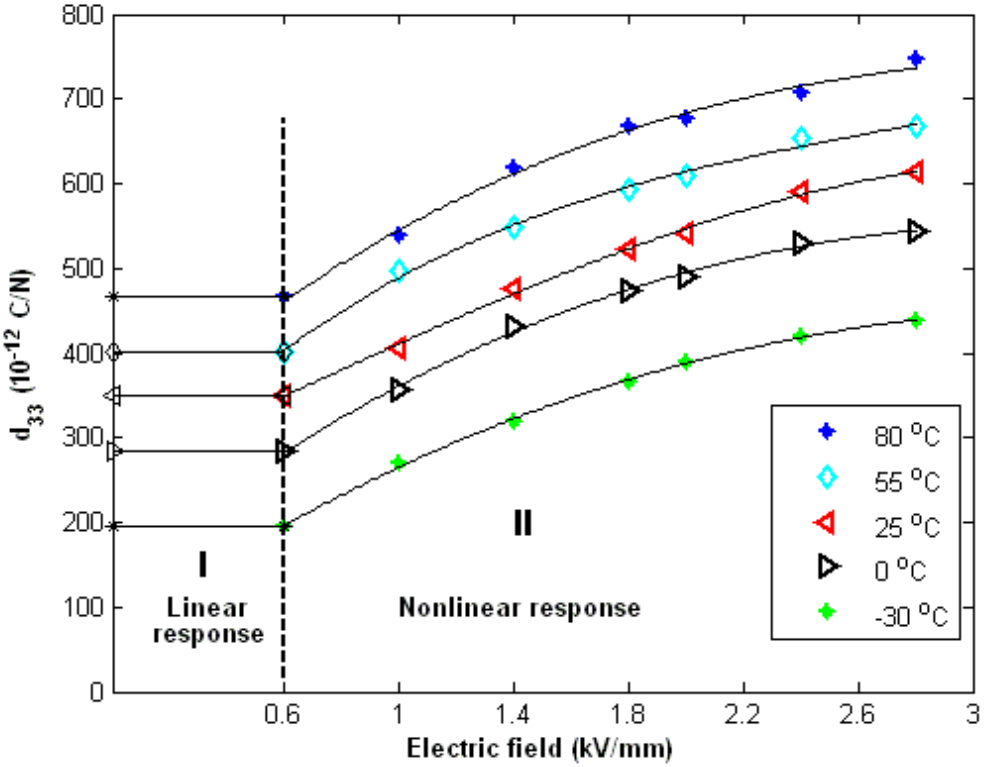

Figure 2.10. Variation of piezoelectric coefficient d_{33} with electric-field magnitude (100 Hz and 10 % duty cycle).

Zhang et al. [19] stated that the change in piezoelectric coefficients with temperature is due to intrinsic and extrinsic contributions, with intrinsic piezoelectric contributions of less than 37% at room temperature. Intrinsic properties are material properties from a single-domain material, while extrinsic properties are mainly from domain walls. They also stated that the extrinsic piezoelectric contributions increased rapidly with temperature as a result of non-180^{o} domain walls. Therefore, it can be concluded that for

the actuator being considered in this study, at low driving-field magnitudes ≤ 0.6 kV/mm (Figure 2.10, region I), the linear change of the piezoelectric coefficient with ambient temperature was mainly caused by extrinsic contributions due to domain walls, which were driven by temperature. At higher electric-field magnitudes (Figure 2.10, region II), an additional extrinsic part was introduced to account for the increased activities of non-180^{o} domain walls caused by high electric-field magnitudes. Figure 2.11 is a re-plotting of Figure 2.10 to delineate the variation of d_{33} with ambient temperature, and shows that d_{33} was linearly dependent on temperature, which is in good agreement with the results obtained by Zhang et al. [19, 20].

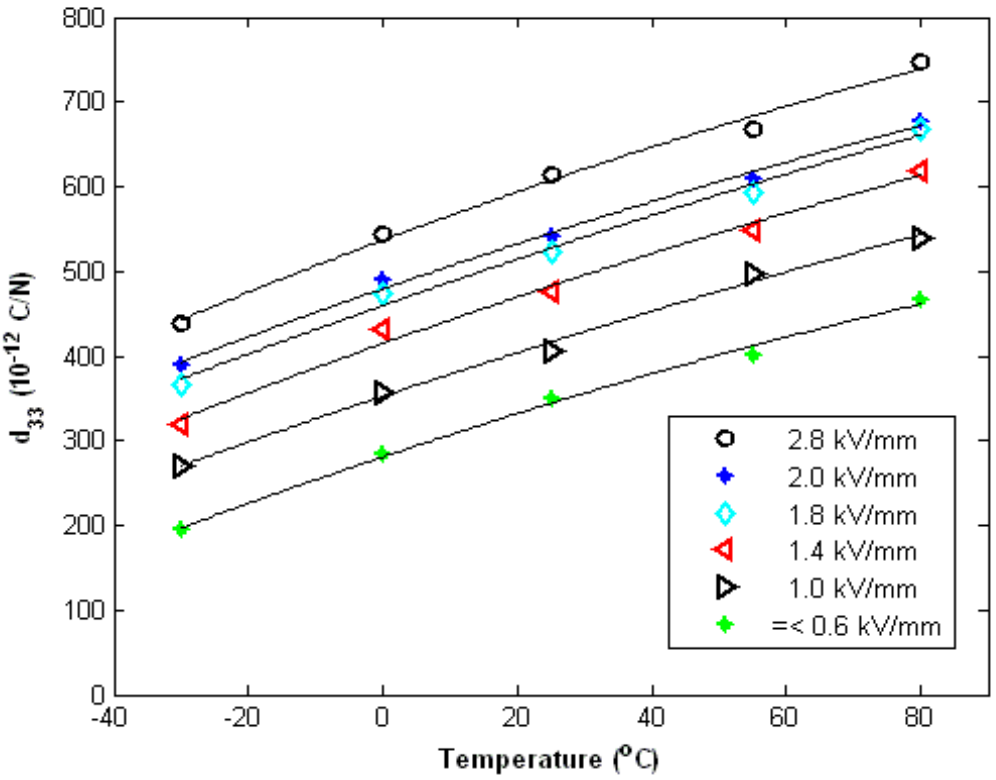

Figure 2.11. Variation of piezoelectric coefficient d_{33} with ambient temperature (100 Hz and 10 % duty cycle).

The effect on the longitudinal piezoelectric coefficient of changing DC offset was also investigated by applying different DC positive bias voltages. Figure 2.12 shows the biased DC offset dependence found of d_{33} under a sinusoidal peak-to-peak electric-field magnitude ranging from 0.6 to 2.0 kV/mm, a frequency of 100 Hz, and a duty cycle of 10% at room temperature. For low electric-field magnitudes less than 1.0 kV/mm, the DC offset was found to have almost no effect on d_{33}. At driving-field magnitudes of 1.0 kV/mm and above, the longitudinal piezoelectric coefficient decreased slightly with the positive DC offset, which is in good agreement with the results obtained by Masys et al. [18]. Masys et al. [18] reported that a positive bias field does not increase the total polarization, but does contribute to pinning of the domain walls and hence reduces the extrinsic contribution to the piezoelectric response.

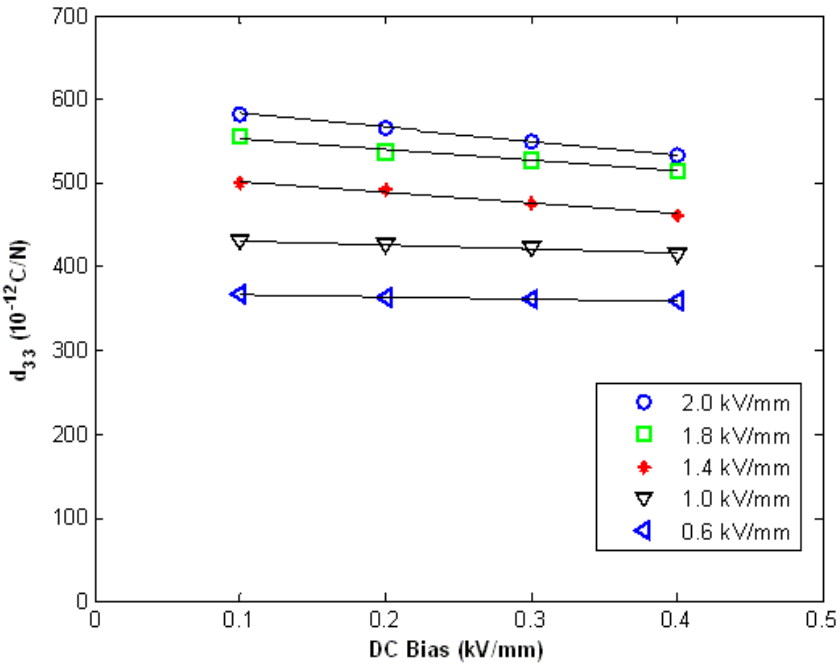

Figure 2.12. Variation of d_{33} with DC offset under different sinusoidal driving field magnitudes at room temperature (100 Hz and 10 % duty cycle).

2.4. Heat Generation and Hysteresis in PZT Actuators

Heat generation in PZT actuators was also investigated since it was observed that a significant amount of heat is generated when PZT actuators are driven under high electric-field magnitudes and/or high frequencies. Heat generation can significantly affect the reliability and piezoelectric properties of these actuators, and may also limit their application. Heat generation in multi-layer PZT actuators is considered to be caused by losses, such as mechanical loss and dielectric loss [21]. However, it has been assumed in the literature to date that the major contribution to heat generation is from dielectric loss which is caused by ferroelectric hysteresis loss [22-24].

The effect of the electric-field magnitude and of ambient temperature on displacement-electric field loss (displacement hysteresis) is shown in Figure 2.13(a-c) and (d-f), at temperatures of -30 ^{o}C and 80^{o}C, respectively, and a driving frequency of 1 Hz using a sinusoidal wave form. At electric-field magnitudes less than 0.6 kV/mm, there was almost no hysteresis at both temperatures. On the other hand, for higher electric-field magnitudes, hysteresis increased due to increased activities of non-180^{o} domain walls with increasing temperature and electric-field magnitude. As mentioned by Zhang et al. [20], mathematical modeling of hysteresis and irreversible behavior in ferroelectric materials is rather complicated. According to them and to Masys et al. [18], most of the observed nonlinearities and hysteresis in the material response are due to extrinsic contributions from the domain-boundary motion and phase-boundary motion.

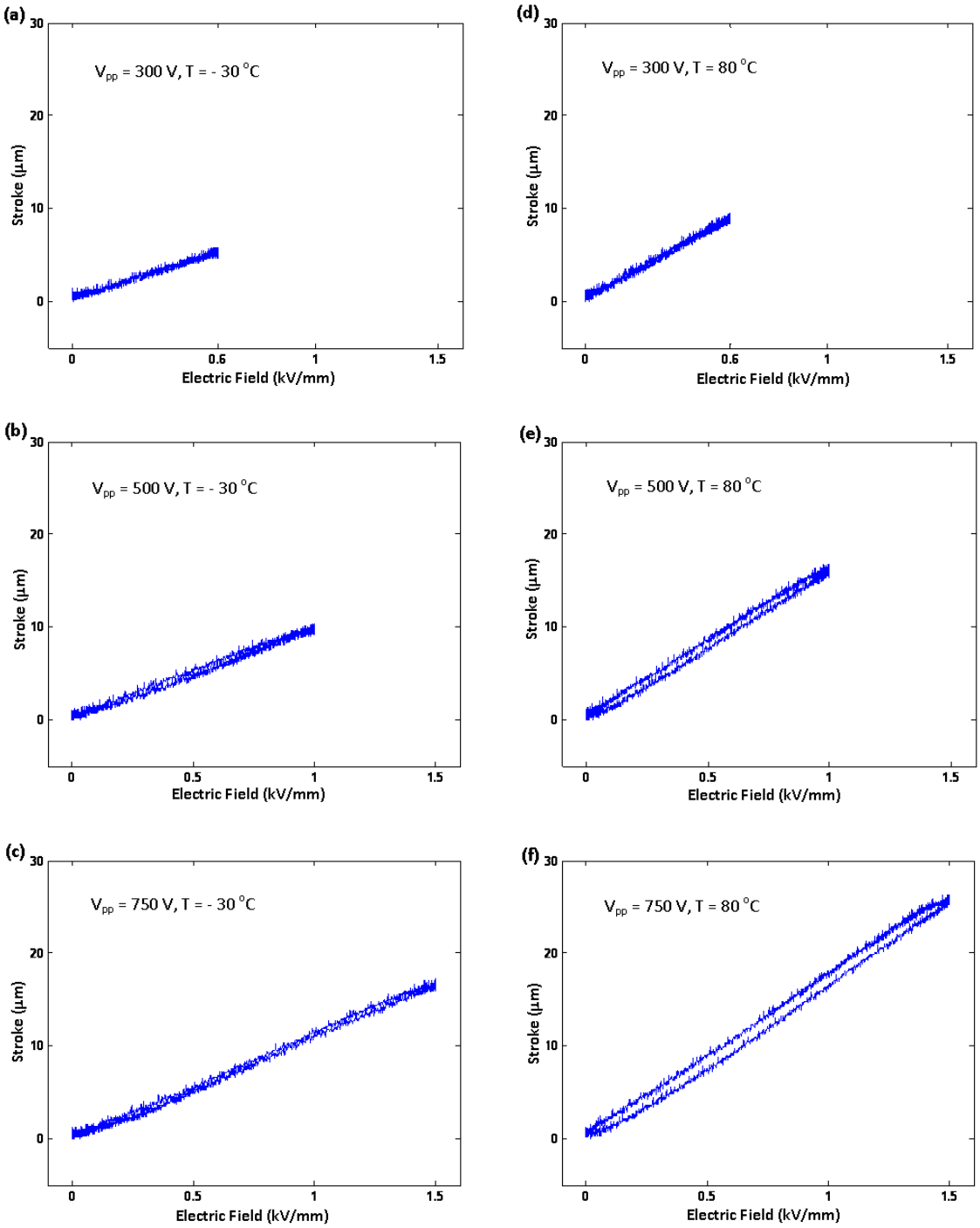

Figure 2.13. Effect of electric-field magnitude on hysteresis at two different temperatures (a-c) -30 °C, (d-f) 80 °C (sinusoidal wave form at 1 Hz).

For the purpose of heat generation testing in the current study, a 10-minute continuous loading cycle was used. The temperature increase of the selected actuators under a continuous sinusoidal AC driving field (i.e., 100% duty cycle) is shown in Figure 2.14 for different frequencies up to 300 Hz, and different electric-field magnitudes (0.6, 1.0, and 1.4 kV/mm). All tests were conducted at room temperature, with 25 ^{o}C as the reference temperature T_0 (ambient temperature inside the chamber). The temperature increase, δT, is defined as $(\delta T=T_i-T_0)$, where T_i is the measured temperature of the actuator surface.

It can be seen from Figure 2.14 that self-heat generation in the PZT actuators tested increased with increasing electric-field magnitude and frequency. The temperature increase in actuators showed an initially increasing trend and then reached a steady state temperature. The time at which the steady state was achieved, as well as the value of the steady state temperature, was governed by the electric-field magnitude and frequency. For instance, for E = 1.4 kV/mm and f = 300 Hz, the steady state temperature was almost $60^{o}C$, while for E = 0.6 kV/mm and f = 100 Hz, the steady state temperature was close to 1.5 ^{o}C. Since the dynamic stroke was found to be dependent on ambient temperature, one can expect the dynamic stroke to increase with time as the actuator temperature increases, as shown in Figure 2.15. Note that the increase in stroke here is due to two sources: (1) self-heat generation which increases the extrinsic piezoelectric contribution, non-180^{o} domain switching-induced strain; and (2) thermal strain.

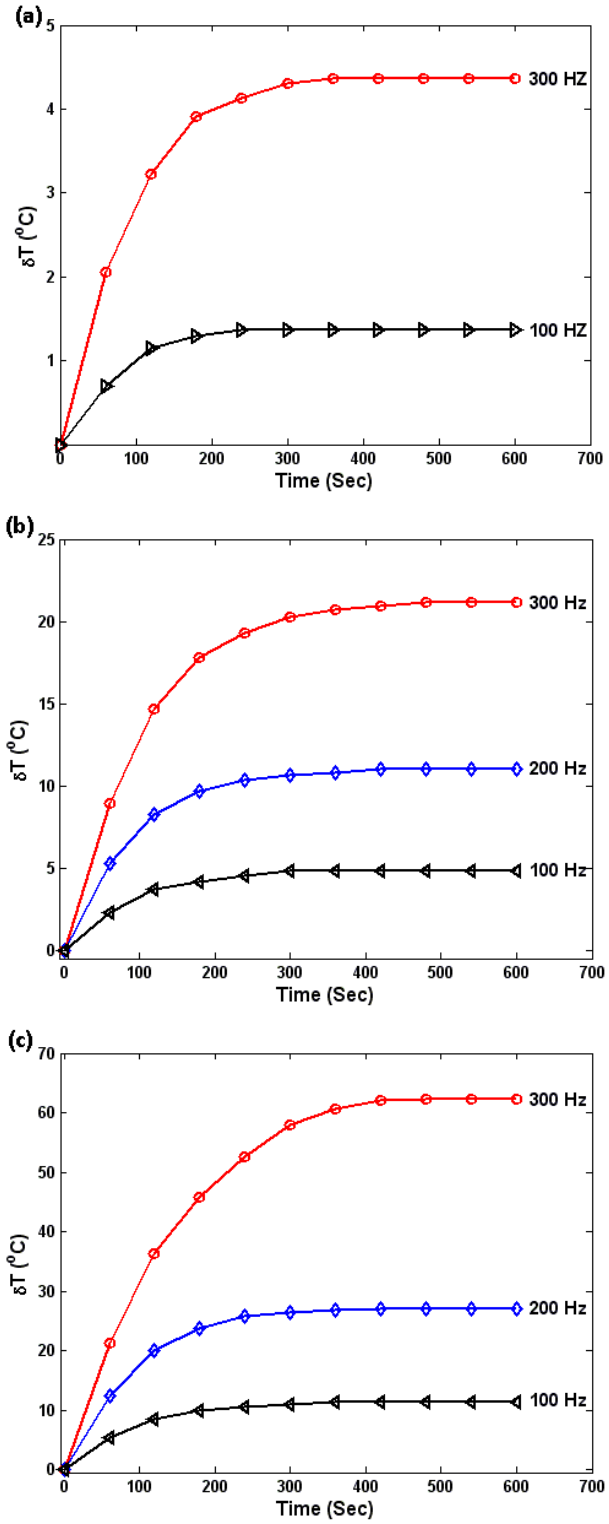

Figure 2.14. Temperature increase with time under different frequencies and continuous sinusoidal electric fields (a) 0.6 kV/mm, (b) 1.0 kV/mm, and (c) 1.4 kV/mm.

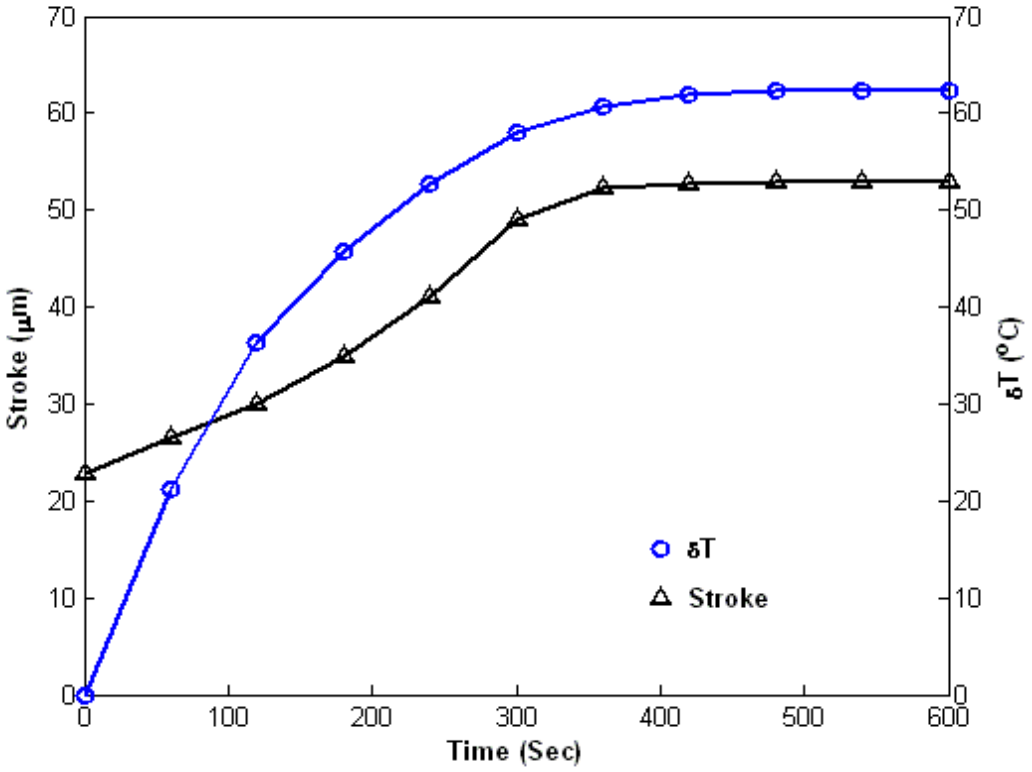

Figure 2.15. Variation of dynamic stroke with time under dynamic driving conditions (E = 1.4 kV/mm, f = 300 Hz, and 100 % duty cycle).

The variation of the steady state temperature increase $\delta T\infty$ with frequency is shown in Figure 2.16 for different driving electric-field magnitudes and a 100 % duty cycle. For driving-field magnitudes less than 0.6 kV/mm, the steady state temperature increase was linearly proportional to the driving-field frequency. However, as the magnitude of the electric field increased, the temperature-frequency relation was no longer linear. A power law fit using the least-squares technique was used to depict the steady state temperature-frequency relation such that $\delta T_\infty = af^b$ (where a and b are functions of the applied electric field, and $b \geq 1.0$).

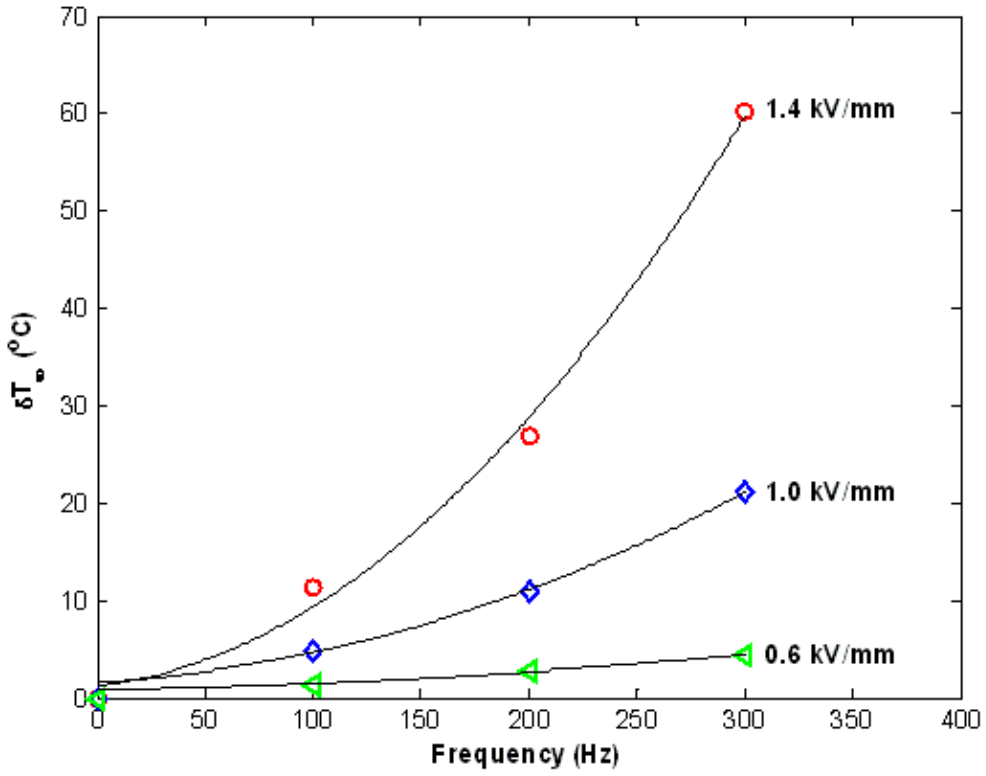

Figure 2.16. Variation of steady state temperature increase with frequency for different electric-field magnitudes.

Self-heat generation in piezoelectric actuators was also found to depend on electric-field magnitude. Figure 2.17 shows the dependence of the steady state temperature increase of the actuators tested on electric-field magnitude. For driving field frequencies less than 100 *Hz*, the steady state temperature increase was almost linearly proportional to the electric-field magnitude. As the frequency increased (≥100 *Hz*), a nonlinear trend was observed with δT_∞ being almost proportional to E^3.

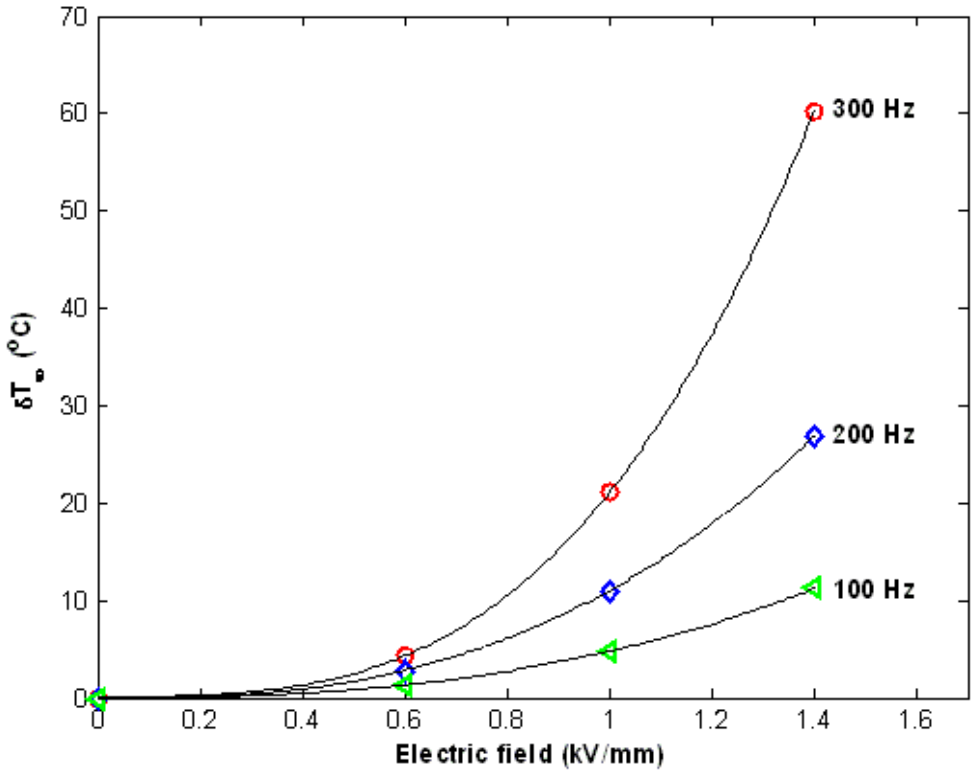

Figure 2.17. Variation of steady state temperature increase with electric-field magnitude for different frequencies.

Although duty cycle did not affect the dynamic stroke, as it was shown in Section 2.3, it significantly affected self-heat generation under dynamic operating conditions. For example, doubling the duty cycle nearly doubled the steady state temperature increase. Figure 2.18 shows the dependence of the temperature increase on duty cycle for different loading frequencies at E = 1.4 kV/mm. Steady state temperature increase in piezoelectric actuators was found to be linearly dependent on duty cycle, as shown in Figure 2.19. Decreasing duty cycle significantly decreased the heat generated in the piezoelectric actuators tested. Thus decreasing the duty cycle can improve the functionality of these actuators and lead to their expanded use in high-power applications.

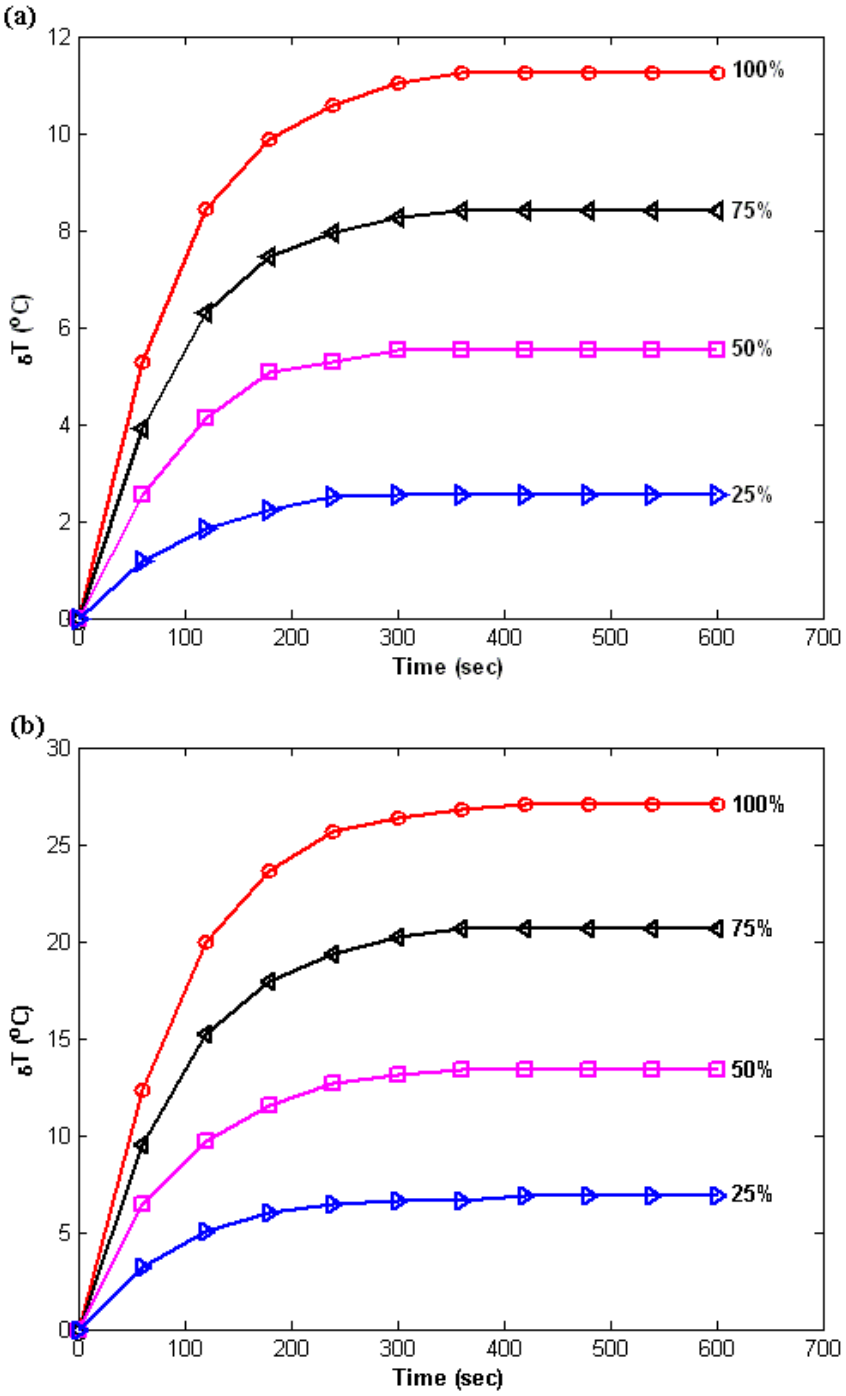

Figure 2.18. Variation of temperature increase with time under different duty cycles at two different frequencies (a) 100 Hz, and (b) 200 Hz [E = 1.4 kV/mm].

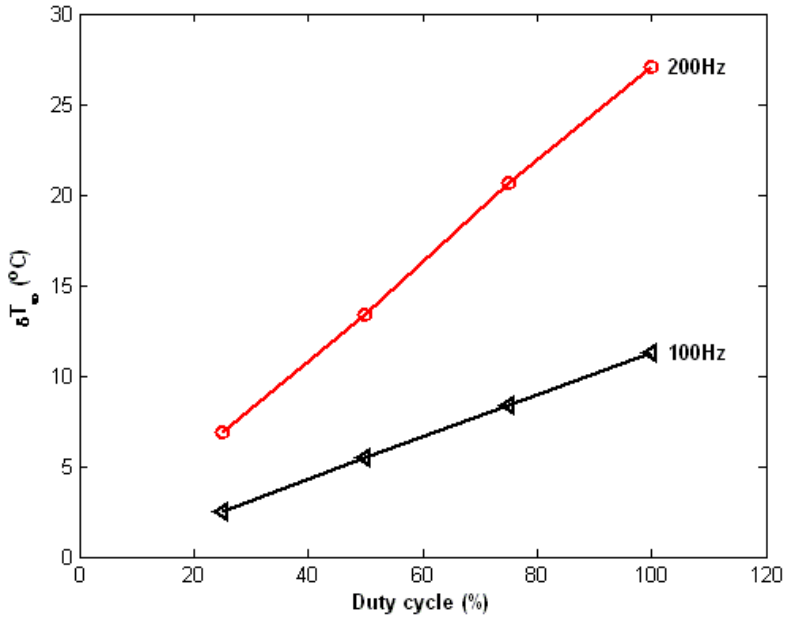

Figure 2.19. Dependence of steady state temperature increase on duty cycle percentage (E = 1.*4* kV/mm).

Zheng et al. [22] proposed a theoretical model to explain the mechanism of heating in piezoelectric materials. The model was based on the law of energy conservation, and the assumption that the rate of heat generation is directly proportional to the frequency and hysteresis loss per driving cycle per unit volume. Polarization-electric field hysteresis was found to be approximately proportional to E^2 and linearly proportional to frequency f. The mathematical model represents a closed-form solution for temperature increase that shows the classical exponential variation with respect to time, as well as a steady state value. However, since the dependence of hysteresis on duty cycle and ambient temperature was not considered in the model, it cannot be used to simulate the results of Figures 2.14:19. In Chapter 3, a mathematical model that accounts for the effects of duty cycle, as well as the dependency of piezoelectric losses on ambient temperature, electric-field magnitude, and frequency is presented.

2.5. Conclusions

The thermo-electro-mechanical performance of piezoelectric stack actuators under different operating conditions relevant to fuel injection was investigated in this chapter. Soft epoxy-bonded PZT stack actuators were tested over a temperature range of -30 ^{o}C to 80 ^{o}C, under sinusoidal and trapezoidal driving fields of up to 2.0 kV/mm with various frequencies, rise times, and duty cycles. The effect of the biased DC offset voltage on the dynamic performance of PZT stacks was also studied. The biased DC offset was found to slightly affect the dynamic stroke of PZT actuators by reducing the extrinsic contribution due to non-180^{o} domain walls. Below the resonance frequency of the testing system (about 500 Hz), the dynamic stroke was found to increase with driving-field frequency. In the case of the trapezoidal loading field, a decrease in rise time increased the non-180^{o} domain wall motions; decreasing the rise time was found to be equivalent to increasing the frequency (i.e., dynamic stroke increased with decreasing rise time). Self-heat generation in the actuators was also investigated for different combinations of electric-field magnitude, frequency, and duty cycle. Heat generation increased with increased driving-field magnitude and driving-field frequency. Although duty cycle had almost no effect on dynamic stroke, it strongly affected heat generation in the actuators. Decreasing the duty cycle can significantly decrease heat generated in the actuators. At driving-field frequencies much lower than the resonance frequency of the system, the stroke- electric field behavior at different temperatures agreed well with the quasi-static results obtained previously.

2.6. Bibliography

[1] Scharf A. Prize-Winning Piezo. *Piezo-actuators in fuel injection systems, EPCOS technical articles*, 2006.

[2] Gromek B, Shen JJ. Multiple stack piezoelectric actuator for a fuel injector. *United States Patent, Patent Number 6,345,771*, 2000.

[3] Takase S. Piezoelectric actuator and fuel-injection apparatus using the actuator. *United States Patent, Patent Number 6-155-500*, 1999.

[4] Boecking F, Sugg B. Piezo Actuators: A technology prevails with injection valves for combustion engines. *10th International Conference on New Actuators,* 2006:171.

[5] Fujii A, Toyao T. Piezoelectric actuators with high reliability for diesel injection valve. *10th International Conference on New Actuators,* 2006:177.

[6] Andersen B, Ringgaard E, Bove T, Albareda A, Pérez R. Performance of piezoelectric ceramic multilayer components based on hard and soft PZT. *7th International Conference on New Actuators* 2000:419.

[7] Andersen B, Ringgaard E, Nielsen LS. Static and Dynamic Performance of Stacked Multilayer Actuators Based on Hard and Soft PZT. *7th International Conference on New Actuators* 2000:423.

[8] Ardelean EV, Cole DG, Clark RL. High performance "V-stack" piezoelectric actuator. *Journal of Intelligent Material Systems and Structures* 2004;15:879.

[9] Heinzmann A, Hennig E, Kolle B, Kopsch D, Richter S, Schwotzer H, Wehrsdorfer E. Properties of PZT Multilayer Actuators. *8th International Conference on New Actuators* 2002.

[10] Li FX, Rajapakse RKND, Mumford D, Gadala M. Quasi-static thermo-electro-mechanical behaviour of piezoelectric stack actuators. *Smart Materials and Structures* 2008;17:015049.

[11] Yao K, Uchino K, Xu Y, Dong S, Lim LC. Compact piezoelectric stacked actuators for high power applications. *IEEE Transactions on Ultrasonics, Ferroelectrics, and Frequency Control* 2000;47:819.

[12] Lynch CS. Electro-mechanical coupling in 8/65/35 PLZT. *9th IEEE International Symposium* 1994:357.

[13] Lynch CS. The effect of uniaxial stress on the electro-mechanical response of 8/65/35 PLZT. *Acta Materialia* 1996;44:4137.

[14] Lynch CS, Chen W, Liu T. Multiaxial constitutive behavior of ferroelectric materials. *International Society for Optical Engineering* 2000;3992:245.

[15] Lindner DK, Vujic N, Leo DJ. Comparison of drive amplifier for piezoelectric actuators. 2001;4332:281.

[16] Sherrit S, Van Nice DB, Graham JT, Mukherjee BK, Wiederick HD. Domain wall motion in piezoelectric materials under high stress. *ISAF'92., Proceedings of the Eighth IEEE International Symposium on Applications of Ferroelectrics* 1992:167.

[17] Strukov BA, Levanyuk AP. Ferroelectric phenomena in crystals: physical foundations. *Springer*. 1998.

[18] Masys AJ, Ren W, Yang G, Mukherjee BK. Piezoelectric strain in lead zirconate titante ceramics as a function of electric field, frequency, and dc bias. *Journal of Applied Physics* 2003;94:1155.

[19] Zhang QM, Wang H, Kim N, Cross LE. Direct evaluation of domain-wall and intrinsic contributions to the dielectric and piezoelectric response and their temperature dependence on lead zirconate-titanate ceramics. *Journal of Applied Physics* 1994;75:454.

[20] Zhang QM, Wang H, Zhao J. Effect of Driving Field and Temperature on the Response Behavior of Ferroelectric Actuator and Sensor Materials. *Journal of Intelligent Material Systems and Structures* 1995;6:84.

[21] Ochi A, Takahashi S, Tagami S. Temperature Characteristics for Multilayer Piezoelectric Ceramic Actuator. *Japanese Journal of Applied Physics* 1985;24:209.

[22] Zheng J, Takahashi S, Yoshikawa S, Uchino K, de Vries JWC. Heat generation in multilayer piezoelectric actuators. *Journal of the American Ceramic Society* 1996;79:3193.

[23] Lesieutre GA, Fang L, Koopmann GH, Pai SP, Yoshikawa S. Heat generation of a piezoceramic induced-strain actuator embedded in a glass/epoxy composite panel. 1996;2717:267.

[24] Uchino K, Hirose S. Loss mechanisms in piezoelectrics: How to measure different losses separately. *IEEE Transactions on Ultrasonics, Ferroelectrics, and Frequency Control* 2001;48:307.

Chapter 3

3. Self-Heat Generation in Piezoelectric Stack Actuators*

3.1. Introduction

The ability of piezoelectric ceramics to generate mechanical displacement as a result of electric charge makes them suitable materials for use in actuation applications [1-3]. A review on shape control of non-piezoelectric structures by piezoelectric actuation was presented by [4]. Piezoelectric materials are also used in many engineering applications as sensors because of their direct piezoelectricity [5, 6]; that is, they generate an electric charge as a result of mechanical deformation. They have also been used in such diverse applications as information technology, biomedical engineering, and energy engineering [7]. In actuation applications that require fast, reliable and precise actuation performance, piezoelectric materials are intended to be used at high electric field magnitudes and/or high frequencies. The co-fired multilayer stack actuator is a key element in these applications. It consists of thin piezoelectric discs (roughly 0.1 mm to 0.5 mm thick) bonded together and sandwiched between electrodes, with adjacent discs having opposite poling directions, and generates relatively large displacement with a low driving voltage.

* "A version of this chapter has been published. **Senousy, M. S.,** Rajapakse, R.K.N.D., Mumford, D., and Gadala, M.S. (2009) Self-Heat Generation in Piezoelectric Stack Actuators Used in Fuel Injectors, *Journal of Smart Materials and Structures*, Vol. 18, No. 4.

The low driving voltage, high energy density, low power consumption, precise positioning, quick response, and long lifetime of piezoelectric stack actuators make them potential candidates for use in fuel injection systems [8, 9]. Moreover, using piezoelectric stack actuators in fuel injection systems is preferable to conventional solenoid technology because they provide an optimized injection system (i.e., quieter, more economical, more powerful, reduced emissions).

Since piezoelectric stack actuators are competitive candidates for clean engine technology, it is important to examine their performance and reliability under conditions that simulate the actual operating conditions of a fuel injector (i.e., electric field magnitude >1.5 kV/mm, frequency range of 10 to 100 Hz, and operating temperature range of -40 ^{o}C to 120 ^{o}C). The dynamic thermo-electro-mechanical performance of cylindrical PZT actuators manufactured by Kinetic Ceramics Inc. (KCI, *www.kineticceramics.com*) has been experimentally investigated by the authors [10] over a temperature range of -30 ^{o}C to 80 ^{o}C. The results showed that PZT stack actuators tend to generate heat when they are driven under high electric-field magnitudes and/or high frequency. This heat may significantly affect the lifetime, durability and positioning accuracy of the actuators, and degradation of the material properties may also occur [11]. Therefore, self heating in piezoelectric stack actuators represents a major challenge in utilizing them in dynamically loaded systems such as fuel injectors.

Although the experimental study of the static and dynamic behavior of piezoelectric stack actuators has received some attention (i.e.,[12-16]), only a limited number of experimental studies addressing the self-heating problem have been published [17-20]. Heat generation in different sizes of piezoelectric actuators under different operating

conditions at room temperature was investigated by [21]. They also proposed a theoretical model to explain the mechanism of heating in piezoelectric materials. The model was based on the law of energy conservation, and the assumption that the rate of heat generation is directly proportional to the frequency and hysteresis loss per driving cycle per unit volume. The dependence of hysteresis on ambient temperature was not considered in this model. A similar mathematical model to explain the mechanism of heating in piezoelectric materials was proposed by [22]. The main difference between the presented mechanisms was the inclusion of heat dissipation from the actuator by only convection [22] or by convection and radiation [21].

In this chapter, an experimental study of the effect of various controlling parameters relevant to fuel injection on self heating is presented. Electric-field magnitude and frequency are dominant parameters in controlling the amount of heat generated in PZT actuators. Actuator geometry is another significant factor; increasing surface area can significantly decrease actuator temperature increase. Duty cycle and fuel type are also significant factors. A theoretical model, based on the first law of thermodynamics, that explains the mechanism of heating in piezoelectric materials and accounts for these controlling parameters is also developed. The model is based on measurement of displacement-electric field loss (displacement hysteresis).

A detailed description of the experimental setup is presented in Section 3.2. In Section 3.3, the effects of electric-field magnitude, frequency, and temperature on displacement hysteresis are experimentally investigated. The effects of electric-field magnitude, frequency, and duty cycle on heat generation are also examined. The developed

analytical model is then presented in Section 3.4 and a comparison between the mathematical and the experimental results is provided in Section 3.5.

3.2. Experimental Setup

The experimental investigation aimed at assessing the characteristics of self heating in piezoelectric actuators over a wide range of controlling parameters related to direct-fuel injection. Different controlling parameters were employed to obtain a better understanding of the heating mechanisms of the actuators: electric-field magnitude E ($E=V_{pp}/t_h$, where V_{pp} is the applied peak-to-peak voltage and t_h is the thickness of a single layer); frequency f; duty cycle d_t; and surrounding properties (i.e., fuel type, using heat sink, etc.).

The test stand (shown in Figure 3.1) was placed inside a thermal chamber (*TestEquity Model 1007C*) with a temperature feedback control of 0.1 ^{o}C. The temperature of the actuator was measured through a Resistance Temperature Detector (*RTD*) attached to the surface of the actuator. In injector applications, the piezo actuators are subjected to a compressive preload for alignment and other design requirements. It was found by [14] that a preload of 0-40 MPa had a negligible effect on actuator response. Additionally, it was reported by [18] that self heating in piezoelectric actuators is slightly independent of load. The actuators in the current study were therefore subjected to a constant compressive preload of 5 MPa throughout the testing, applied using a soft spring (30 N/mm) fixed by a screw nut. The preload was measured using a force sensor placed between the shaft and the moving loading head, which was in direct contact with the actuator. The other end of the actuator was placed on a fixed plate, allowing the

displacement to be measured using a Linear Variable Displacement Transducer (*LVDT*), with a resolution of 0.1 μm.

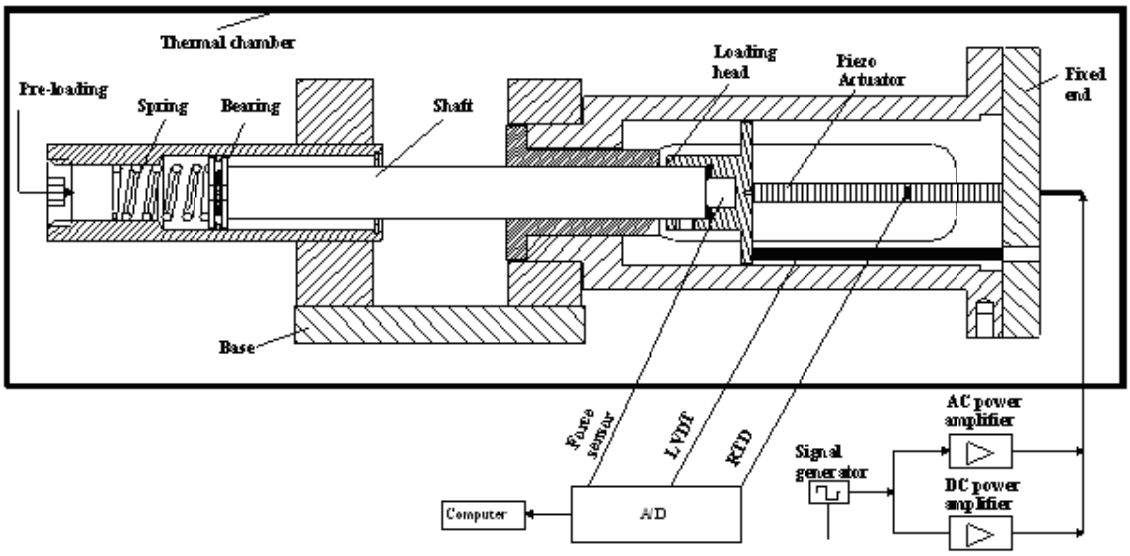

Figure 3.1. Test setup.

The test procedure consisted of the following steps: (1) aligning the actuator with the centre of the shaft and the loading head; (2) preloading the actuator using a screw nut through a spring; (3) choosing the desired electric-field magnitude and frequency using the signal generator; (4) switching the power amplifier on and adjusting the DC offset; (5) firing the actuator for 10 minutes; and (6) recording data every 60 seconds. The actuators were subjected to continuous loading for 10 minutes to give them enough time to reach a steady state temperature.

Custom-made PZT multi-layer stack actuators manufactured by Kinetic Ceramics Inc. were used in this study. Table 3.1 shows the geometry and material properties of the actuators used in this study. The actuators are made from soft PZT ceramics, and have a Curie temperature above 360 ^{o}C. Soft PZT ceramics have a higher dielectric loss factor

tanδ than hard PZT ceramics, which promotes a higher heat generation under large electric-field magnitude and/or frequency, a higher piezoelectric coefficient d, and a lower coercive field E_c. Although soft PZT ceramics tend to generate higher self heating than harder PZT ceramics [20], they are advantageous for actuator applications because they produce a greater strain in response to an applied electric field.

Table 3.1. KCI piezoelectric properties.

Property	*Value*
Actuator diameter (mm)	5
Actuator length (mm)	30
Layer thickness (mm)	0.5
Number of layers (stacks)	54
Capacitance (nF)	69
Maximum operating voltage (Volts)	1000
Maximum operating electric field (kV/mm)	2.0
Longitudinal piezoelectric coefficient d_{33} (pC/N)	370
Young's Modulus Y_{33} (GPa)	48
Heat Capacity c (J/kg^{o}C)	420

3.3. Self-Heat Generation and Hysteresis in PZT Actuators

Self heating in PZT actuators is considered to be caused by losses, such as mechanical loss and dielectric loss, with the major contribution from dielectric loss caused by ferroelectric hysteresis loss [23, 24]. It was also found by [25] that at large unipolar electric-field magnitudes, dielectric loss (polarization hysteresis) can be directly related to piezoelectric loss (displacement hysteresis). Therefore, without loss of generality, self heating in PZT actuators can be said to be directly related to dielectric loss and/or piezoelectric loss. These losses can be ascribed to domain wall motion, lattice distortion, and microstructural evolution.

The effects of electric-field magnitude and temperature on displacement hysteresis found in the current study are shown in Figure 3.2, at temperatures of -30 ^{o}C, 55 ^{o}C, and 80 ^{o}C, respectively, and a duty cycle of 100%, using a sinusoidal wave form. Displacement hysteresis, D_f, is represented by the hysteresis area and defined as the loss of the sample per electric charge per driving cycle. Figure 3.3(a) shows the dependence of displacement hysteresis on electric-field magnitude over a temperature range of -30 ^{o}C to 80 ^{o}C under a sinusoidal driving-electric field, and a duty cycle of 100%. At low temperatures (< 0 ^{o}C), displacement hysteresis was almost linearly proportional to the driving-field magnitude. As temperature increased (≥ 0 ^{o}C), a nonlinear trend was observed. At low temperatures, the hysteresis due to domain walls were driven by electric field, while at higher temperatures, an additional extrinsic contribution was due to increased activities of non-180^{o} domain walls caused by temperature.

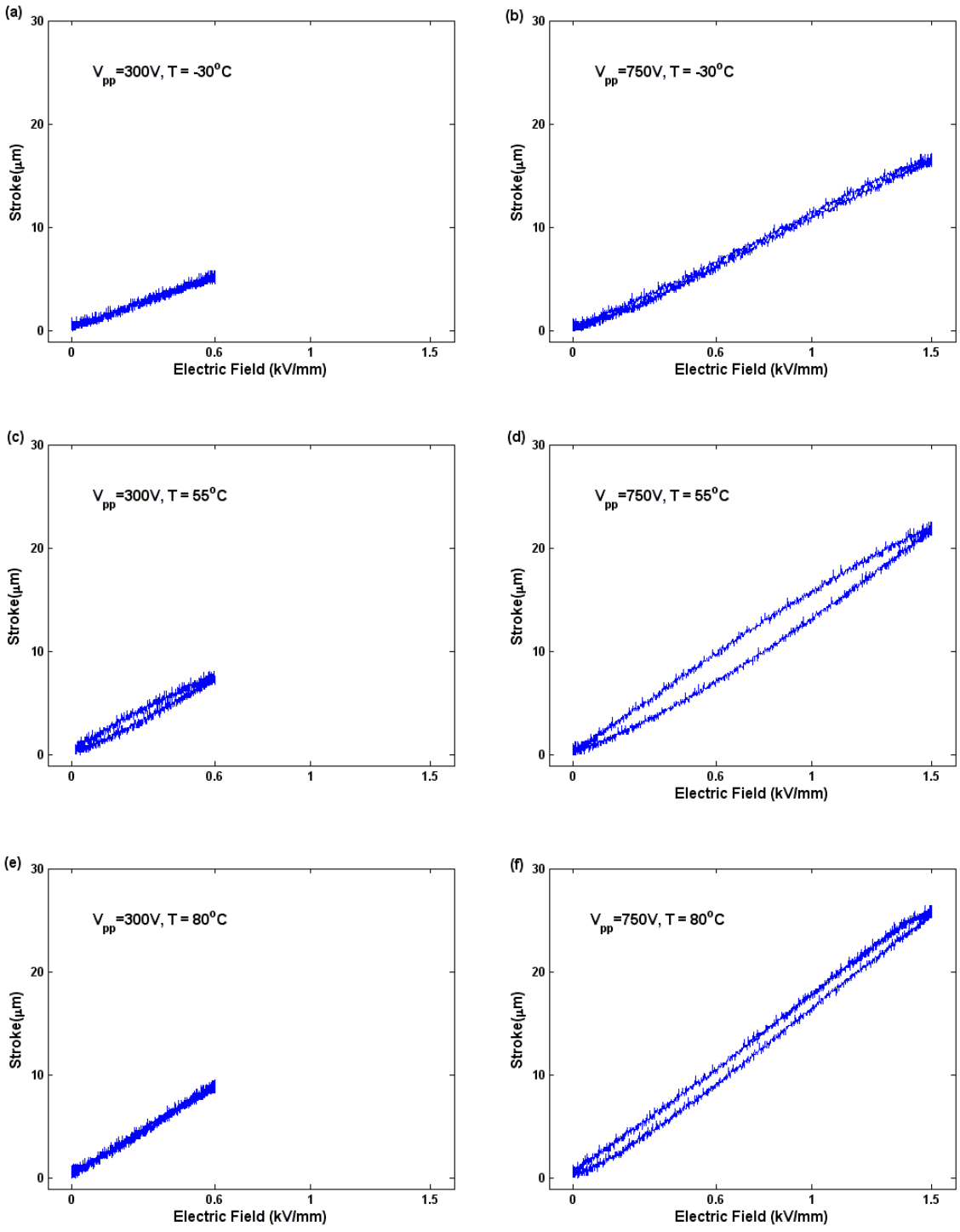

Figure 3.2. Effect of electric-field magnitude on displacement hysteresis at different temperatures (sinusoidal wave form at 100% duty cycle).

Figure 3.3(a) is re-plotted in Figure 3.3(b) to delineate the variation of D_f with temperature at different electric-field magnitudes. Hysteresis-temperature curves can be linearly fitted as shown in Figure 3.3(b); the dashed lines represent linear fitting excluding hysteresis at a temperature of 55 ^{o}C, while the solid lines represent the actual measured values. At low electric-field magnitude (0.6 kV/mm), there was a slight, almost negligible change in displacement hysteresis with temperature; at higher electric-field magnitudes, a noticeable change in displacement hysteresis with temperature was observed. However, at all electric-field magnitudes, a displacement hysteresis maxima was observed at a temperature of 55 ^{o}C, which may be interpreted as a microstructural evolution in the actuator's material occurring around this temperature and causing the hysteresis to increase. In Chapter 2, a nonlinear transition zone in stroke-temperature behavior was observed between 40 ^{o}C and 55 ^{o}C, which is consistent with the nonlinear hysteresis maxima observed here at 55 ^{o}C.

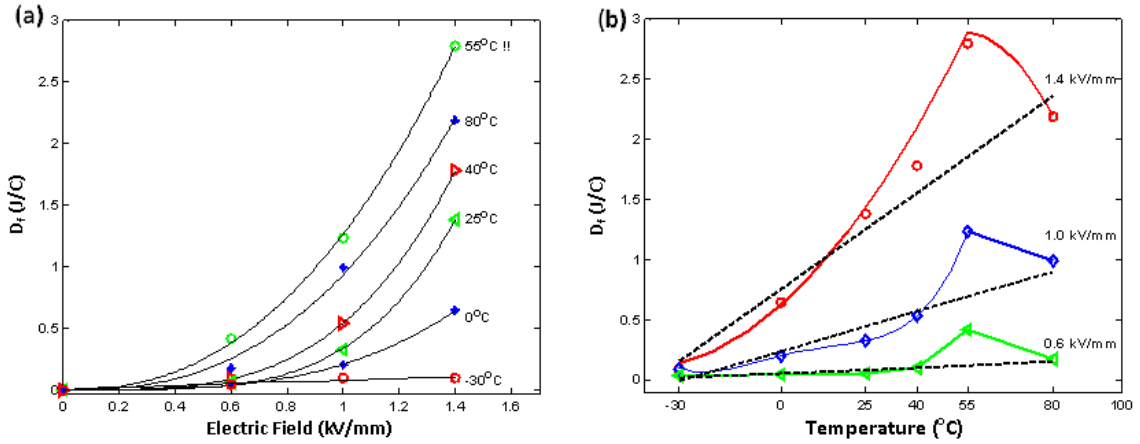

Figure 3.3. Variation of displacement hysteresis D_f with (a) electric-field magnitude, (b) temperature (sinusoidal wave form at 100 % duty cycle).

In the current investigation, displacement hysteresis D_f was also found to be slightly independent of frequency. Figure 3.4 shows the dependence of displacement hysteresis on frequency found under an electric-field magnitude of 1.4 kV/mm at room temperature. Displacement hysteresis was almost constant with frequency, with a standard deviation percentage of 2.5 %. Therefore, in the analytical self-heating model presented in the following section, hysteresis variation with frequency is neglected.

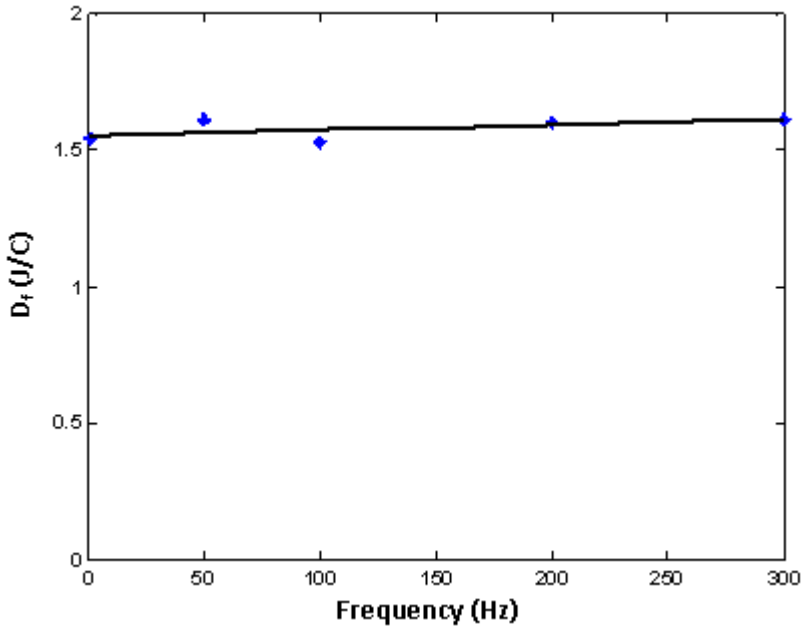

Figure 3.4. Variation of displacement hysteresis with frequency

(E = 1.4 kV/mm at room temperature).

The temperature increase of the selected actuators under a continuous sinusoidal AC driving field (i.e., 100 % duty cycle) is shown in Figure 3.5 for different frequencies up to 300 Hz, and for two different electric-field magnitudes. All tests were conducted at room temperature, with 25 ^{o}C as the reference temperature T_0 (ambient temperature inside the chamber), and continuous loading for 10-minutes. The temperature increase,

δT, is defined as ($\delta T=T_i-T_0$), where T_i is the measured temperature of the actuator surface.

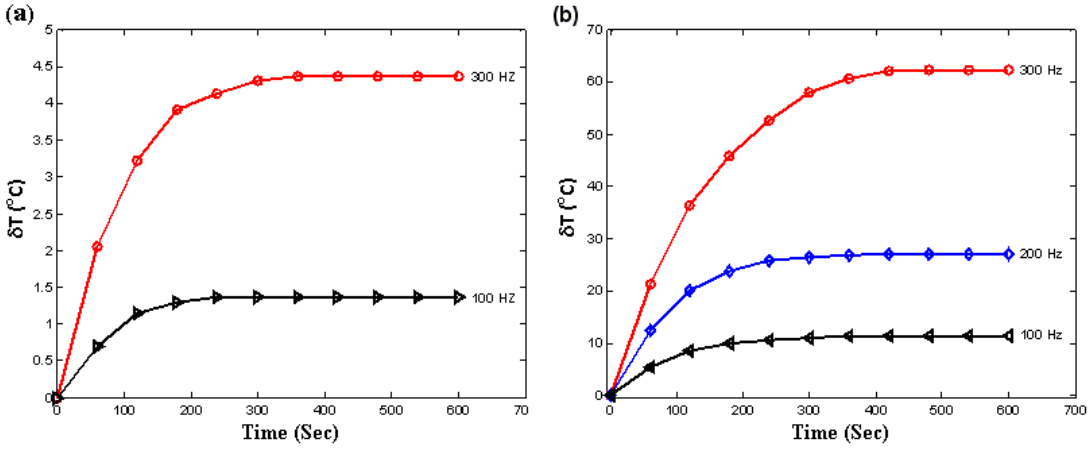

Figure 3.5. Variation of temperature increase with time under different frequencies and continuous sinusoidal electric field of (a) 0.6 kV/mm, (b) 1.4 kV/mm.

It can be seen from Figure 3.5 that self-heat generation in the PZT actuators tested increased with increasing electric-field magnitude and frequency. At low electric-field magnitudes, the low level of self heating is due to molecular friction [26]. Increasing electric-field magnitude introduces a source of extrinsic contributions due to increased activities of non-180^o domain walls. As a result, an increase in hysteresis occurs, resulting in self heating in the PZT actuators. It can also be seen that the temperature increase in the actuators showed an initially increasing trend and then reached a steady state temperature. Duty cycle was also found to significantly affect self-heat generation under dynamic operating conditions. Duty cycle is defined as the ratio between the period of a single sinusoidal pulse and the period of a complete voltage cycle. Figure 3.6 shows the dependence of temperature increase on duty cycle under frequencies of 100 Hz and 200 Hz, respectively, at E = 1.4 kV/mm. At both frequencies, increasing duty cycle

significantly increased the amount of heat generated in the PZT actuators. Self heating in PZT actuators is linearly dependent on duty cycle percentage, as shown in Figure 3.7. Since reducing the duty cycle percentage significantly decreased the amount of heat generated within the actuators, it can be concluded that decreasing the duty cycle can improve the functionality of these actuators and lead to their expanding use in applications that operate at high electric field and frequency levels.

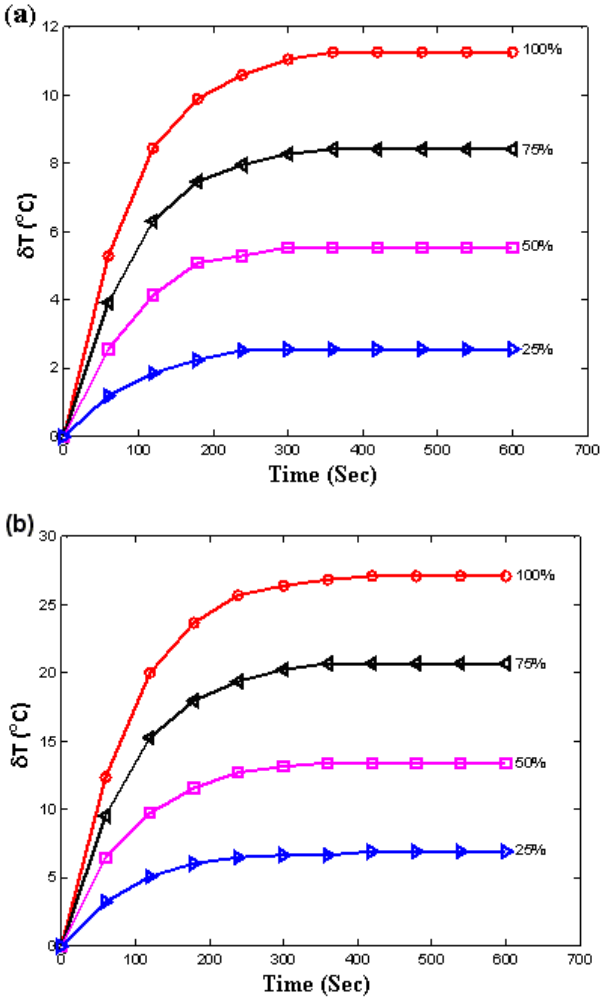

Figure 3.6. Variation of temperature increase with time under different duty cycles at two different frequencies (a) 100, and (b) 200 Hz [E = 1.4 kV/mm].

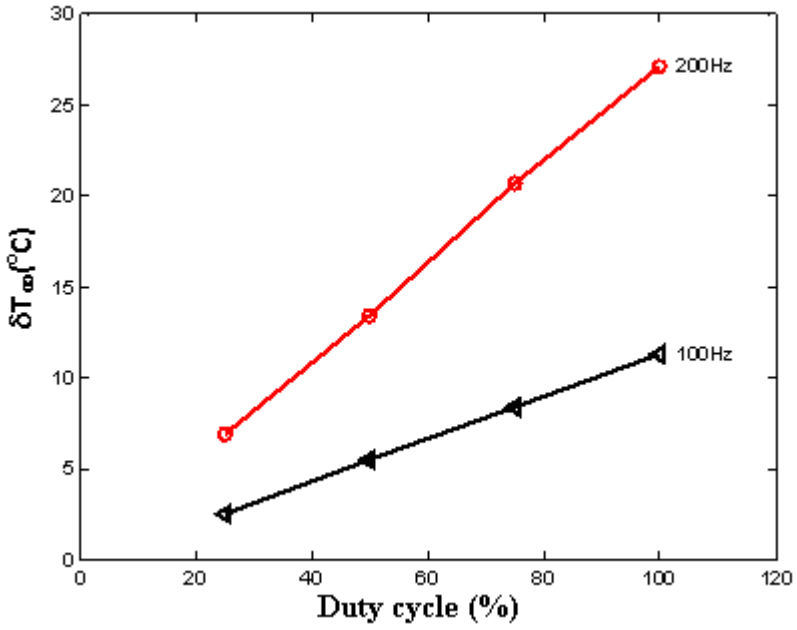

Figure 3.7. Dependence of steady state temperature increase on duty cycle percentage at two different frequencies and $E = 1.4$ kV/mm.

3.4. Self-Heat Generation Model

In this section of the chapter, a 1D analytical self-heating model based on the first law of thermodynamics is developed. The model accounts for the effect of different parameters including geometry, driving electric field, frequency, and duty cycle percentage on self heating, based on their effect on displacement hysteresis. Figure 3.8 shows a piezoelectric actuator placed horizontally on a bracket. The bracket is made of pure aluminum and works as a heat sink to reduce the amount of temperature increase within the actuator by increasing the amount of heat dissipated.

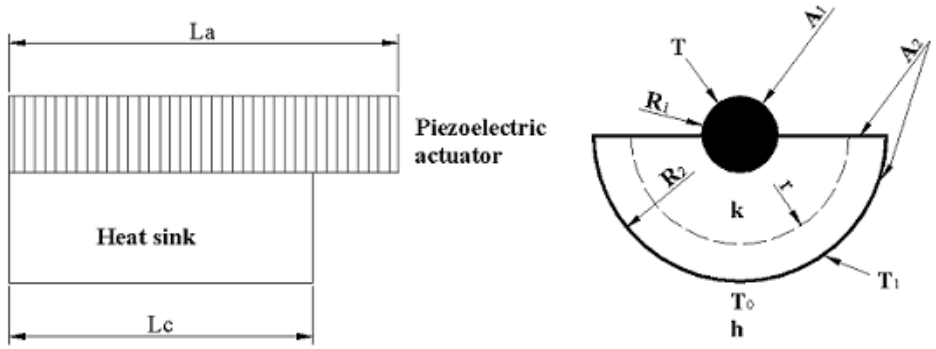

Figure 3.8. Sketch of an actuator with a heat sink (bracket).

According to the first law of thermodynamics, the law of energy conservation of a closed system may be expressed as:

$$\begin{pmatrix}\text{Rate of internal}\\ \text{heat generation}\end{pmatrix} - \begin{pmatrix}\text{Rate of energy transfer}\\ \text{to the environment}\end{pmatrix} = \begin{pmatrix}\text{Rate of energy accumulation}\\ \text{within the control volume}\end{pmatrix}$$

For a piezoelectric sample, and assuming uniform temperature distribution and isotropic material, the energy conservation law or the time rate of the actuator temperature change can be expressed as

$$\dot{Q}_g - \dot{Q}_d = m C_p \frac{dT}{dt} \tag{3.1}$$

where $\dot{Q}_g$ and $\dot{Q}_d$ are the rates of internal heat generation and of heat dissipation from the actuator in (J/s), respectively; m is the mass of the actuator in (kg); and C_p is the specific heat capacity of the actuator in (J/kg^{o}C).

As previously stated, self heating is mainly considered to be caused by losses. As a result, in a piezoelectric sample, $\dot{Q}_g$ can be expressed as follows:

$$\dot{Q}_g = D_f E_{ch} f \tag{3.2}$$

where D_f is the loss of the sample per electric charge per driving cycle in (J/C); E_{ch} is the accumulated electric charge on the sample in (C); and f is the driving-field frequency in (Hz).

In a typical multilayer piezoelectric-stack actuator, disks are mechanically connected in series and electrically connected in parallel. The electric charge in a PZT actuator can therefore be written as [27]

$$E_{ch} = \sum_{1}^{n} CV = n \frac{\kappa_{33} \kappa_0 A}{t_h} V = n \kappa_{33} \kappa_0 A E \tag{3.3}$$

where $C = \frac{\kappa_{33} \kappa_0 A}{t_h}$ is the capacitance of one disk in (Farads); t_h is the thickness of a single layer; A is the actuator cross-section area; $E=V/t_h$ is the electric-field magnitude in (Volts/m); n is the number of layers; κ_0 is the free space permittivity (8.85×10^{-12} F/m); and κ_{33} is the dielectric constant in the poling direction.

The dependence of κ_{33} of PZT ceramics on the intensity of applied electric-field has been experimentally studied by Zhang et al. [28]. They reported that κ_{33} is nearly constant at low levels of electric-field, while it linearly increases at higher levels of electric-field magnitude. Accordingly, it can be expected that the capacitance of PZT ceramics is electric-field dependent at higher magnitudes. However, in the current model κ_{33} is considered constant since the applied electric-field is not as high as compared to the values reported in [28]. In addition, the non-linear behavior is lumped into D_f which is considered temperature and electric-field dependent.

By substituting Equation (3.3) into Equation (3.2), the rate of heat generation per driving cycle can be expressed as follows:

$$\dot{Q}_g = D_f \left(n \kappa_{33} \kappa_0 A E \right) f \tag{3.4}$$

The experimental results presented in the previous section showed a linear dependence of steady state temperature increase on duty cycle in piezoelectric actuators. Therefore, Equation (3.4) may be modified to account for duty cycle effect such that

$$\dot{Q}_g = d_t D_f n \kappa_{33} \kappa_0 A E f \tag{3.5}$$

where d_t is the duty cycle percentage ($0 < d_t \leq 1.0$).

The experimental setup used in this study allowed a conduction heat transfer to the bracket through the bottom surface of the actuator and a convection heat transfer to the ambient through the top surface of the actuator and the bottom surface of the bracket, as shown in Figure 3.8. The two ends of the actuator were of non-conductive material, and

therefore, did not contribute to the energy released. Additionally, the lead wires attached to the actuators had small diameters and energy dissipated through them could be neglected. Thus, the rate of heat dissipated can be written such that

$$\dot{Q}_d = hA_1(T - T_0) + hA_2(T_1 - T_0) \tag{3.6}$$

where h is the convective heat coefficient of the surrounding air in (W / m^2 ^{o}C); T is the surface temperature of the actuator; T_1 is the bottom surface temperature of the bracket; and T_0 is the surrounding reference temperature. A_1 represents the actuator's surface area not in contact with the bracket; A_2 is the bracket's surface area not in contact with the actuator. The first term in Equation (3.6) represents the heat transfer from the actuator and the second term represents the heat transfer from the bracket. The areas A_1 and A_2 are expressed as follows:

$$\begin{aligned} A_1 &= \pi R_1 L_c + 2\pi R_1 (L_a - L_c), \\ A_2 &= ((\pi + 2)R_2 - 2R_1)L_c \end{aligned} \tag{3.7}$$

where L_a is the actuator length; L_c is the contact length with the bracket; R_1 is the actuator radius; and R_2 is the bracket radius. λ_2 is defined as the ratio of the bracket radius to the actuator radius such that $\lambda_2 = R_2 / R_1$.

To deduce the general form of heat dissipated through the bracket, $\dot{Q_{br}}$, it is assumed that the amount of heat gained through conduction is equal to the amount of heat dissipated through convection in the bracket. It is also assumed that heat flows only in a radial direction. $\dot{Q_{br}}$ can then be expressed as

$$\dot{Q}_{br} = hA_2\left(T_1 - T_o\right) \tag{3.8.1}$$

$$\dot{Q}_{br} = -kA_r \frac{dT}{dr} = -k\pi r L_c \frac{dT}{dr} \tag{3.8.2}$$

where k is the thermal conductivity of the bracket in (W / m ^{o}C); and $A_r = \pi r L_c$ is the area for heat flow in the bracket (r is measured from the center of the actuator). The boundary conditions are

$$\begin{aligned} T &= T_1 \quad at \quad r = R_2 \\ T &= T \quad at \quad r = R_1 \end{aligned} \tag{3.9}$$

The solution of Equation (3.8.2) is obtained as follows:

$$\dot{Q}_{br} \int_{R_1}^{R_2} \frac{dr}{r} = -\pi k L_c \int_{T}^{T_1} dT \tag{3.10.1}$$

$$\dot{Q}_{br} = \pi k L_c \frac{\left(T - T_1\right)}{\ln\left(\lambda_2\right)} \tag{3.10.2}$$

Substituting into Equation (3.8)

$$hA_2\left(T_1 - T_o\right) = \pi k L_c \frac{\left(T - T_1\right)}{\ln\left(\lambda_2\right)} \tag{3.11}$$

Rearranging Equation (3.11), the surface temperature of the bracket, T_1, is obtained as follows:

$$T_1 = \frac{1}{hA_2 \ln(\lambda_2) + \pi k L_c}\left[\pi k L_c\, T + hA_2 \ln(\lambda_2) T_o\right] \tag{3.12}$$

Substituting Equation (3.12) into Equation (3.6), and simplifying, the rate of heat dissipation is

$$\dot{Q}_d = \bar{h} A_1 (T - T_o) \tag{3.13}$$

where $\bar{h}$ represents the overall heat convection coefficient, and is expressed as

$$\bar{h} = \frac{h^2 A_2 \ln(\lambda_2) + h\pi k L_c (1 + A_2 / A_1)}{hA_2 \ln(\lambda_2) + \pi k L_c} \tag{3.14}$$

In the case of no heat sink, (i.e., k = 0 and/or L_c = 0), the overall heat convection coefficient and the rate of heat dissipation are expressed as

$$\bar{h} = h \text{ , and } \dot{Q}_d = hA_1 (T - T_o) \tag{3.15}$$

where h is the convection heat transfer coefficient; and $A_1 = 2\pi R_1 L_a$.

Substituting $\dot{Q}_g$ and $\dot{Q}_d$ from Equation (3.5) and Equation (3.13), respectively, into Equation (3.1)

$$d_t D_f (n \kappa_{33} \kappa_0 A E) f - \bar{h} A_1 (T - T_0) = m C_p \frac{dT}{dt} \tag{3.16}$$

The experimental results presented in the previous section showed the dependency of displacement hysteresis D_f on electric field and temperature. Therefore, from Equation (3.16), it is expected that the amount of heat generated in an actuator is electric-field and

temperature dependent. At a specified electric-field magnitude, the solution of Equation (3.16) is obtained for two cases: (i) D_f is linearly dependent on temperature; and (ii) D_f is constant (does not change with temperature).

3.4.1. Case i : D_f is Dependent on Temperature

Displacement hysteresis is assumed to linearly increase with increased temperature. At a specified electric-field magnitude, D_f can be linearly fitted in the form

$$D_f = a_1 + a_2 T \tag{3.17}$$

where a_1 and a_2 are fitting constants determined from the experimental data shown in Figure 3.3(b).

Substituting Equation (3.17) into Equation (3.16) and letting $C_1 = d_t n \kappa_{33} \kappa_0 A E f$,

$$C_1(a_1 + a_2 T) - \bar{h} A_1 (T - T_0) = m C_p \frac{dT}{dt} \tag{3.18}$$

Rearranging Equation (3.18),

$$m C_p \frac{dT}{dt} + (\bar{h} A_1 - C_1 a_2) T = C_1 a_1 + \bar{h} A_1 T_0 \tag{3.19}$$

At steady state, the rate of temperature increase is zero (i.e., $dT/dt = 0$). The steady state temperature T_∞ is easily obtained from Equation (3.19), as follows:

$$T_\infty = \frac{C_1 a_1 + \bar{h} A_1 T_0}{\bar{h} A_1 - C_1 a_2} \tag{3.20}$$

The temperature increase at steady state is expressed as follows:

$$\delta T_{\infty} = T_{\infty} - T_o = \frac{C_1\left(a_1 + a_2 T_o\right)}{\bar{h}\, A_1 - C_1 a_2} \tag{3.21}$$

The solution of Equation (3.19) is obtained by solving for a homogeneous solution and a particular solution. The general homogenous solution is given as follows:

$$T = e^{-\int\left(\frac{\bar{h}\, A_1 - C_1 a_2}{m C_p}\right) dt} = e^{-\left(\frac{\bar{h}\, A_1 - C_1 a_2}{m C_p}\right) t} \tag{3.22}$$

Consequently, a particular solution is obtained as follows:

$$T = e^{-\frac{\bar{h}\, A_1 - C_1 a_2}{m C_p} t}\left(k_1 + \frac{C_1 a_1 + \bar{h}\, A_1 T_0}{\bar{h}\, A_1 - C_1 a_2}\; e^{\frac{\bar{h}\, A_1 - C_1 a_2}{m C_p} t}\right) \tag{3.23}$$

Applying the initial boundary condition (i.e, at time $t = 0,\ T = T_0$), the integration constant k_1 is

$$k_1 = -\frac{C_1\left(a_1 + a_2 T_0\right)}{\bar{h}\, A_1 - C_1 a_2} \tag{3.24}$$

The actuator temperature T is then written as

$$T = \left(\frac{C_1 a_1 + \bar{h}\, A_1 T_0}{\bar{h}\, A_1 - C_1 a_2} - \frac{C_1\left(a_1 + a_2 T_0\right)}{\bar{h}\, A_1 - C_1 a_2} e^{-\frac{\bar{h}\, A_1 - C_1 a_2}{m C_p} t}\right) \tag{3.25}$$

with temperature increase δT written in the form

$$\delta T = \delta T_{\infty}\left(1 - e^{-\frac{\bar{h}A_1 - C_1 a_2}{\beta m C_p} t}\right) \tag{3.26}$$

A chosen parameter β was introduced into Equation (3.26) such that analytical results are in best agreement with experimental results. The heat capacity of soft and hard PZT was measured by Yarlagadda et al. [29] over a wide range of temperature, and both were reported to be temperature dependent. It was also reported by [30] that the heat capacity of bulk PZT materials increases with increased temperature. Accordingly, in the current study, the parameter β may be interpreted as the dependency of the heat capacity coefficient on actuator temperature which is electric-field dependent. β does not affect the steady state temperature, and only changes the time constant of the exponential response. Equation (3.26) is simplified such that

$$\delta T = \delta T_{\infty}\left(1 - e^{-\frac{t}{\tau}}\right) \tag{3.27}$$

where $\delta T_{\infty} = \dfrac{C_1\left(a_1 + a_2 T_0\right)}{\bar{h}A_1 - C_1 a_2}$ is the steady state temperature increase, and $\tau = \dfrac{\beta m C_p}{\bar{h}A_1 - C_1 a_2}$ is a time constant.

3.4.2. Case ii: D_f is Constant

By assuming that displacement hysteresis is temperature independent (i.e., constant for a specified electric-field magnitude), the solution of Equation (3.16) is obtained, similar to Case *i*, such that

$$\delta T = \delta T_{\infty}\left(1 - e^{-\frac{t}{\tau}}\right) \tag{3.28}$$

where $\delta T_{\infty} = \dfrac{d_t n \kappa_{33} \kappa_0 A E D_f f}{\bar{h} A_1}$ is the actuator steady state temperature (i.e., maximum temperature rise), and $\tau = \dfrac{\beta m C_p}{\bar{h} A_1}$ is a time constant.

In this case, displacement hysteresis was assumed to be temperature independent. However, when Equation (3.28) was applied to obtain the actuator surface temperature, an incremental solution was used and displacement hysteresis was updated after each increment according to the linear fitting presented in Figure 3.3(b). In other words, an initial surrounding reference temperature T_0 is assumed; D_f and T are obtained based on that temperature using Equation (3.17); the newly computed temperature T is used to generate a new D_f; and then a new T is solved for using Equation (3.28). For the sake of easy presentation, we will call this procedure "Case *ii.b*", and the temperature independent case "Case *ii.a*".

3.5. Results and Discussion

3.5.1. No Heat Sink (k = 0 and/or L_c = 0)

Figure 3.9 shows temperature increase δT under sinusoidal electric fields of 0.6, 1.0, and 1.4 kV/mm, at different frequencies of up to 300 Hz, and with a duty cycle of 100 %; no heat sink was used. It can be seen from Figure 3.9 that the three different solution cases (Case *i*, where D_f is linearly dependent on temperature, Case *ii.a*, where D_f is constant, and Case *ii.b*, where D_f is incrementally updated) were in good agreement with the experimental results at low frequencies ($\leq$ 100 *Hz*). A possible explanation for all cases giving similar results could be the low level of temperature increase, so that the dependence of displacement hysteresis on temperature could be neglected (i.e., D_f is constant).

As frequency and electric field increased, δT increased and displacement-hysteresis dependence on temperature became more significant. At higher levels of electric-field magnitudes and driving frequencies, Case *ii.a***,** where D_f was assumed constant, deviated considerably from actual experimental results. The steady state temperature increase at E = 1.4 kV/mm and f = 300 Hz, predicted from Case *ii.a***,** was almost 41 % less than the measured steady state temperature increase Figure 3.9(c). On the other hand, for all levels of electric field magnitudes and frequencies, Case *i* and Case *ii.b* showed almost identical steady state temperature increases with a reasonable agreement with experimental results (within ±5 %).

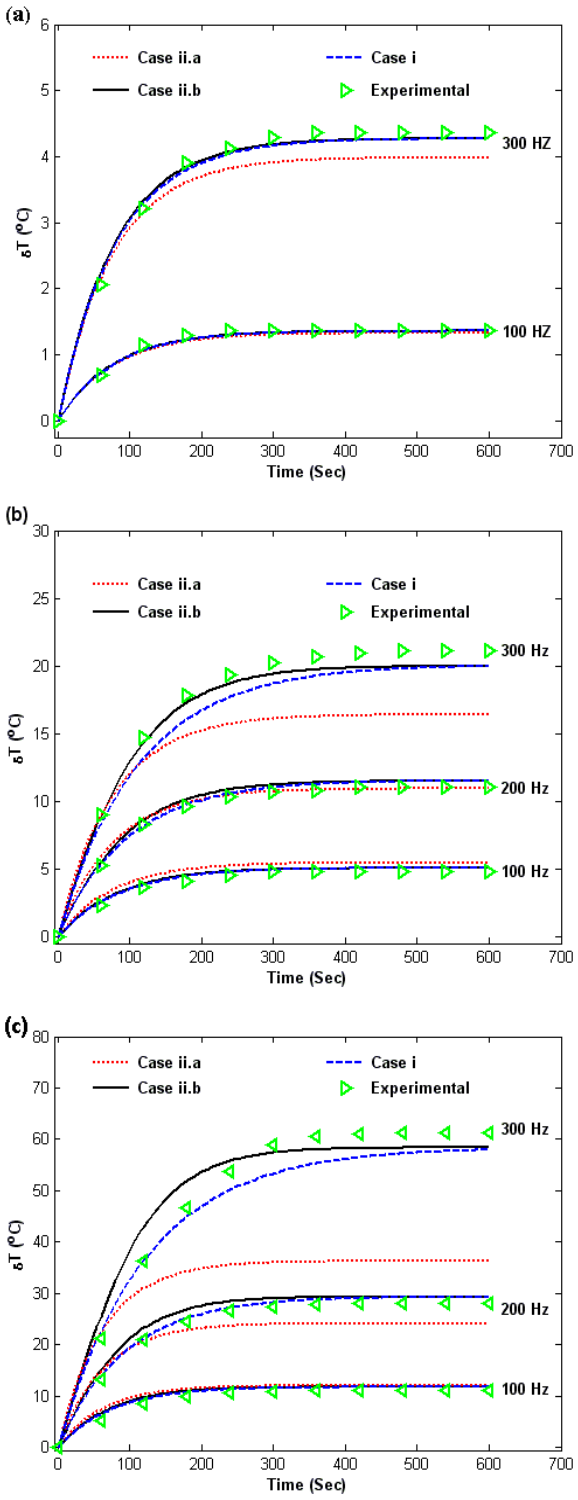

Figure 3.9. Temperature increase with time under continuous sinusoidal electric fields and different frequencies (a) 0.6, (b) 1.0, and (c) 1.4 kV/mm.

The fitting parameter β introduced in Equation (3.26) is indirectly dependent on electric field. As previously mentioned, β may be interpreted as the dependency of the heat capacity coefficient C_p on actuator temperature, which is dependent on electric-field magnitude. The parameter β increased with increased electric-field magnitude; that is, specific heat capacity, C_p, increased with increased electric-field magnitude (i.e., the heating energy required to increase the temperature of the actuator increased). Similarly, it can be seen that the convection heat coefficient, h, is also indirectly dependent on electric field strength; it increased with increased electric field strength as a result of temperature increase in the actuator. An empirical value of h at $E = 0$ and $f = 0$ was predicted using the empirical equations provided by [31] for the case of a horizontal cylinder. Figure 3.10 shows the estimated values of h at different levels of electric-field magnitudes. It should be noted that although β and h indirectly increased with electric-field magnitude, the ratio β/h was found to be constant with electric-field magnitude.

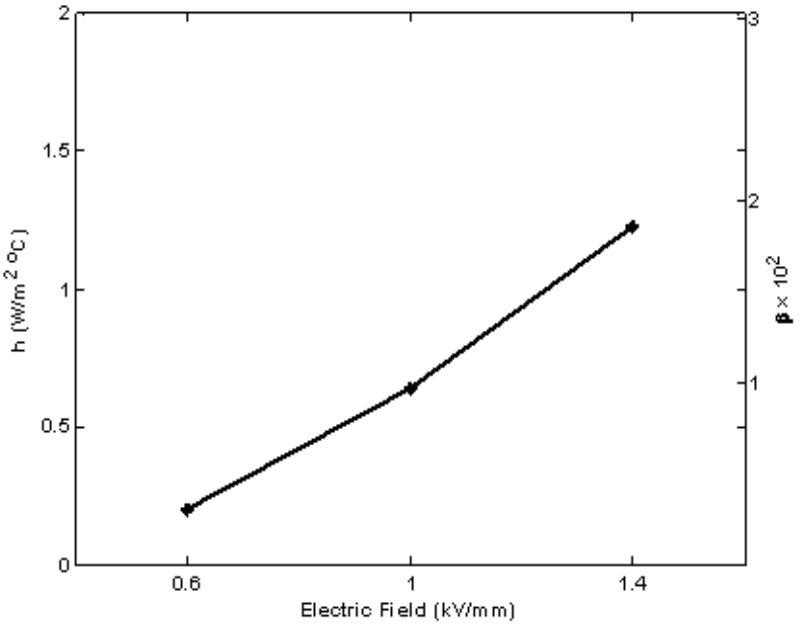

Figure 3.10. Variation of heat convection coefficient h, and β with electric-field magnitude.

The effect of duty cycle on temperature increase can also be predicted using the developed self-heating model. Duty cycle significantly affected self-heat generation under dynamic operating conditions. Figure 3.11 shows the temperature increase that occurred under a unipolar sinusoidal electric field E = 1.4 kV/mm at (a) f = 100 Hz, and (b) f = 200 Hz, respectively. It can be seen that reducing duty cycle can dramatically decrease the amount of heat generated in piezoelectric actuators. This phenomenon allows application of higher electric fields and frequencies with low duty cycles, since the latter reduce heat generation. The developed heat generation mechanism simulates the experimental results fairly closely at different duty cycles up to 100 %. Case *ii.a* gives accurate results at low frequency levels and duty cycles; however, it deviates as frequency and/or duty cycle increases.

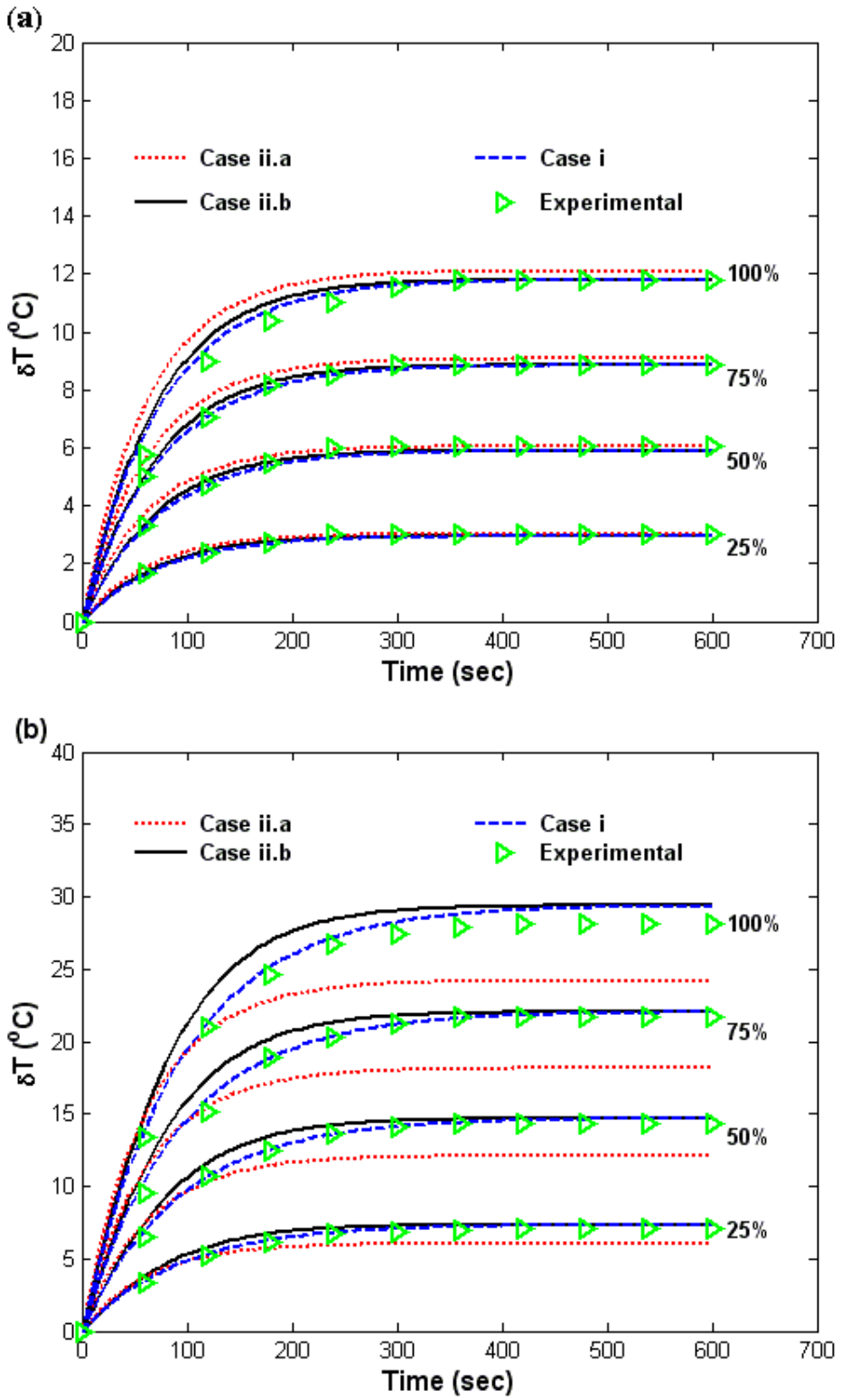

Figure 3.11. Variation of temperature increase with time for different duty cycles at E = 1.4 kV/mm under two different frequencies (a) 100, and (b) 200 Hz.

3.5.2. Using a Heat Sink

Using a heat sink of high thermal conductivity may also help reduce the temperature increase in piezoelectric actuators, by increasing the amount of heat dissipated. The experimental setup used in this study allowed attaching a pure aluminum bracket of thermal conductivity k = 204 W/m^{o}C. The bracket functioned as a heat sink. Practically, such a bracket should move with the actuator, to avoid abrading the outer surface of the actuator. It can be seen from Figure 3.12 that Case *i* and Case *ii.b* are again more accurate than Case *ii.a* at higher frequencies. At E = 1.4 kV/mm and f = 300 Hz, using an aluminum bracket as a heat sink reduced the amount of temperature increase within the actuator by almost 39 % (the steady state temperature δT_{∞} with no heat sink was 60.5 ^{o}C), while it was reduced to 37 ^{o}C when a heat sink was used, as shown in Figure 3.13.

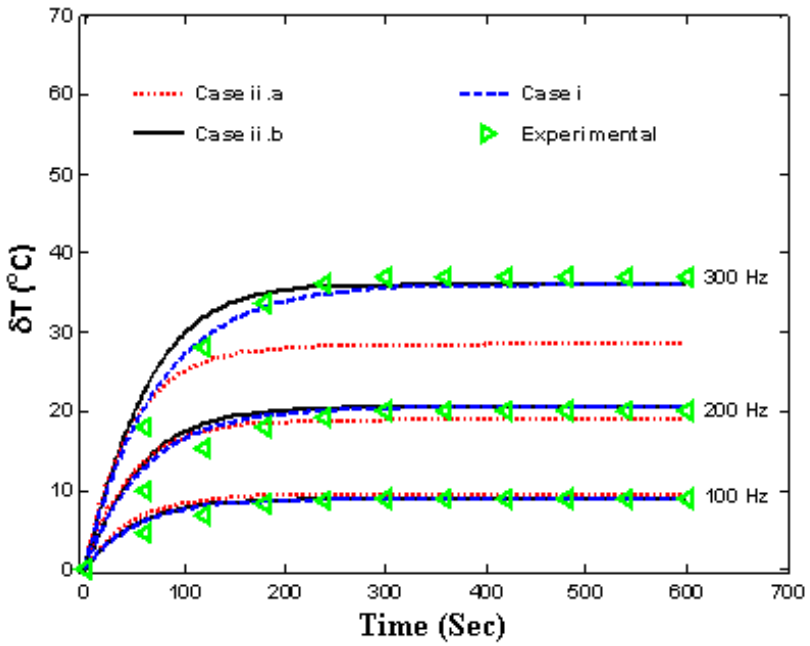

Figure 3.12. Variation of temperature increase with time for different frequencies at E = 1.4 kV/mm (using heat sink).

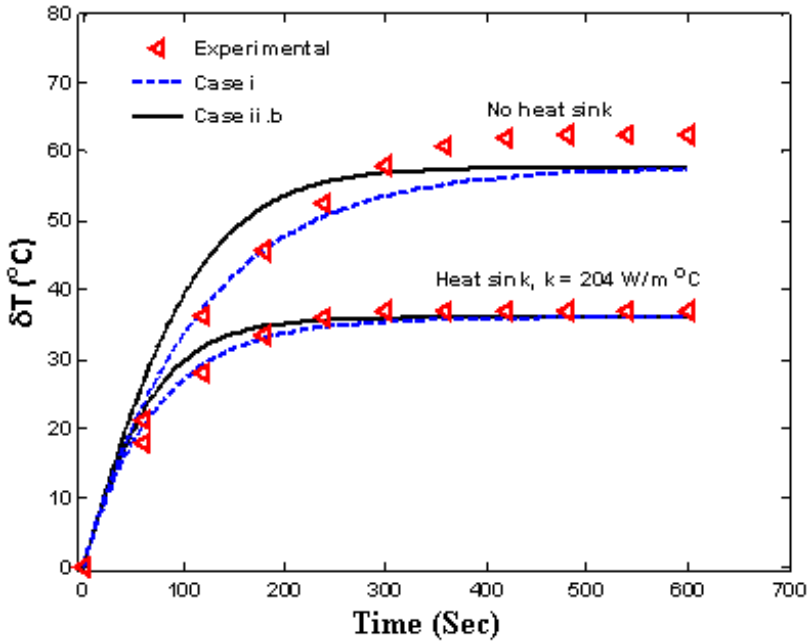

Figure 3.13. Effect of using a heat sink on temperature increase

(E = 1.4 kV/mm, f = 300 Hz, and 100 % duty cycle).

3.6. Conclusions

In this chapter, self heating in soft Lead Zirconate Titanate (PZT) stack actuators was studied at different dynamic operating conditions relevant to the fuel injection process. Heat generated in these actuators was dependent on applied electric-field magnitude and frequency. Decreasing the duty cycle significantly decreased heat generated in the actuators. A mathematical model based on the first law of thermodynamics and accounting for different controlling parameters was developed. The model represents a closed-form solution for temperature increase that shows the classical exponential variation with respect to time, in the form $\delta T = \delta T_{\infty} (1-e^{-t/\tau})$. The developed model provides an invaluable tool for designing piezoelectric actuators for fuel injectors, as well as for high-power actuators, with limited self heating.

3.7. Bibliography

[1] Ardelean EV, Cole DG, Clark RL. High performance "V-stack" piezoelectric actuator. *Journal of Intelligent Material Systems and Structures* 2004;15:879.

[2] Chen Q, Yao DJ, Kim CJ, Carman GP. Frequency response of an inchworm motor fabricated with micromachined interlocking surface mesoscale actuator device (MAD). *Proceedings of SPIE* 1998;3329:768.

[3] Jäker P. Electro-Mechanical Characterization of High-Performance Piezoactuators. *Proceedings of SPIE* 1997;3039:670.

[4] Irschik H. A review on static and dynamic shape control of structures by piezoelectric actuation. *Journal of Engineering Structures* 2002;24:5.

[5] Akella P, Chen X, Cheng W, Hughes D, Wen JT. Modeling and control of smart structures with bonded piezoelectric sensors and actuators. *Journal of Smart Materials and Structures* 1994;3:344.

[6] Ashida F, Tauchert TR. Temperature determination for a contacting body based on an inverse piezothermoelastic problem. *International Journal of Solids and Structures* 1997;34:2549.

[7] Uchino K. Piezoelectric actuators: Expansion from IT/robotics to ecological/energy applications. *Journal of Electroceramics* 2008;20:301.

[8] Fujii A, Toyao T. Piezoelectric actuators with high reliability for diesel injection valve. *10th International Conference on New Actuators,* 2006:177.

[9] Schuh C, Steinkopff T, Wolff A, Lubitz K. Piezoceramic multilayer actuators for fuel injection systems in automotive area. *Proceedings of SPIE* 2003;3992:165.

[10] Senousy MS, Li F, Mumford D, Gadala MS, Rajapakse RKND. Thermo-electro-mechanical performance of piezoelectric stack actuators for fuel injector applications. *Journal of Intelligent Material Systems and Structures* 2009;20:387.

[11] Chaplya PM, Mitrovic M, Carman GP, Straub FK. Durability properties of piezoelectric stack actuators under combined electromechanical loading. *Journal of Applied Physics* 2006;100:124111.

[12] Andersen B, Ringgaard E, Bove T, Albareda A, Pérez R. Performance of piezoelectric ceramic multilayer components based on hard and soft PZT. *7th International Conference on New Actuators* 2000:419.

[13] Heinzmann A, Hennig E, Kolle B, Kopsch D, Richter S, Schwotzer H, Wehrsdorfer E. Properties of PZT Multilayer Actuators. *8th International Conference on New Actuators* 2002.

[14] Li FX, Rajapakse RKND, Mumford D, Gadala M. Quasi-static thermo-electro-mechanical behaviour of piezoelectric stack actuators. *Smart Materials and Structures* 2008;17:015049.

[15] Sakai T, Ishikiriyama M, Shimazaki R. Durability of Piezoelectric Ceramics for an Actuator. *Japanese Journal of Applied Physics* 1992;31:3051.

[16] Sakai T, Kawamoto H. Durability properties of piezoelectric stack actuator. *Japanese Journal of Applied Physics* 1998;37:5338.

[17] Pritchard J, Ramesh R, Bowen CR. Time-temperature profiles of multi-layer actuators. *Sensors and Actuators, A: Physical* 2004;115:140.

[18] Ronkanen P, Kallio P, Vilkko M, Koivo HN. Self heating of piezoelectric actuators: Measurement and compensation. *Int. Symp. on Micro-NanoMechatronics and Human Sci.,* 2004:313.

[19] Weiland LM, Lynch CS. Thermo-Electro-Mechanical Behavior of Ferroelectric Materials Part II: Introduction of Rate and Self-Heating Effects. *Structures Journal of Intelligent Material Systems and Structures* 2003;14:605.

[20] Yao K, Uchino K, Xu Y, Dong S, Lim LC. Compact piezoelectric stacked actuators for high power applications. *IEEE Transactions on Ultrasonics, Ferroelectrics, and Frequency Control* 2000;47:819.

[21] Zheng J, Takahashi S, Yoshikawa S, Uchino K, de Vries JWC. Heat generation in multilayer piezoelectric actuators. *Journal of the American Ceramic Society* 1996;79:3193.

[22] Lesieutre GA, Fang L, Koopmann GH, Pai SP, Yoshikawa S. Heat generation of a piezoceramic induced-strain actuator embedded in a glass/epoxy composite panel. 1996;2717:267.

[23] Ochi A, Takahashi S, Tagami S. Temperature Characteristics for Multilayer Piezoelectric Ceramic Actuator. *Japanese Journal of Applied Physics* 1985;24:209.

[24] Uchino K, Hirose S. Loss mechanisms in piezoelectrics: How to measure different losses separately. *IEEE Transactions on Ultrasonics, Ferroelectrics, and Frequency Control* 2001;48:307.

[25] Evans J. Introduction to Small Signal Displacement Measurements using Precision Testers. *Radiant Technologies, Inc*, 2005.

[26] Lu X, Hanagud SV. Extended irreversible thermodynamics modeling for self-heating and dissipation in piezoelectric ceramics. *IEEE Transactions on Ultrasonics, Ferroelectrics, and Frequency Control* 2004;51:1582.

[27] Buchanan RC. Ceramic materials for electronics: processing, properties, and applications. *Marcel Dekker Inc.* New York 1991.

[28] Zhang QM, Wang H, Zhao J. Effect of Driving Field and Temperature on the Response Behavior of Ferroelectric Actuator and Sensor Materials. *Journal of Intelligent Material Systems and Structures* 1995;6:84.

[29] Yarlagadda S, Chan MHW, Lee H, Lesieutre GA, Jensen DW, Messer RS. Low temperature thermal conductivity, heat capacity, and heat generation of PZT. *Journal of Intelligent Material Systems and Structures* 1995;6:757.

[30] Morimoto K, Uematsu A, Sawai S, Hisano K, Yamamoto T. Simultaneous Measurement of Thermophysical Properties and Dielectric Properties of PZT-Based Ferroelectric Ceramics by Thermal Radiation Calorimetry. *International Journal of Thermophysics* 2003;24:821.

[31] Incropera FP, Dewitt DP, Bergman TL, Lavine AS. Introduction to Heat Transfer. *John Wiley & Sons*. USA 2007.

Chapter 4

4. Temperature-Dependent Two-Step Domain-Switching Model*

4.1. Introduction

Multilayer piezoelectric stack actuators are used in diverse engineering applications. Their low driving voltage and power consumption make them excellent candidates for use in fuel injection systems [1]. Because of operational requirements in fuel injection, stack actuators are subjected to relatively high electric-field magnitudes (> 1.5 MV/m), high frequencies (> 100 Hz), and elevated temperatures (up to 120 ^{o}C). Performance of selected Lead Zirconate Titanate (PZT) actuators under conditions relevant to fuel injection systems has been experimentally studied by Senousy et al. [2, 3] and Li et al. [4]. The results showed that PZT stacks typically generate heat and exhibit nonlinear behavior. The generated heat may produce thermal stresses, which could lead to structural failure of the stacks. Self heating and the nonlinearity response of PZT stacks are interconnected; nonlinearity is believed to be the main cause of self heating [5].

* "A version of this chapter has been published. **Senousy, M. S.,** Rajapakse, R.K.N.D., and Gadala, M.S. (2009) A Temperature-Dependent Two-Step Domain-Switching Model for Ferroelectric Materials, *Acta Materialia*, doi:10.1016/j.actamat.2009.08.039."

Moreover, it has been widely accepted that domain switching is the main source of nonlinearity [6].

Domains are regions of material with the same spontaneous polarization direction, and are formed to minimize free energy when piezoelectric materials undergo paraelectric to ferroelectric phase transformation at the Curie temperature. Domain switching involves rotation of the polarization direction of a domain by either 180^o or non-180^o in response to a sufficiently large electric field (ferroelectric) or mechanical stress (ferroelastic). In tetragonal piezoelectric ceramics such as PZT ceramics, an electric field can rotate the polarization by either 180^o or 90^o, whereas a mechanical stress can only cause 90^o rotation. 180^o domain switching does not cause any change in strain. However, 90^o domain switching causes an increase in strain in the new polarization direction and a reduction by the same amount in the initial direction.

In order to better understand the overall performance of PZT actuators used in fuel injection, both domain switching and temperature effects need to be considered. The development of accurate domain-switching models for piezoelectric materials remains a challenging task [7, 8]. Hwang et al. [9] developed the first domain-switching model, and their model has served as the foundation for several other models [10, 11]. Hwang's model was based on the reduction in potential energy caused by the changes in spontaneous strain and spontaneous polarization. It has also served as a base for several nonlinear finite element modeling studies of ferroelectric materials [12, 13]. Jiang [14] extended the above model to also include the dependence of potential energy reduction on variations in the produced strain. These models neglected the influence of electromechanical coupling, material anisotropy, and temperature effects on domain

switching and assumed that the energy required to cause 180^o or 90^o switching is identical. Based on the concepts of Hwang et al. [9], Zeng and Rajapakse [15] developed a domain-switching model that accounted for electromechanical coupling and the changes in electro-elastic properties of switched domains. Their model also assumed that both 180^o and 90^o domain switching occur at the same energy level. Different energy levels for 180^o and 90^o domain switching were assumed in other models [16-19].

In this paper, a new domain-switching model accounting for electromechanical coupling, temperature and different energy barriers for 180^o and 90^o switching is presented for tetragonal materials by extending the concepts of Hwang et al. [9]. It is assumed that 180^o switching is a result of two 90^o switching occurrences. A similar sequential switching process was reported previously for rhombohedral materials by several authors [20-22]. This assumption implies that some domains may not complete 180^o rotation, so that an improved prediction of the hysteretic nonlinear behavior can be expected. The governing equations of a piezothermoelastic continuum are summarized in Section 4.2. The development of the switching model is presented in Section 4.3. A finite element scheme based on the proposed switching model is presented in Section 4.4. A comparison of the present model with the Hwang et al.'s model [9] and with experimental results, as well as a discussion on domain-switching evolution, is provided in Section 4.5.

4.2. Governing Equations

The constitutive relations describing the behavior of a piezothermoelastic continuum can be expressed as follows [23]:

$$\varepsilon_{ij} = s_{ijkl}^{(E,T)}\sigma_{kl} + d_{ijk}E_k + \alpha_{ij}T + \varepsilon_{ij}^r \tag{4.1.a}$$

$$D_i = d_{ijk}\sigma_{jk} + \kappa_{ij}^{(\sigma,T)}E_j + p_iT + P_i^r \tag{4.1.b}$$

$$I = \alpha_{ij}\sigma_{ij} + p_iE_i + \alpha_v^{(\sigma,E)}T \tag{4.1.c}$$

Alternatively, they can be written as

$$\sigma_{ij} = c_{ijkl}^{(E,T)}\left(\varepsilon_{kl} - \varepsilon_{kl}^r\right) - e_{ijk}E_k - \lambda_{ij}T \tag{4.2.a}$$

$$D_i = e_{ijk}\left(\varepsilon_{jk} - \varepsilon_{jk}^r\right) + \kappa_{ij}^{(\varepsilon,T)}E_j + p_iT + P_i^r \tag{4.2.b}$$

$$I = \lambda_{ij}\left(\varepsilon_{ij} - \varepsilon_{ij}^r\right) + p_iE_i + \alpha_v^{(\varepsilon,E)}T \tag{4.2.c}$$

where ε_{ij}^r is the remnant strain tensor; P_i^r is the remnant polarization vector; $c_{ijkl}^{(E,T)}$ and $s_{ijkl}^{(E,T)}$ are the elastic constants and elastic compliance, respectively, measured at constant electric field and constant temperature; e_{ijk} and d_{ijk} are the piezoelectric-stress and piezoelectric-strain constants, respectively; $\kappa_{ij}^{(\varepsilon,T)}$ are the dielectric coefficients measured under constant strain and constant temperature, and $\kappa_{ij}^{(\sigma,T)}$ are the dielectric coefficients measured under constant stress and constant temperature; λ_{ij} and α_{ij} are the thermal-stress and thermal-strain coefficients, respectively; p_i are the pyroelectric constants;

$\alpha_v^{(\varepsilon,E)}$ is a material constant $\left(\alpha_v^{(\varepsilon,E)} = \rho c_v^{(\varepsilon,E)} T_r^{-1}\right)$, where ρ is the mass density; and $c_v^{(\varepsilon,E)}$ is the specific heat at a constant volume and a constant electric field.

The above material properties are related such that

$$\kappa_{ij}^{(\sigma,T)} = \kappa_{ij}^{(\varepsilon,T)} / \left(1-\chi^2\right),\ s_{ijkl}^{(E,T)} = \left(c_{ijkl}^{(E,T)}\right)^{-1},\ \alpha_{ij} = c_{ijkl}^{(E,T)} \lambda_{kl}, \text{ and } d_{ijk} = e_{imn}\left(c_{mnjk}^{(E,T)}\right)^{-1} \tag{4.3}$$

where χ^2 is the electromecahanical coupling factor, which can be defined as the ratio of stored electrical/mechanical energy to supplied mechanical/electrical energy.

The mechanical strain ε_{ij}, electric field E_i, and heat flux q_i can be related to the derivatives of the mechanical displacement vector u_i, electric potential φ, and temperature T. The equilibrium equations for a continuum can be expressed as

$$\sigma_{ij,j} = 0, \quad D_{i,i} = 0, \quad q_{i,i} - \dot{I} T_r = 0 \tag{4.4}$$

where σ_{ij} is the stress tensor; D_i is the electric displacement vector; T_r is a reference temperature; and I is the entropy density.

The relevant boundary conditions are

$$u_i = u_i^0 \ \text{ on } s_u, \quad \text{or} \quad \sigma_{ij} n_j = t_i \quad \text{on} s_t \tag{4.5.a}$$

$$\varphi = \varphi^0 \ \text{ on} s_\varphi, \quad \text{or} \quad D_i n_i = -Q \ \text{ on} s_Q \tag{4.5.b}$$

$$T = T^0 \ \text{ on} s_T, \quad \text{or} \quad -K_{ij} T_{,j} n_i = q_s + h_v\left(T_f - T\right) \ \text{ on} s_q \tag{4.5.c}$$

where u_i^0, t_i, φ^0, Q and n_i are the specified mechanical displacement, surface traction, electric potential, electric-surface charge, and the outward unit normal vector components, respectively; T^0 is a prescribed temperature; q_s is the rate of heat flow per unit area; T_f is the surrounding temperature; K_{ij} are the heat conduction coefficients; and h_v is the convection heat transfer coefficient. s_u and s_t are the surfaces where mechanical displacements and tractions, respectively, are specified; s_φ and s_Q are the surfaces where electric potential and electric charges, respectively, are specified; s_T is the surface with specified temperature; and s_q is the surface with prescribed heat flow.

4.3. Domain-Switching Criterion

Following [9, 11], it is assumed that if a domain within a piezothermoelastic continuum of a total volume v switches, the total potential energy Π is reduced. The change in potential energy $\Delta\Pi$ can be expressed as

$$\Delta\prod = \int_v \Delta F\, dv - \int_{s_t} t_i \Delta u_i^0\, ds_t - \int_{s_Q} \varphi^0 \Delta Q\, ds_Q - \int_{s_T} T^0 \Delta q_s\, ds_T \tag{4.6}$$

where F is the free-energy density (energy per unit volume), which is a function of electric field, mechanical stress, and temperature.

Following Ikeda [23] and Landis [24-26], F can be expressed as

$$F = \frac{E_i \kappa_{ij}^{(\sigma,T)} E_j}{2} + \frac{\sigma_{ij} s_{ijkl}^{(E,T)} \sigma_{kl}}{2} + \frac{T\alpha_v^{(\sigma,E)} T}{2} + E_i d_{ijk} \sigma_{jk} + \sigma_{ij}\alpha_{ij} T + E_i p_i T \tag{4.7}$$

where the last three terms in Equation (4.7) represent the piezoelectric, thermoelastic, and pyroelectric coupling terms, respectively.

Rearranging the terms in Equation (4.7) and substituting the constitutive relations (4.1), F can be written as

$$F = \frac{E_i\left(D_i - P_i^r\right)}{2} + \frac{\sigma_{ij}\left(\varepsilon_{ij} - \varepsilon_{ij}^r\right)}{2} + \frac{TI}{2} \tag{4.8}$$

The reduction in potential energy $\Delta\Pi$ due to domain switching is accompanied by a change in the local material states of $P_i^r, \varepsilon_{ij}^r$, s_{ijkl}, d_{ijk}, κ_{ij}, α_{ij}, α_v and p_i in the switching volume. In this paper, the state before switching is called "*State 1*", whereas the state after switching is called "*State 2*". The change in free energy ΔF due to domain switching can be expressed as

$$\begin{aligned}\int_v \Delta F\, dv &= \int_v \left(F^{(2)} - F^{(1)}\right) dv \\ &= \frac{1}{2}\int_v \begin{bmatrix} \left(E_i^{(2)} + E_i^{(1)}\right)\Delta D_i - \left(E_i^{(2)} + E_i^{(1)}\right)\Delta P_i^r + E_i^{(2)}\left(D_i^{(1)} - P_i^{(r1)}\right) \\ - E_i^{(1)}\left(D_i^{(2)} - P_i^{(r2)}\right) + \left(\sigma_{ij}^{(2)} + \sigma_{ij}^{(1)}\right)\Delta\varepsilon_{ij} - \left(\sigma_{ij}^{(2)} + \sigma_{ij}^{(1)}\right)\Delta\varepsilon_{ij}^r \\ + \sigma_{ij}^{(2)}\left(\varepsilon_{ij}^{(1)} - \varepsilon_{ij}^{(r1)}\right) - \sigma_{ij}^{(1)}\left(\varepsilon_{ij}^{(2)} - \varepsilon_{ij}^{(r2)}\right) + \left(T^{(2)} + T^{(1)}\right)\Delta I \\ + T^{(2)} I^{(1)} - T^{(1)} I^{(2)} \end{bmatrix} dv \end{aligned} \tag{4.9}$$

where superscripts $^{(1)}$ and $^{(2)}$ are used to denote the quantities associated with States *1* and *2*, respectively.

Applying the divergence theorem, the first, fifth, and ninth volume integrals in Equation (4.9) can be reduced to

$$\int_v \frac{\left(E_i^{(2)} + E_i^{(1)}\right)}{2} \Delta D_i \, dv = -\frac{1}{2} \int_{s_Q} \left(\varphi^{(2)} + \varphi^{(1)}\right) n_i \Delta D_i \, ds_Q = \int_{s_Q} \varphi^0 \Delta Q \, ds_Q \tag{4.10.a}$$

$$\int_v \frac{\left(\sigma_{ij}^{(2)} + \sigma_{ij}^{(1)}\right)}{2} \Delta \varepsilon_{ij} \, dV = \int_{s_t} \sigma_{ij} n_j \Delta u_i^0 \, ds_t = \int_{s_t} t_i \Delta u_i^0 \, ds_t \tag{4.10.b}$$

$$\int_v \frac{\left(T^{(2)} + T^{(1)}\right)}{2} \Delta I \, dv = -\int_v T^0 K_{ij} T_{,j} n_i \, dv = \int_{s_q} T^0 q_s \, ds_q \tag{4.10.c}$$

Substituting Equation (4.1), (4.9), and (4.10) into Equation (4.6), the change in potential energy density $\Delta \Pi'$ due to domain switching (change in potential energy per unit volume) can be written as

$$\begin{aligned} \Delta \prod{}' = & -\frac{\left(E_i^{(2)} + E_i^{(1)}\right)}{2} \Delta P_i^r - \frac{\left(\sigma_{ij}^{(2)} + \sigma_{ij}^{(1)}\right)}{2} \Delta \varepsilon_{ij}^r \\ & - \frac{E_i^{(2)} \Delta \kappa_{ij}^{(\sigma,\theta)} E_j^{(1)}}{2} - \frac{\sigma_{ij}^{(2)} \Delta s_{ijkl}^{(E,\theta)} \sigma_{kl}^{(1)}}{2} - \frac{T^{(2)} \Delta \alpha_v^{(\sigma,E)} T^{(1)}}{2} \\ & - \frac{E_i^{(2)} T^{(1)} + E_i^{(1)} T^{(2)}}{2} \Delta p_i - \frac{E_i^{(2)} \sigma_{jk}^{(1)} + E_i^{(1)} \sigma_{jk}^{(2)}}{2} \Delta d_{ijk} - \frac{\sigma_{ij}^{(2)} T^{(1)} + \sigma_{ij}^{(1)} T^{(2)}}{2} \Delta \alpha_{ij} \end{aligned} \tag{4.11}$$

Assuming that the field variables do not change during switching (i.e., $E_i^{(2)} = E_i^{(1)} = E_i$, $\sigma_{ij}^{(2)} = \sigma_{ij}^{(1)} = \sigma_{ij}$, and $T^{(2)} = T^{(1)} = T$), Equation (4.11) can be written as

$$\begin{aligned} \Delta \prod{}' = & -E_i \Delta P_i^r - \sigma_{ij} \Delta \varepsilon_{ij}^r - E_i \Delta d_{ijk} \sigma_{jk} - E_i \Delta p_i T - \sigma_{ij} \Delta \alpha_{ij} T \\ & - \frac{E_i \Delta \kappa_{ij}^{(\sigma,T)} E_j}{2} - \frac{\sigma_{ij} \Delta s_{ijkl}^{(E,T)} \sigma_{kl}}{2} - \frac{T \Delta \alpha_v^{(\sigma,E)} T}{2} \end{aligned} \tag{4.12}$$

The first two terms in Equation (4.12) represent the contribution due to the changes in the remnant polarization and the remnant strain, respectively, and they are identical to the corresponding terms in Hwang et al.'s model [9]. The following three terms represent the contributions due to piezoelectric, pyroelectric, and thermoelastic coupling, respectively.

The last three terms represent the change in electric, strain, and thermal energy, respectively.

It is assumed that the switching process is instantaneous; therefore, a critical energy can be used to represent the barrier that has to be overcome for switching to occur. A domain is predicted to switch according to the following criterion:

$$E_i \Delta P_i^r + \sigma_{ij} \Delta \varepsilon_{ij}^r + E_i \Delta d_{ijk} \sigma_{jk} + E_i \Delta p_i T + \sigma_{ij} \Delta \alpha_{ij} T + \frac{E_i \Delta \kappa_{ij}^{(\sigma,T)} E_j}{2} + \frac{\sigma_{ij} \Delta s_{ijkl}^{(E,T)} \sigma_{kl}}{2} + \frac{T \Delta \alpha_v^{(\sigma,E)} T}{2} \geq \psi_b(T) \tag{4.13}$$

where the left-hand side of Equation (4.13) represents the potential energy release during domain switching, and the right-hand side represents the critical energy barrier $\psi_b(T)$ associated with polarization switching. The critical energy barrier is assumed to be temperature-dependent.

In the absence of temperature effects, the present domain-switching criterion reduces to the model of Zeng and Rajapakse [15] such that

$$E_i \Delta P_i^r + \sigma_{ij} \Delta \varepsilon_{ij}^r + E_i \Delta d_{ijk} \sigma_{jk} + \frac{E_i \Delta \kappa_{ij}^{(\sigma,T)} E_j}{2} + \frac{\sigma_{ij} \Delta s_{ijkl}^{(E,T)} \sigma_{kl}}{2} \geq \psi_b(T) \tag{4.14}$$

Additionally, neglecting electromechanical coupling the present model reduces to Hwang et al.'s model [9] as follows:

$$E_i \Delta P_i^r + \sigma_{ij} \Delta \varepsilon_{ij}^r \geq \psi_b(T) \tag{4.15}$$

In Hwang et al. [9], it was assumed that the critical energy barriers $\psi_b(T)$ for both 90^o and 180^o domain switching are equal. It is assumed in the present model that barriers are

different. The key assumption in the proposed model is that 180° domain switching is composed of two successive 90° domain-switching occurrences; the critical energy barrier for 180° domain switching $\psi_b(T)|_{180^o}$ is therefore the summation of two critical energy barriers $\psi_b(T)|^1_{90^o}$ and $\psi_b(T)|^2_{90^o}$ such that

$$\psi_b(T)|_{180^o} = \psi_b(T)|^1_{90^o} + \psi_b(T)|^2_{90^o} \tag{4.16}$$

where $\psi_b(T)|^1_{90^o}$ is the energy barrier per unit volume for the first 90° domain switching, and $\psi_b(T)|^2_{90^o}$ is the energy barrier the second 90° domain switching, respectively.

The switching criterion (4.13) can then be rewritten for different switching types as

$$\Delta\prod' + \psi_b(T)|^1_{90^o} \geq 0.0 \tag{4.17.a}$$

$$\Delta\prod' + \psi_b(T)|_{180^o} \geq 0.0 \tag{4.17.b}$$

In order to find an expression for the different energy barriers, let us assume a tetragonal crystallite with a local polarization direction along its positive x_3-axis. Ferroelectric switching occurs when an applied electric field exceeds the coercive electric field E_c and moves the central ion to one of five possible off-centre tetragonal sites (four possible 90° and one possible 180° domain-switching directions), as shown in Figure 4.1. If 90° ferroelectric domain switching takes place, polarization in the x_3-direction switches from $+P^s$ to 0 (P^s is the magnitude of the spontaneous polarization). In the new polarization direction (x_1 or x_2-direction), polarization changes from 0 to $\pm P^s$.

This switching is usually accompanied by work done; in general, the electric work is described by

$$W_E^{90} = \left| \int E_i dD_i \right| = E_c(T) P^s(T) \tag{4.18}$$

where the coercive electric field $E_c(T)$ and the spontaneous polarization $P^s(T)$ are assumed to be temperature dependent.

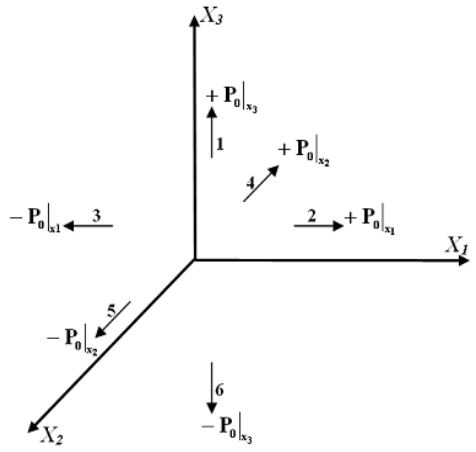

Figure 4.1. Possible switching directions.

On the other hand, in 180° ferroelectric domain switching, spontaneous polarization switches from $+P^s$ to $-P^s$ in the x_3-direction (i.e., the electric displacement changes by $-2P^s$), so that Equation (4.18) becomes

$$W_E^{180} = \left| \int E_i dD_i \right| = 2E_c(T) P^s(T) \tag{4.19}$$

Ferroelastic domain switching is caused by a stress sufficiently large to cause the central ion to move to one of the side sites (four possible 90° switching directions). Mechanical stress, on the other hand, can only cause 90° domain switching. In

ferroelastic switching caused by an applied stress $\sigma = \sigma_c$ (σ_c is the coercive stress), the change in spontaneous strain involves a reduction of strain by $\frac{3}{2}\varepsilon^s$ in the prior polarization direction and an increase of strain by the same amount in the new polarization direction. Assuming that the switching occurs at a constant stress, the mechanical work done during ferroelastic switching can be described by

$$W_M^{90} = \left| \int \sigma_{ij} d\varepsilon_{ij} \right| = \frac{3}{2} \sigma_c(T) \varepsilon^s(T) \tag{4.20}$$

where the coercive stress $\sigma_c(T)$ and the spontaneous strain $\varepsilon^s(T)$ are assumed to be temperature dependent.

The coupled electromechanical work during 90^o domain switching can be approximated as,

$$W_{EM}^{90} = \left| \int d_{ijk} E_k d\sigma_{ij} \right| = d_{33} E_c(T) \sigma_c(T) \tag{4.21}$$

where d_{33} is the longitudinal strain piezoelectric coefficient.

In Equation (4.21), both coercive electric field and stress are used but, in reality, only one of these is reached during 90^o domain switching. Note that since 180^o domain switching does not cause any change in strain, no coupled electromechanical work exists. Therefore, the energy-barriers for the first 90^o and 180^o ferroelectric domain switching can be expressed as

$$\psi_b(T)\Big|_{90^o}^1 = E_c(T) P^s(T) + d_{33} E_c(T) \sigma_c(T) \tag{4.22.a}$$

$$\psi_b(T)\big|_{180^o} = 2E_c(T)P^s(T) \tag{4.22.b}$$

Similarly, the energy-barrier density for 90^o ferroelastic domain switching (stress driven) can be written as,

$$\psi_b(T)\big|_{90^o}^{1} = \frac{3}{2}\sigma_c(T)\varepsilon^s(T) + d_{33}E_c(T)\sigma_c(T) \tag{4.23}$$

Note that the second term of the right-hand side of Equation (4.22.a) and (4.23) is relatively smaller when compared to the first term, and its effect on the overall electromechanical response will be investigated in Section 4.5.

4.4. Finite Element Formulation

A finite element formulation based on the weighted-residual method [27] is used in the present study. Isoparametric finite elements are used, and mechanical displacement u, electric potential φ, and temperature T are chosen as nodal degrees of freedom for each element. Two additional internal variables are contained within an element to represent its spontaneous polarization and spontaneous strain; they are assumed to be at the centroid of an element.

Using the governing equations presented in Section 4.2 and applying the weighted residual method, the following finite element equations are obtained.

$$\begin{aligned}
\left[K_{uu}\right]\{u\}+\left[K_{u\varphi}\right]\{\varphi\}&=\left\{f^{u}\right\}+\left\{f^{u^{s}}\right\}+\left\{f^{uT}\right\}\\
\left[K_{u\varphi}^{T}\right]\{u\}-\left[K_{\varphi\varphi}\right]\{\varphi\}&=\left\{f^{\varphi}\right\}+\left\{f^{\varphi^{s}}\right\}+\left\{f^{\varphi T}\right\}
\end{aligned} \tag{4.24}$$

where

$$\begin{aligned}
&K_{uu}=\int_{v}B^{u'}cB^{u}dv, \qquad K_{u\varphi}=\int_{v}B^{u'}eB^{\varphi}dv, \qquad K_{\varphi\varphi}=\int_{v}B^{\varphi'}\kappa B^{\varphi}dv\\
&f^{u}=\int_{s_t}N^{us'}t\,ds_{t}, \qquad f^{u^{s}}=\int_{v}B^{u'}c\varepsilon^{s}\,dv, \qquad f^{uT}=\int_{v}B^{u'}\lambda N^{T}dv\{T\}\\
&f^{\varphi}=-\int_{s_Q}N^{\varphi s'}Qds_{Q}, \qquad f^{\varphi^{s}}=\int_{v}B^{\varphi'}P^{s}\,dv+\int_{v}B^{\varphi'}e\varepsilon^{s}\,dv, \qquad f^{\varphi T}=-\int_{v}B^{\varphi'}pN^{T}dv\{T\}
\end{aligned} \tag{4.25}$$

where N^{u}, N^{φ}, and N^{T} are interpolation matrices containing shape functions for displacement u, voltage φ, and temperature T, respectively. B^{u}, B^{φ}, and B^{T} are

interpolation matrices for strain, electric field, and heat flux, respectively. f^{u^s} is a nodal load due to spontaneous strain; f^{φ^s} is a nodal electric charge due to spontaneous strain and spontaneous polarization; and f^{uT} and $f^{\varphi T}$ are a nodal load and a nodal electric charge due to temperature.

A finite element code based on the Eqs. (4.24) and (4.25) was developed by the authors. In the finite element scheme, each element is modeled as a grain of a single domain with the polarization vector randomly oriented [12, 13, 28]. The macroscopic response of a bulk piezothermoelastic continuum is obtained by averaging the responses of all domains over the volume. A random-number generator subroutine is used to obtain the principle axes, and hence the local material properties, of each domain. The random-number generator subroutine is based on the acceptance-rejection method [29]. Domains' orientations are generated according to predefined probability distribution functions [28].

During solution, loads are incrementally applied and the internal variables of each element (spontaneous strain and spontaneous polarization) remain constant until equilibrium is achieved. After each iteration, all elements are checked for switching based on the switching criterion (4.13), which is calculated at the centroid of an element. An element is checked for its first 90^o domain switching. If the element meets the switching criterion, it is then checked for a second 90^o switching. Consequently, new nodal loads f^{u^s} and f^{φ^s} are obtained by assembling the spontaneous strain and spontaneous polarization forces for all elements. Equation (4.25) is thereafter solved for new nodal values of $\{u\}$ and $\{\varphi\}$. This process is repeated until no more elements switch

and equilibrium is achieved at a specific load increment. Moreover, when an element switches, its material properties are updated accordingly.

It should be noted that in tetragonal structures, 90^o domain switching causes an increase of strain in the new polarization direction, and a reduction by the same amount in the old polarization direction [30]. As a result, neighboring domains that have different poling directions undergo different strains (strain incompatibility), and hence internal stresses are generated. During each iteration and after an element switches, internal and external load vectors are calculated and equilibrium is checked. If these vectors do not satisfy equilibrium, an incremental change in the nodal values, $\{\Delta u\}$ and $\{\Delta \varphi\}$, is computed based on the Newton-Raphson scheme [27]. Equilibrium is achieved when internal and external load vectors satisfy equilibrium, and all energetically favorable domains switch. The convergence criterion is obtained by requiring the norm of the out-of-balance load vector to be within a predefined small tolerance of the original load increment [27]. After equilibrium is achieved, the internal variables of all switched domains are updated, the volume-averaged total strain and electric displacement are calculated, and a new loading increment is introduced. The internal variables of switched domains are updated according to

$$\varepsilon_{ij}^{s}\Big|_{new} = a_{ik}a_{jl}\varepsilon_{kl}^{s}\Big|_{old}, \text{ and } P_i^s\Big|_{new} = a_{ij}P_j^s\Big|_{old} \tag{4.26}$$

where $a_{ij} = cos\ \gamma_{ij}$ are the direction cosines between new (after switching) and old (before switching) domain/element coordinate systems.

4.5. Results and Discussion

In this section, numerical results are presented to assess the performance of the proposed model. The materials used in the simulations were PZT discs manufactured by Kinetic Ceramics Inc., PZT discs manufactured by Piezo Kinetics Inc.

4.5.1. KCI-PZT disc under cyclic electric loading at different temperature

Since a typical multilayer PZT stack actuator consists of thin piezoelectric discs bonded together and sandwiched between electrodes, with adjoining discs having opposite poling directions, a single disc with two surface electrodes can be studied to represent an actuator.

Table 4.1. Properties of the soft KCI-PZT ceramics at room temperature.

Property	*Supplied value*	*Measured value*
Disc diameter (mm)	10	10
Electrode diameter (mm)	9.5	9.5
Disc thickness (mm)	0.5	0.5
Young's modulus c_{33} (GPa)	48	66
Poisson's ratio υ	0.3	0.3
Piezoelectric coefficient d_{33} (pC/N)	370	250
Dielectric permittivity κ_{33}	3400	2082
Coercive electric field E_c (MV/m)		1.08
Saturated remnant polarization P_{sat} (C/m^2)		0.45
Remnant polarization P^r (C/m^2)		0.40

The response of PZT thin discs corresponding to stack actuators custom made by Kinetic Ceramics Inc. (www.kineticceramics.com) was studied. The discs are made from soft PZT ceramics with a Curie temperature around 360 ^{o}C; Table 4.1 shows the

geometry and physical properties at room temperature of the discs considered in this study. The experimental results were provided by aixACCT, Advanced Customized Characterization Technology (www.aixacct.com).

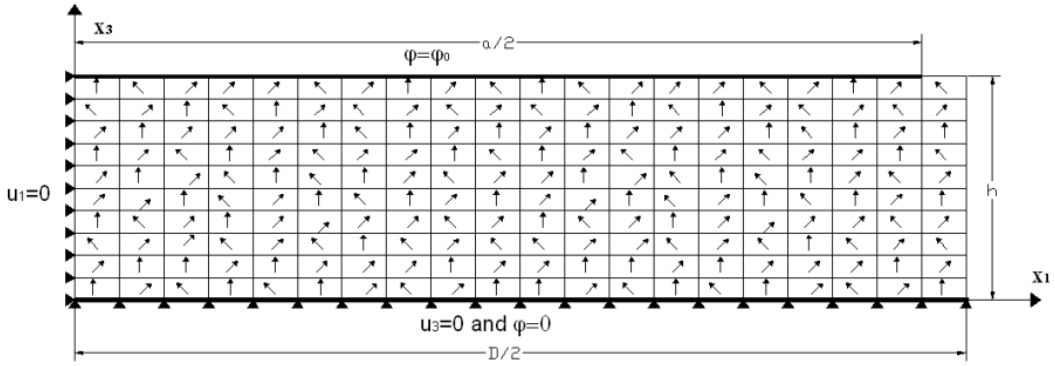

Figure 4.2. Geometry, boundary conditions and domain orientation of axisymmetric disk.

In the numerical simulations, the discs were modeled as axisymmetric domains using 800 (40 × 20) 2D four-node isoparametric elements with an element size of 125 × 25 μm^2. The polarization direction of each element was randomly assigned using a random-number generator. The mesh-size effect on the macroscopic response was numerically studied for three different element sizes: (1) 250 × 50 μm^2; (2) 125 × 25 μm^2; and (3) 100 × 25 μm^2. It was determined that the element size has an almost negligible effect on the average macroscopic response of the discs. The boundary conditions were imposed such that at the bottom surface of the disc (at $x_3 = 0$), both the vertical displacement u_3 and the applied electric potential φ were fixed at zero for all nodes of the mesh, as shown in Figure 4.2. At the central line of the disc (i.e., at $x_1 = 0$), the radial displacement u_1 was

fixed for all nodes. The applied electric potential φ was prescribed as φ_0 at the top surface (at $x_3 = h$). The right edge (at $x_1 = D/2$) was stress and charge free.

The applied electric-potential φ_0 at the upper surface was incrementally applied, and the temperature distribution, considered to be constant and uniform, was input into the model. Based on the experimental results provided by aixAACT, the temperature dependence of domain-switching behavior was accounted for by considering the linear dependency of the remnant polarization and the coercive field on temperature such that

$$P^r(T) = P^r(T_0) - \alpha_P(T - T_0) \tag{4.27.a}$$

$$E_c(T) = E_c(T_0) - \alpha_E(T - T_0) \tag{4.27.b}$$

where T is a given temperature; $P^r(T_0)$ and $E_c(T_0)$ are the remnant polarization and the coercive field at room temperature, respectively; α_p and α_E are the slopes of the remnant polarization temperature and coercive field temperature curves, respectively. It was found that $P^r(T_0)=0.40C/m^2$, $\alpha_p=0.00084C/m^{2o}C$, $E_c(T_0)=1.08MV/m$, and $\alpha_E=0.0023MV/m^oC$ based on the experimental results. The effect of electromechanical coupling work on the switching energy barriers was studied. It was determined that the second term in Equation (22.a) and (4.23), has a negligible effect on the energy barriers, and it can be conveniently dropped from the two switching criteria.

The D_3-E_3 and S_3-E_3 hysteresis loops were computed. Figure 4.3 shows a comparison of the results from the present model with the results based on the model developed by Hwang et al. [9], and the experimental results under an electric loading of E = 3.0 MV/m at three different temperatures: (a, d) 25 ^{o}C; (b, e) 50 ^{o}C; and (c, f) 200 ^{o}C. All

experimental results were obtained from tests done at the laboratories of aixACCT. It can be seen from Figure 4.3(a-c) that the present model successfully predicts the experimental D_3-E_3 hysteresis loops at the three different temperatures. It is noted that the experimental domain-switching starting points (for example, points *B* and *G* in Figure 4.3-a) show rounded edges in the D_3-E_3 hysteresis loops, whereas the current model shows slightly sharper edges. The sharp edges of the simulation could possibly be due to the assumption that domain switching is an instantaneous process. It can also be seen from Figure 4.3(a-c) that temperature has a significant effect on the D_3-E_3 curves; the remnant polarization, saturation polarization, and coercive electric field steadily decrease with increasing temperature.

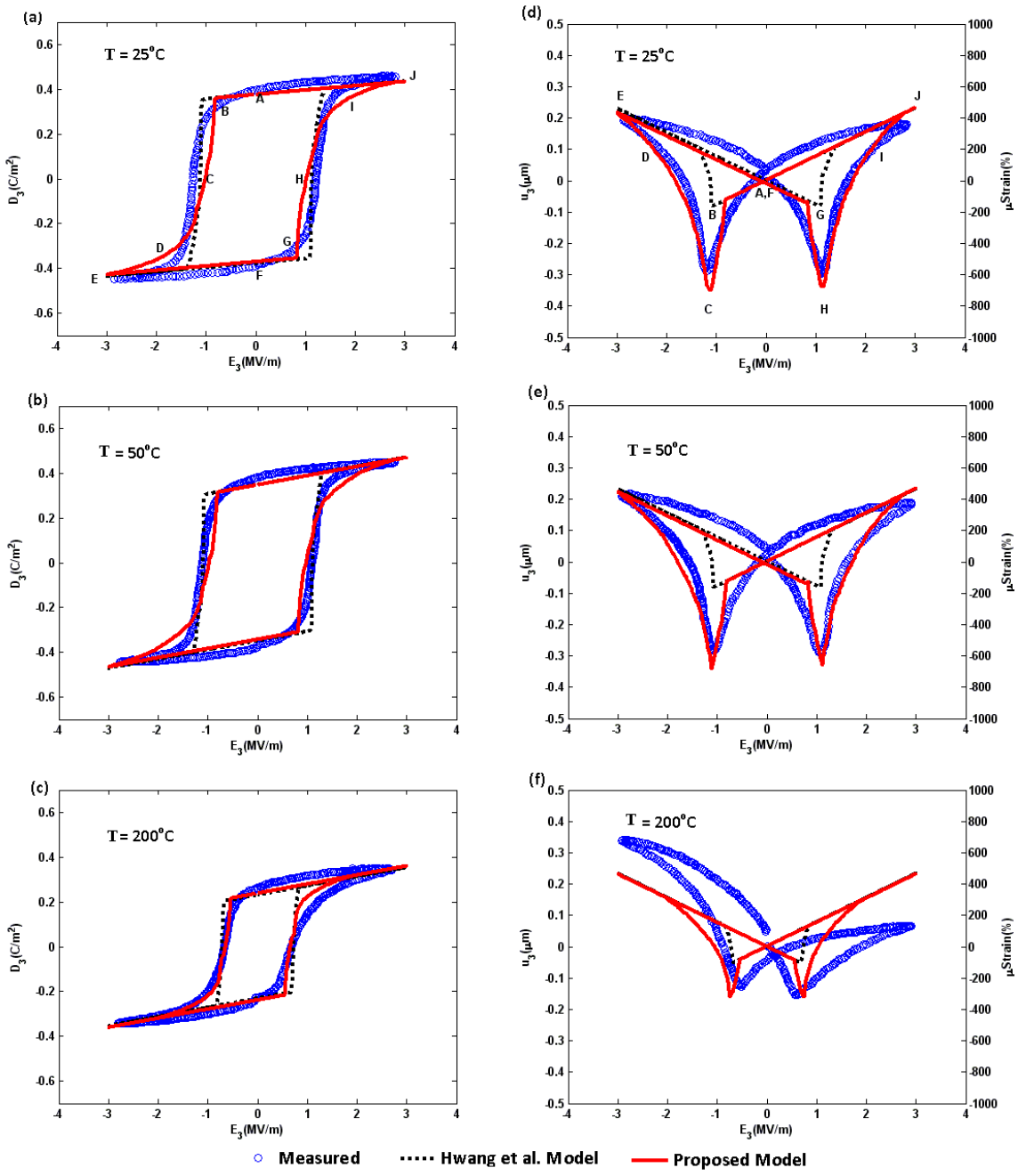

Figure 4.3. Simulated and measured D_3-E_3 (a-c), and S_3-E_3 (d-f) hysteresis loops under pure electric loading at three different temperatures.

Similarly, Figure 4.3(d-f) show that the present model can predict the experimentally obtained S_3-E_3 hysteresis loops at room and moderately above room temperatures. However, at 200 ^{o}C, the experimental results [Figure 4.3(f)] show that the butterfly loop is no longer symmetric, and the current model results deviate substantially from the experimental results. This could possibly be related to microstructural changes and other nonlinearities in the material that might occur at high temperature, which are not accounted for in the present model.

Figure 4.3 also shows the prediction obtained using Hwang et al.'s model. It can be seen from Figure 4.3(a-c) that Hwang et al.'s model also reasonably predicts the experimentally obtained D_3-E_3 hysteresis loops at the three different temperatures. However, their model shows a steeper slope near the coercive electric field, whereas our model shows a relatively gradual slope during domain switching. As previously mentioned, it was assumed in Hwang et al.'s model that the energy required to activate 180^{o} or 90^{o} domain switching is the same. Consequently, 90^{o} domain switching was not likely predicted, and only 180^{o} switching events were observed, resulting in a steeper slope. This steeper slope is better seen in Figure 4.3(d-f) where it can be seen that the predicted value of the strain at the tails of the butterfly loops using Hwang et al.'s model was almost one-quarter of the actual measured strain. As the energy thresholds for 90^{o} and 180^{o} domain switching are the same, Hwang et al.'s model causes only 180^{o} switching under pure electric loading, which does not cause any change in strain. As a result, less strain is induced and the butterfly loop simulations are not very close to the experimental results. On the other hand, our proposed model considers 180^{o} switching as

a result of two 90^o switching events that are associated with changes in strain, leading to a better prediction of the butterfly loops.

In order to demonstrate the evolution of domain switching, the loading path is assigned the symbols *A* to *J*, as shown in Figure 4.3(a) and (d); Points A to J are identical in both figures. The evolution of domain switching at room temperature corresponding to the above points is shown in Figure 4.4. The initial state of a domain, 0^o orientation, is shown in red. When a domain experiences its first 90^o switching, it is represented in green, and then by blue when it undergoes the second 90^o switching (180^o). Point A is referred to as the initial poled state where all domains are in their 0^o orientation. At an electric field slightly less than the coercive field, Point B, energetically favorable domains started to achieve their first 90^o domain switching. The rate of negative strain was therefore increased, as shown in Figure 4.3(d), since 90^o domain switching causes an increase in strain in the new polarization direction and a reduction by the same amount in the old polarization direction. At this point, only a small fraction of domains, shown in green, had achieved their first 90^o domain switching. These domains were randomly distributed in the specimen, as shown in Figure 4.4(B).

At Point *C*, almost 75% of the domains met the switching criterion and achieved their first 90^o-reorientation. Immediately after this point, the second 90^o domain reorientation begins. At Point D, some domains achieved their second 90^o domain switching. At Point *E*, all energetically favorable domains that met the switching criterion achieved their second 90^o reorientation. Although the specimen reached the saturation state at this point, it is noted that there were still some domains that did not complete their second 90^o domain switching (elements with green color). According to Hwang et al.'s model, these

elements would have either switched 180° or not switched at all, which may not reflect the actual behavior. After Point *F*, the electric field was reversed, domains re-switched, and the specimen was brought back to the initial poling state *A*.

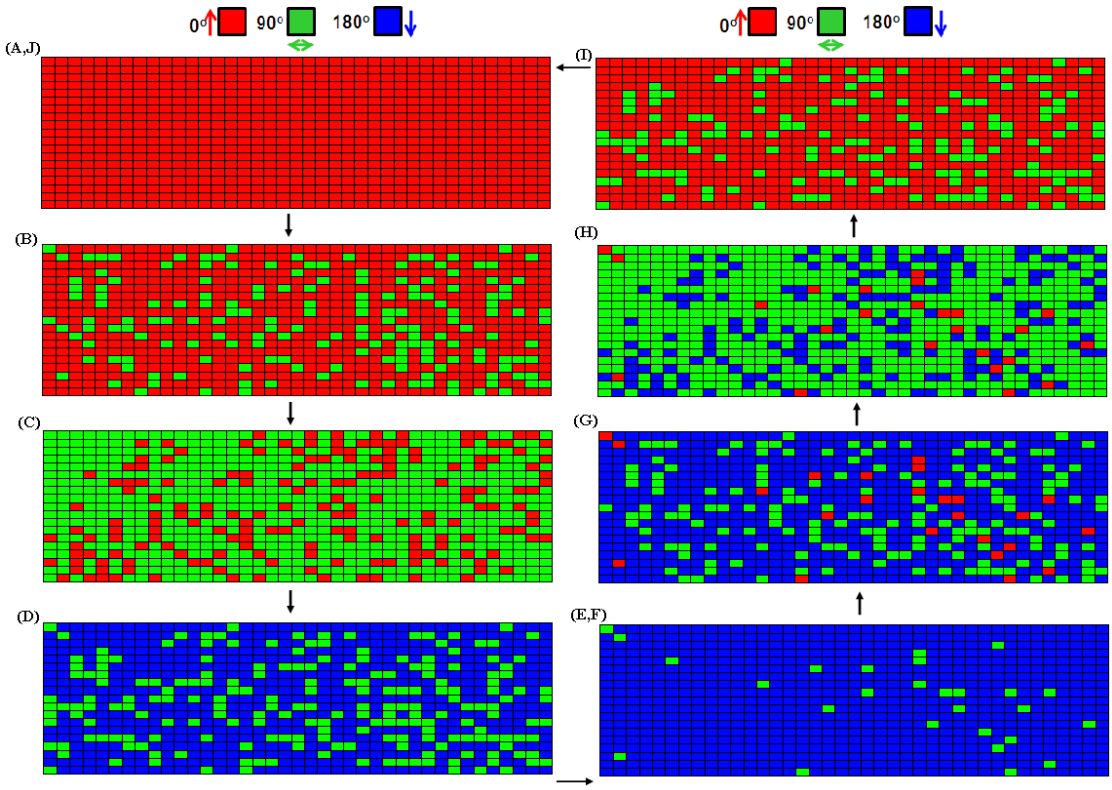

Figure 4.4. Evolution of domain-switching under a full cycle of pure electric loading at room temperature.

4.5.2. PZT disc under constant preload and cyclic electric loading at room temperature

In this section, selected numerical results are presented to assess the performance of the present model under combined electromechanical loading. The numerical results are compared with the experimental results obtained by Yimnirun et al. [31], who studied the effect of preload compressive stress on the electric displacement D_3-E_3 hysteresis loops of soft PZT ceramics manufactured by Piezo Kinetics Inc. (www.piezo-kinetics.com). The geometry and physical properties of the relevant PZT discs are shown in Table 4.2.

A 2D axisymmetric model was used to model the PZT discs. 40 × 20 2D four-node isoparametric elements were used with an element size of 125 × 50 μm^2. Similar boundary conditions were imposed as in the previous example, along with a compression preload of - 23.47 MPa imposed on the top surface ($x_3 = h$). In this case, the compressive preload stress was incrementally applied in the polarization direction, parallel to the x_3-axis, with no electric field applied. Afterward, the cyclic electric field was incrementally applied.

Table 4.2. Properties of the soft Piezo Kinetics Inc. ceramics [31].

Property	***Supplied value***
Disc diameter (mm)	10
Disc thickness (mm)	1.0
Young's modulus c_{33} (GPa)	66
Poisson's ratio υ	0.31
Piezoelectric coefficient d_{31} (pC/N)	-270
Piezoelectric coefficient d_{33} (pC/N)	550
Piezoelectric coefficient d_{15} (pC/N)	720
Dielectric permittivity κ_{33}	3400

The stable-electric displacement (D_3-E_3) loops were computed. Figure 4.5 shows a comparison of the numerical simulations from the present model, the Hwang et al.'s model [9], and the experimental results [31] under a cyclic-uniaxial electric load of E = 2.0 MV/m with: (a) zero MPa; and (b) -23.47 MPa applied compressive stress. It can be seen from Figure 4.5 that the present model predicts the experimental D_3-E_3 hysteresis loops quite well. Figure 4.5(b) shows that the constant preload has a significant effect on the electric-displacement hysteresis behavior. The resulting hysteresis loop shows a reduction in the remnant polarization as well as in the D_3-E_3 hysteresis area, which physically represents the dissipation energy, with the applied mechanical stress. This phenomenon is called the *depolarization phenomenon* [8]. The reduction in the remnant polarization can be explained by the 90^o domain reorientation caused by the mechanical stress. When a sufficiently large compressive stress was applied in the polarization direction, energetically favorable domains experienced 90^o switching. Figure 4.6 shows the effect of the compressive mechanical stress on (a) electric displacement D_3; and (b) longitudinal strain S_3 at zero electric field. Points *A'* and *A* represent the start and end, respectively, of 90^o domain switching. They are identical in both figures. It can be seen from Figure 4.6(a) and (b) that both D_3 and S_3 are linearly related to the applied mechanical stress until Point *A'* is reached. At Point *A'*, 90^o domain switching commenced, and a faster reduction of both D_3 and S_3 occurred. At Point *A*, all energetically favorable domains completed their first 90^o domain switching, with almost 50 % of the domains switched. The linear behavior was then retrieved and no more domains switched until the electric field was incrementally applied. The electric field loading path was *A*-*B*-*C*-*D*-*E*-*F*, as shown in Figure 4.5(b).

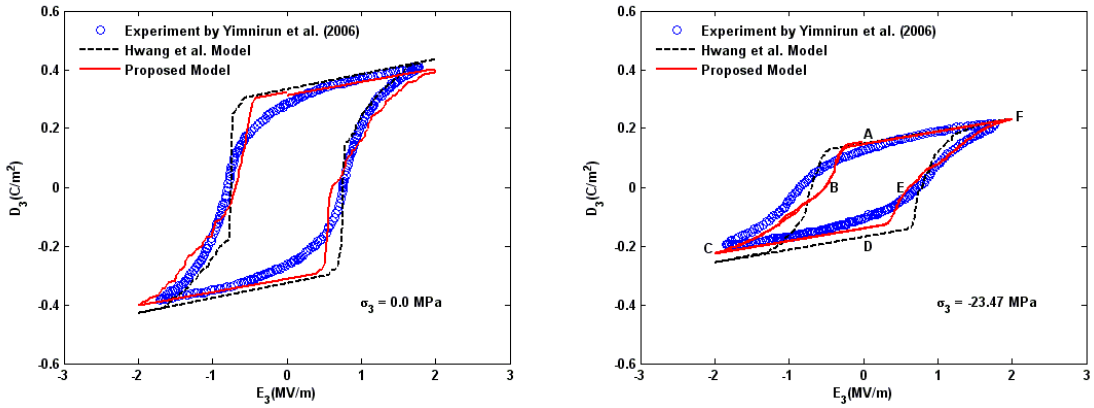

Figure 4.5. Comparison of theoretical and experimental results under (a) pure electric loading, and (b) combined electromechanical loading at room temperature.

The evolution of domain switching under combined electromechanical loading corresponding to the above points is shown in Figure 4.7. Point *A* represents the polarization state at zero electric field under a mechanical preload σ_3 = -23.47 MPa. The remnant polarization at this point is almost 50% less than in the stress-free state. Similar to the previous example, the initial state of a domain is shown in red, 90^o reorientation in green, and 180^o reorientation in blue. It can be seen from Figure 4.7 that the domains that experienced 90^o switching under the mechanical preload, shown in green at Point *A*, did not experience any further switching as the electric field was increased. In other words, these domains were orthogonally trapped and could not be reoriented by the applied electric field. This phenomenon may explain the reduction in the remnant polarization with increased stress. As the electric field increased, the un-switched domains started to switch, following a pattern similar to that seen in the previous example. An initial 90^o

domain switching occurred at Point *B*, as shown in Figure 4.7, followed by a second 90° domain switching, as shown at Points *C* and *D*.

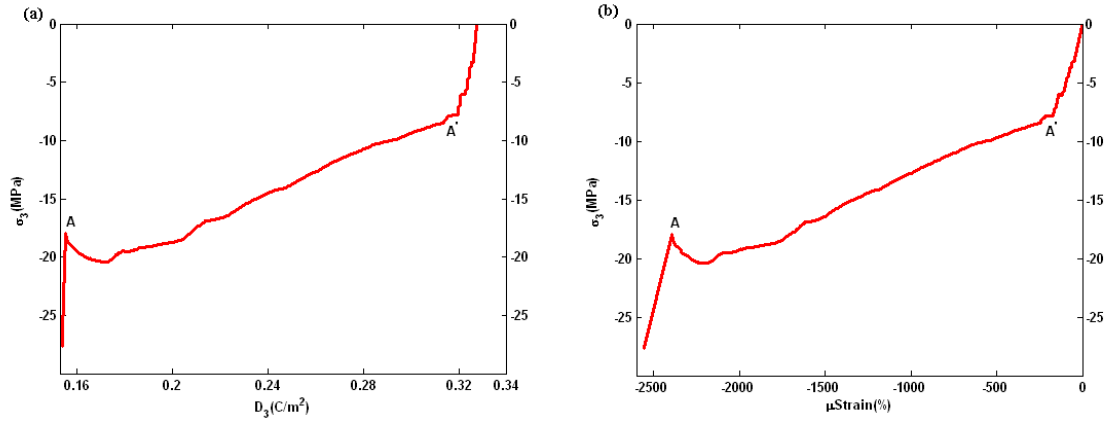

Figure 4.6. Effect of compressive preload on (a) electric displacement, and (b) longitudinal strain.

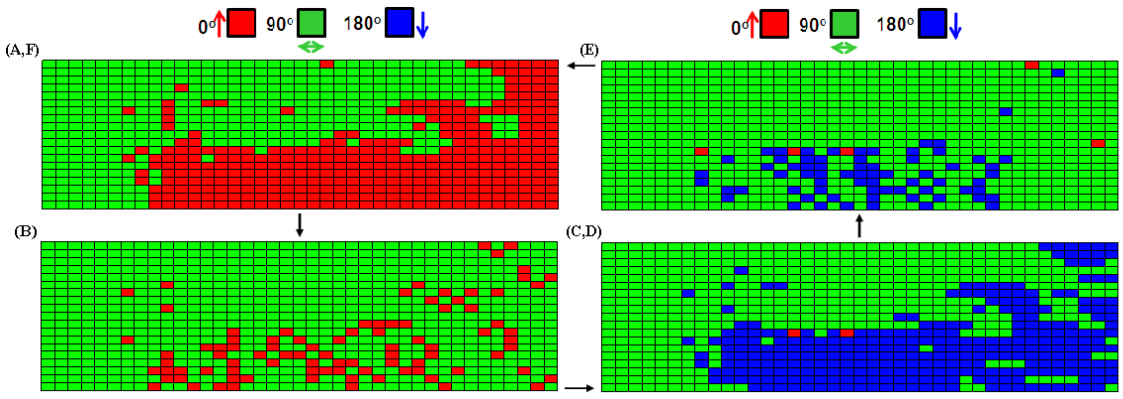

Figure 4.7. Evolution of domain-switching under combined electromechanical loading.

4.6. Conclusions

A temperature-dependent domain-switching model for ferroelectric materials that accounts for the influence of piezothermoelastic coupling and material anisotropy was developed. The switching criterion is based on the fundamental concepts of Hwang et al. [9]. The proposed model considers 90^o switching to be a prerequisite for 180^o switching. This two-step switching process suggests different energy barriers for 90^o electric–field driven switching and 90^o mechanical–stress driven switching. As a result, the present model successfully predicted the experimentally obtained D_3-E_3 and S_3-E_3 hysteresis loops at different applied electric-field magnitudes, stress preload, and temperatures. It also provided a better prediction of the butterfly loops than the previous models. Domain-switching evolution was also studied and the numerical results show that some domains did not complete a second 90^o domain switching, which validated the two-step switching process assumption. The present model could serve as a valuable tool for the design of piezoceramic actuators over a broad range of loading and temperatures.

4.7. Bibliography

[1] Schuh C, Steinkopff T, Wolff A, Lubitz K. Piezoceramic multilayer actuators for fuel injection systems in automotive area. In: *Proceedings of SPIE* 2003;3992:165.

[2] Senousy MS, Li F, Mumford D, Gadala MS, Rajapakse RKND. Thermo-electro-mechanical performance of piezoelectric stack actuators for fuel injector applications. *Journal of Intelligent Material Systems and Structures* 2009;20:387.

[3] Senousy MS, Rajapakse RKND, Mumford D, Gadala MS. Self-heat generation in piezoelectric stack actuators used in fuel injectors. *Journal of Smart Materials and Structures* 2009;18:045008.

[4] Li FX, Rajapakse RKND, Mumford D, Gadala M. Quasi-static thermo-electro-mechanical behaviour of piezoelectric stack actuators. *Smart Materials and Structures* 2008;17:015049.

[5] Ochi A, Takahashi S, Tagami S. Temperature Characteristics for Multilayer Piezoelectric Ceramic Actuator. *Japanese Journal of Applied Physics* 1985;24:209.

[6] Jaffe B, Cook WR, Jaffe H. Piezoelectric Ceramic. *Academic Press Inc.* London 1971.

[7] Kamlah M, Jiang Q. A constitutive model for ferroelectric PZT ceramics under uniaxiai loading. *Smart Materials and Structures* 1999;8:441.

[8] Kamlah M, Tsakmakis C. Phenomenological modeling of the non-linear electro-mechanical coupling in ferroelectrics. *International Journal of Solids and Structures* 1999;36:669.

[9] Hwang SC, Lynch CS, McMeeking RM. Ferroelectric/ferroelastic interactions and a polarization switching model. *Acta Materialia* 1995;43:2073.

[10] Fotinich Y, Carman GP. Nonlinear behavior of polycrystalline piezoceramics. In: *Proceedings of SPIE* 2000;3992:319.

[11] McMeeking RM, Hwang SC. On the potential energy of a piezoelectric inclusion and the criterion for ferroelectric switching. *Ferroelectrics* 1997;200:151.

[12] Hwang SC, McMeeking RM. A finite element model of ferroelectric polycrystals. *Ferroelectrics* 1998;211:177.

[13] Hwang SC, McMeeking RM. A finite element model of ferroelastic polycrystals. *International Journal of Solids and Structures* 1999;36:1541.

[14] Jiang L. Fracture and fatigue behaviour of piezoelectric materials. Ph.D Thesis, *Purdue University*, West Lafayette, IN, USA 1998.

[15] Zeng X, Rajapakse RKND. Eshelby tensor for piezoelectric inclusion and application to modeling of domain switching and evolution. *Acta Materialia* 2003;51:4121.

[16] Huber J, Fleck N, Landis CM, McMeeking RM. A constitutive model for ferroelectric polycrystals. *Journal of the Mechanics and Physics of Solids* 1999;47:1663.

[17] Hwang SC, Huber JE, McMeeking RM, Fleck NA. The simulation of switching in polycrystalline ferroelectric ceramics. *Journal of Applied Physics* 1998;84:1530.

[18] Kamlah M, Liskowsky AC, McMeeking RM, Balke H. Finite element simulation of a polycrystalline ferroelectric based on a multidomain single crystal switching model. *International Journal of Solids and Structures* 2005;42:2949.

[19] Li FX, Rajapakse RKND. Nonlinear finite element modeling of polycrystalline ferroelectrics based on constrained domain switching. *Computational Materials Science* 2008;44:322.

[20] Chen W, Lynch CS. A micro-electro-mechanical model for polarization switching of ferroelectric materials. *Acta Materialia* 1998;46:5303.

[21] Lynch CS. The effect of uniaxial stress on the electro-mechanical response of 8/65/35 PLZT. *Acta Materialia* 1996;44:4137.

[22] Chen W, Lynch CS. Multiaxial constitutive behavior of ferroelectric materials. *Journal of Engineering Materials and Technology* 2001;123:169.

[23] Ikeda T. Fundamentals of Piezoelectricity. *Oxford University Press Inc.* New York, USA 1996.

[24] Landis CM. Self-consistent and phenomenological constitutive models for ferroelectric ceramics. Ph.D Thesis*, University of California.*, Santa Barbara, CA, USA 1999.

[25] Landis CM. Fully coupled, multi-axial, symmetric constitutive laws for polycrystalline ferroelectric ceramics. *Journal of the Mechanics and Physics of Solids* 2002;50:127.

[26] Landis CM. A new finite-element formulation for electromechanical boundary value problems. *Int. J. Numer. Meth. Engng* 2002;55:613.

[27] Bathe KJ, Wilson EL. Numerical methods in finite element analysis. *Prentice-Hall Inc*. Englewood Cliffs, USA 1976.

[28] Li F, Fang D. Simulations of domain switching in ferroelectrics by a three-dimensional finite element model. *Mechanics of Materials* 2004;36:959.

[29] Devroye L. Non-uniform random variate generation. *Springer-Verlag* New York, USA 1986.

[30] Hwang SC, Waser R. Study of electrical and mechanical contribution to switching in ferroelectric ferroelastic polycrystals. *Acta Materialia* 2000;48:3271.

[31] Yimnirun R, Laosiritaworn Y, Wongsaenmai S. Effect of uniaxial compressive pre-stress on ferroelectric properties of soft PZT ceramics. *Journal of Physics D: Applied Physics* 2006;39:759.

Chapter 5

5. Conclusions

5.1. Summary and Conclusions

The major findings and conclusions of the present study are summarized as follows:

1. A comprehensive experimental investigation of the thermo-electro-mechanical performance of soft PZT actuators under operating conditions relevant to fuel injection is provided in this thesis. The experimental findings provide a better understanding of the overall response of actuators under different controlling parameters, such as electric field magnitude, frequency, driving-field rise time (inversely proportional to holding time), DC offset, duty cycle, and ambient temperature. Dynamic stroke, piezoelectric coefficient d_{33}, and self-heating are also investigated. It is found that:

    a. In the temperature range of -30 ^{o}C to 80 ^{o}C, dynamic stroke increases with temperature. At electric-field levels ≥ 1.0 kV/mm, a nonlinear stroke-temperature transition zone occurs between 40 ^{o}C and 55 ^{o}C, which may be explained by the increased activities of non-180^{o} domain-wall motions. Dynamic stroke is also shown to increase with decreased rise time t_r. Dynamic stroke is investigated over a duty cycle range of 10 to 80 %,

under four different wave forms and different frequencies. It is concluded that duty cycle percentage has a negligible effect on dynamic stroke.

b. At low electric-field magnitudes (<1.0 kV/mm), d_{33} is not affected by DC offset. On the other hand, at higher electric fields, d_{33} decreases slightly with increased DC offset. d_{33} is also shown to increase with increased electric-field at different temperatures. The increase in d_{33} may be due to intrinsic and extrinsic contributions, with extrinsic contributions resulting from increased actions of non-180^o domain walls.

c. Self-heating is experimentally investigated under sinusoidal electric loading at different frequencies and electric-field magnitudes. Results show that PZT actuators characteristically generate heat when they are driven under high electric-field magnitude and/or frequency. Moreover, duty cycle d_t is found to considerably affect the amount of heat generated; decreasing d_t significantly decreases heat generated. For instance, at E = 1.4 kV/mm, f = 200 Hz, and d_t = 100 %, the steady-state temperature increase was almost 27 ^{o}C, whereas it was almost 7 ^{o}C under d_t = 25 %.

2. A simplified mathematical model for heat generation is developed where temperature increase can be obtained in a classical exponential closed-form. The developed model provides an invaluable tool for designing piezoelectric actuators for fuel injectors, and for designing high-power actuators. The model has the following characteristics:

a. The model accounts for different parameters, such as geometry, magnitude and frequency of applied-electric field, duty cycle percentage, and surrounding properties. The model relates self-heating in the actuators to displacement hysteresis D_f. Although the dependence of hysteresis on temperature was not considered in the previous models [1, 2], temperature and electric-field dependences of D_f are experimentally obtained and considered in our model. At different electric-field magnitudes, displacement hysteresis is shown to increase with increased temperature over a range of -30 ^{o}C to 80 ^{o}C. D_f is found to increase slightly with increased frequency.

b. The closed-form solution for δT is obtained for three solution cases: *(i)* D_f is temperature dependent; *(ii.a)* D_f is constant; and *(ii.b)* D_f is incrementally updated with increased temperature. All cases show that the steady-state temperature increase, δT_{∞}, is governed by actuator geometry, material properties, and loading. At f = 100 Hz, all solution cases are in good agreement with experimental results, whereas at higher frequencies, Case *ii.a* deviates from the experimental results. Consequently, it is concluded that the dependence of D_f on temperature and electric field should not be neglected at large electric-field magnitudes and/or frequencies. The model can also successfully predict temperature increase under different surrounding conditions such as in the case of an aluminum bracket which can be used in thermal management.

3. A temperature-dependent domain-switching model for PZT materials is developed. The major findings of the model are summarized as follows:

    a. The model is based on reduction in potential energy. It assumes that field variables (i.e., electric field, mechanical stress, and temperature) do not change during switching, whereas remnant strain, remnant polarization, and material properties' tensors rotate with domains reorientation. The developed criterion constitutes the contributions due to changes in remnant strain, remnant polarization, full thermo-electro-mechanical coupling, and different energy types: electric, strain, and thermal energies. Moreover, the model considers 180^o switching to be composed of two 90^o switching events. Different energy barriers for 90^o electric–field driven switching and 90^o mechanical–stress driven switching are assumed. In both cases, numerical results show that the influence of coupled electromechanical work is relatively smaller than that of electric work and/or mechanical work.

    b. The developed model can successfully predict the macroscopic polarization–electric field (dielectric) and strain–electric field (butterfly) hysteresis loops at different electric-field magnitudes, preload stresses, and temperatures. Dielectric and butterfly loops of PZT materials are compared with experimental results as well as with those in the literature [3, 4]. The present model provides a better prediction of the hysteresis loops.

c. Under pure electric loading and combined electromechanical loading, the predicted hysteresis loops show sharp edges at the domain-switching starting points, which may be explained by the assumption that domain switching is an instantaneous process. A compressive mechanical preload applied parallel to the polar direction is shown to cause *depolarization* due to 90^o domain reorientation.

d. Domain-switching evolution can be demonstrated using the present model. Numerical results for 180^o and 90^o domain evolution in a PZT disc under pure electric loading reveal that some domains do not complete a second 90^o domain switching, which validates the two-step switching process assumption. Under combined electromechanical loading, 90^o mechanical–stress driven switching is shown to be irreversible. In other words, domains that experience 90^o switching under a mechanical preload are trapped and do not experience any further switching as the electric field is increased.

5.2. Recommendations for Future Work

To deepen the understanding of the overall performance of piezoelectric actuators under different operating conditions, the following suggestions are made for future work:

1. The proposed self-heating model shows that temperature increase within the actuators is size and geometry dependent. The model can therefore form the basis of an optimization algorithm for designing optimum piezoelectric

actuators adapted to the operational requirements of fuel injection, with a maximum stroke and minimum self-heating.

2. In the proposed switching criterion, domain-wall dynamics are not considered (i.e., domain reorientation is assumed to be instantaneous). However, domain switching is the result of domain-wall nucleation followed by domain-wall propagation. A switching model that considers domain-wall dynamics may be helpful in explaining the constitutive behavior of ferroelectric materials.

3. Piezoelectric ceramics are brittle and susceptible to cracking under cyclic electric field and/or mechanical loading [5]. Moreover, the electrode-tip is an electric-field concentration zone that may undergo failure or dielectric breakdown. The proposed switching criterion, in Chapter 4, may be extended to better understand the fracture behavior of multilayer stacks, particularly at the electrode tip zone.

5.3. Bibliography

[1] Lesieutre GA, Fang L, Koopmann GH, Pai SP, Yoshikawa S. Heat generation of a piezoceramic induced-strain actuator embedded in a glass/epoxy composite panel. 1996;2717:267.

[2] Zheng J, Takahashi S, Yoshikawa S, Uchino K, de Vries JWC. Heat generation in multilayer piezoelectric actuators. *Journal of the American Ceramic Society* 1996;79:3193.

[3] Hwang SC, Lynch CS, McMeeking RM. Ferroelectric/ferroelastic interactions and a polarization switching model. *Acta Materialia* 1995;43:2073.

[4] Yimnirun R, Laosiritaworn Y, Wongsaenmai S. Effect of uniaxial compressive pre-stress on ferroelectric properties of soft PZT ceramics. *Journal of Physics D: Applied Physics* 2006;39:759.

[5] Shindo Y, Narita F, Horiguchi K, Magara Y, Yoshida M. Electric fracture and polarization switching properties of piezoelectric ceramic PZT studied by the modified small punch test. *Acta Materialia* 2003;51:4773.

Appendix A

FE Formulation of Piezothermoelastic Materials

The governing equations describing the behavior of a piezothermoelastic continuum were given in Chapter 4.

The mechanical strain ε_{ij}, electric field E_i, and heat flux q_i are defined as the derivatives of the mechanical displacement vector u_i, electric potential φ, and temperature T, respectively, such that

$$\varepsilon_{ij} = 1/2\left(u_{i,j} + u_{j,i}\right); \quad E_i = -\varphi_{,i}; \text{ and } \quad q_i = -k_{ij}T_{,j} \tag{A.1}$$

For a material volume $\boldsymbol{v}$ subjected to virtual displacement δu_i, temperature δT, and electric potential $\delta\varphi$

$$\int_v \sigma_{ij,j}\,\delta u_i\,dv + \int_v D_{i,i}\,\delta\varphi\,dv + \int_v k_{ij}T_{,ij}\,\delta T\,dv = 0 \tag{A.2}$$

Applying the divergence theorem yields,

$$\begin{aligned} &-\int_v \sigma_{ij}\delta u_{i,j}\,dv + \int_{s_t} \sigma_{ij}n_j\,\delta u_i\,ds_t - \int_v D_i\,\delta\varphi_{,i}\,dv \\ &+\int_{s_Q} D_i\,n_i\delta\varphi\,ds_Q - \int_v k_{ij}T_{,j}\delta T_{,i}\,dv + \int_{s_q} k_{ij}T_{,j}n_i\,\delta T\,ds_q = 0 \end{aligned} \tag{A.3}$$

Making use of the symmetry property of the stress and strain tensors, and applying Equation (A.2) results in

$$-\int_v \sigma_{ij}\delta\varepsilon_{ij}\,dv+\int_{s_t} t_i\,\delta u_i\,ds_t+\int_v D_i\,\delta E_i\,dv-\int_{sQ} Q\,\delta\varphi\,ds_Q- \\ -\int_v k_{ij}T_{,j}\delta T_{,i}\,dv+\int_{sq} q\,\delta T\,ds_q+\int_{sq} h_v\left(T_f-T\right)\delta T\,ds_q=0.0 \tag{A.4}$$

Substituting (A.1) into (A.4) and rearranging the terms results in

$$-\int_v \delta\varepsilon_{ij}c_{ijkl}^{(E,T)}\varepsilon_{kl}\,dv+\int_v \delta\varepsilon_{ij}c_{ijkl}^{(E,T)}\varepsilon_{kl}^{r}\,dv+\int_v \delta\varepsilon_{ij}e_{ijk}E_k\,dv+\int_v \delta\varepsilon_{ij}\lambda_{ij}T\,dv \\ +\int_{s_t} t_i\,\delta u_i\,ds_t+\int_v \delta E_i e_{ijk}\varepsilon_{jk}\,dv+\int_v \delta E_i e_{ijk}\varepsilon_{jk}^{r}\,dv+\int_v \delta E_i\kappa_{ij}^{(\varepsilon,T)}E_j\,dv \\ +\int_v \delta E_i P_i^{r}\,dv+\int_v \delta E_i p_i T\,dv-\int_{sQ} Q\,\delta\varphi\,ds_Q-\int_v k_{ij}T_{,j}\delta T_{,i}\,dv \\ +\int_{sq} q\,\delta T\,ds_q+\int_{sq} h_v\left(T_f-T\right)\delta T\,ds_q=0.0 \tag{A.5}$$

Two dimensional- four node quadrilateral isoparametric elements with four DOFs per node are used. Isoparametric shape functions are used to interpolate the mechanical displacement u, the electric potential φ, and the temperature T distributions within an element such that

$$u_i=N_{ij}^{u}\overline{u}_j,\ i=1,2 \text{ and } j=1,2,..8$$

$$\varphi=N_i^{\varphi}\overline{\varphi}_i,\ i=1,2,..4 \tag{A.6}$$

$$T=N_i^{T}\overline{T}_i,\ i=1,2,...4$$

where a bar above a variable denotes the nodal values of the variable within an element. N^u, N^φ, and N^T are element shape functions for displacement, electric potential and temperature, respectively, and written as:

$$N^u = \left[\begin{array}{c|cc|c} ..... & N_i & 0 & ..... \\ & 0 & N_i & \end{array} \right], \text{ and } N^T = N^\varphi = \left[.....|N_i|.... \right], \; i=1,2,..4 \tag{A.7}$$

where

$$N_1(r,s) = \frac{1}{4}(1+r)(1+s) \quad N_2(r,s) = \frac{1}{4}(1-r)(1+s)$$
$$N_3(r,s) = \frac{1}{4}(1-r)(1-s) \quad N_4(r,s) = \frac{1}{4}(1+r)(1-s) \tag{A.8}$$

The coordinate approximation for a general point within an element may be written as:

$$x = N_i x_i = N_1 x_1 + N_1 x_1 + N_3 x_3 + N_4 x_4$$
$$y = N_i y_i = N_1 y_1 + N_2 y_2 + N_3 y_3 + N_4 y_4 \tag{A.9}$$

The shape function matrices can be differentiated to obtain the mechanical strain ε_{ij}, electric field E_i, and temperature gradient $T_{,i}$ distributions within an element such that

$$\varepsilon_i = B^u_{ij} \overline{u}_j, \; i=1,..,3 \text{ and } j=1,2,..8$$
$$E_i = -B^\varphi_{ij} \overline{\varphi}_j, \; i=1,2 \text{ and } j=1,2,..4 \tag{A.10}$$
$$T_{,i} = -B^T_{ij} \overline{T}_j, \; i=1,2 \text{ and } j=1,2,..4$$

where B^u, B^φ, and B^T are the linear differentiation of N^u, N^φ, and N^T, respectively. B matrices can then be written as

For plane stress and plane strain formulation:

$$B^u = \begin{bmatrix} \cdots\cdots & \left|\begin{matrix} \frac{\partial N_i}{\partial x} & 0 \\ 0 & \frac{\partial N_i}{\partial y} \\ \frac{\partial N_i}{\partial y} & \frac{\partial N_i}{\partial x} \end{matrix}\right| & \cdots\cdots \end{bmatrix}, \text{ and } B^T = B^\varphi = \begin{bmatrix} \cdots\cdots & \left|\begin{matrix} \frac{\partial N_i}{\partial x} \\ \frac{\partial N_i}{\partial y} \end{matrix}\right| & \cdots\cdots \end{bmatrix}, \; i=1,2,..4 \qquad \text{(A.11.1)}$$

For axisymmetric formulation:

$$B^u = \begin{bmatrix} \cdots\cdots & \left|\begin{matrix} \frac{\partial N_i}{\partial x} & 0 \\ 0 & \frac{\partial N_i}{\partial y} \\ \frac{\partial N_i}{\partial y} & \frac{\partial N_i}{\partial x} \\ \frac{N_i}{r} & 0 \end{matrix}\right| & \cdots\cdots \end{bmatrix}, \text{ and } B^T = B^\varphi = \begin{bmatrix} \cdots\cdots & \left|\begin{matrix} \frac{\partial N_i}{\partial x} \\ \frac{\partial N_i}{\partial y} \\ \frac{N_i}{r} \end{matrix}\right| & \cdots\cdots \end{bmatrix}, \; i=1,2,..4 \qquad \text{(A.11.2)}$$

where r is the radius of an element.

Substituting (A.6) and (A.10) into (A.5) and rearranging the terms such that it is valid for any arbitrary values of virtual displacement, potential, and temperature yields the following finite element equations

$$\left[\begin{array}{cc|c} K_{uu} & K_{u\varphi} & -K_{uT} \\ K_{\varphi u} & -K_{\varphi\varphi} & K_{\varphi T} \\ \hline 0 & 0 & K_{TT} \end{array}\right] \left\{\begin{matrix} u \\ \varphi \\ \hline T \end{matrix}\right\} = \left\{\begin{matrix} F_u \\ F_\varphi \\ \hline F_T \end{matrix}\right\} \qquad \text{(A.12)}$$

where the element stiffness matrices and the loading vectors are calculated such that

$$K_{uu} = \int_v B^{u^T} c\, B^u dv, \quad K_{\varphi\varphi} = \int_v B^{\varphi^T} \kappa\, B^\varphi dv, \quad K_{TT} = \int_v B^{T^T} k B^T dv + \int_{s_q} h_v N^{T^T} N^T ds_q$$

$$K_{u\varphi} = K'_{\varphi u} = \int_v B^{u'} e\, B^\varphi dv, \quad K_{uT} = K'_{Tu} = \int_v B^{u^T} \lambda\, N^T dv, \quad K_{\varphi\theta} = K'_{T\varphi} = \int_v B^{\varphi'} p\, N^T dv$$

$$F_u = \int_{s_t} N^{us'} t \, ds_t + \int_v B^{u'} c \varepsilon^s \, dv$$

$$F_\varphi = -\int_{s_Q} N^{\varphi s'} Q ds_Q + \int_v B^{\varphi'} P^s \, dv$$

$$F_T = \int_{s_q} q_s N^{Ts'} ds_q + \int_{s_q} h_v N^{Ts'} \left(T_f - T\right) ds_q \tag{A.13}$$

The Gauss quadrature technique is used to numerically evaluate the integrations in (A.13).

Appendix B

List of Publications

Journal Publications

1. ***Senousy, M. S.,*** Li, F., Mumford, D., Gadala, M. S., and Rajapakse, R.K.N.D. (2009) Thermo-electro-mechanical performance of piezoelectric stack actuators for fuel injector applications, *Journal of Intelligent Material Systems and Structures*, Vol. 20(4), pp. 387-399.

2. ***Senousy, M. S.,*** Rajapakse, R.K.N.D., Mumford, D., and Gadala, M. S. (2009) Self-heat generation in piezoelectric stack actuators used in fuel injectors, *Journal of Smart Materials and Structures*, Vol. 18(4):045008

3. ***Senousy, M. S.,*** Rajapakse, R.K.N.D., and Gadala, M. S. (2009) A Temperature-Dependent Two-Step Domain-Switching Model for Ferroelectric Materials, *Acta Materialia,* doi:10.1016/j.actamat.2009.08.039.

Conference Publications

1. ***Senousy, M. S.,*** Rajapakse, R.K.N.D., and Gadala, M. S. Experimental investigation and theoretical modeling of piezoelectric actuators used in fuel injectors. *Invited Paper, IUTAM09 Symposium- Multiscale Modeling of Fatigue, Damage and Fracture in Smart Materials Systems, September 1-4, 2009, Freiberg, Germany.*

2. ***Senousy, M. S.,*** Rajapakse, R.K.N.D., Mumford, D., and Gadala, M. S. Theoretical modeling of heat generation in piezoelectric actuators under dynamic driving conditions. *12th International Conference on Fracture, July 12-17, 2009, Ottawa, Canada.*

3. ***Senousy, M. S.,*** Rajapakse, R.K.N.D., Mumford, D., and Gadala, M. S. Self heating in piezoelectric actuators-based fuel injectors. *9th International Conference on Mechanical Design and Production, January 8-10, 2008, Cairo, Egypt.*

4. ***Senousy, M. S.,*** Rajapakse, R.K.N.D., Mumford, D., and Gadala, M. S. Heat generation in piezoelectric stack actuators under high operating conditions. *CANSMART International Workshop, pp.179-188, October 10-12, 2007, Montreal, Canada.*

5. ***Senousy, M. S.*** Li, F., Mumford, D., Gadala, M. S., and Rajapakse, R.K.N.D. Dynamic thermo-electro-mechanical performance of piezoelectric stack actuators. *Proceedings of SPIE, Vol. 6526, pp. 6526091-9, March 12-18, 2007, San Diego, CA, USA.*

6. ***Senousy, M. S.,*** Gadala, M. S., and Rajapakse, R.K.N.D. Coupled finite element modeling of piezothermoelastic materials. *Proceedings of SPIE Vol. 6526, pp. 65260H1-11, March 12-18, 2007, San Diego, CA, USA.*